The Divergent Pathways and Mechanisms of Energy Dissipation at the Interfaces of Martensitic Tribocouples

Von der Fakultät für Ingenieurwissenschaften, Abteilung Maschinenbau und Verfahrenstechnik der

Universität Duisburg-Essen

zur Erlangung des akademischen Grades
einer
Doktorin der Ingenieurwissenschaften
Dr.-Ing.

genehmigte Dissertation

von

Priska Stemmer
aus
Gladbeck

Datum der mündlichen Prüfung: 24. Oktober 2016
Erstgutachter: Prof. Dr.-Ing. habil Alfons Fischer
Zweitgutachter: Apl.-Prof. Dr. Martin Dienwiebel

Abstract

The requirements for technical systems subjected to friction and wear become more demanding, therefore the components are exposed to increasing stresses. Besides possible safety matters, failure of tribologically loaded systems cause tremendous maintenance costs. Due to the lack of reliable wear prediction models, tribometer tests are used in order to investigate wear behavior of materials and lubrication conditions.

For well-aimed optimizations of tribological contacts a comprehensive understanding of wear processes is necessary. However, the transferability of many studies into technical applications is arguable due to applied loads, lubrication conditions and material selection.

In this study specimens with different topographies and subsurface structures were investigated prior to and after tribological testing. The tests have been carried out under application related conditions regarding material properties, lubrication and loading conditions. The analyses of surface and subsurface characteristics were performed using complementary microscopy techniques, such as EBSD and TEM. Findings from microscopic analyses were linked to the frictional and wear behavior in order to gain information about energy dissipation and dissipative mechanisms within the respective system. The presence of a grain-refined layer appears to have a beneficial influence on the adaptation of the counterfaces and enhances the robustness of the tribosystems.

In addition wear debris was analyzed and different mechanisms of particle generation were discussed.

Kurzfassung

Steigende Anforderungen an technische Systeme, welche Reibung und Verschleiß ausgesetzt sind, führen dazu, dass die eingesetzten Bauteile höheren Belastungen ausgesetzt sind. Abgesehen von möglichen Sicherheitsrisiken, führen Ausfälle tribologischer Systeme zu erheblichen Instandhaltungskosten. Das Fehlen zuverlässiger Modelle zur Vorhersage des Verschleißverhaltens bedingt den Einsatzt von Tribometerversuchen um das Verschleißverhalten von Werkstoffen und die Schmierungsbedingungen zu untersuchen.

Dabei setzt die gezielte Optimierung tribologischer Kontakte ein umfangreiches Verständnis der Verschleißprozesse voraus. Die Wahl der verwendeten Belastungen, Schmierungszustände und Werkstoffe vieler tribologischer Versuche führte jedoch dazu dass die Übertragbarkeit der Ergebnisse auf technische Anwendungen kaum geben ist.

Im Rahmen dieser Arbeit wurden Proben mit unterschiedlichen Oberflächentopographien und oberflächennahen Gefügestrukturen vor und nach tribologischen Versuchen analysiert. Die Verschleißversuche sind bezüglich der Werkstoffeigenschaften, sowie der Schmierungs- und Belastungszustände unter anwendungsnahen Bedingungen durchgeführt worden. Die Analyse der Oberflächen und oberflächennahen Bereiche wurde mit Hilfe komplementärer mikroskopischer Methoden, wie EBSD und TEM, durchgeführt. Die Ergebnisse dieser Untersuchungen wurden anschließend mit dem Reibungs- und Verschleißverhalten korreliert um Informationen über Energiedissipation und dissipative Mechanismen in den jeweiligen Tribosystemen zu erlangen. Dabei zeigte sich, dass das Vorhandensein eines feinkörnigen Bereichs an der Oberfläche einen positiven Effekt auf die Anpassungsfähigkeit der Kontaktflächen und die Robustheit des Tribosystems zu haben scheint.

Zusätzlich wurden Verschleißpartikel analysiert und verschiedene Mechanismen der Partikelentstehung diskutiert.

Contents

Abbreviations

BB	base body
BF	bright field
BS	bearing steel
CB	counter body
CI	cast iron
CoF	coefficient of friction
CS	carburized steel
CSP	cross section polisher
DF	dark field
DP	diffraction pattern
EBSD	electron backscattered diffraction
ECC	electron channeling contrast
EDS	electron dispersive X-ray spectroscopy
FIB	focused ion beam
IM	interfacial medium
IQ	image quality
IS	ion slicer
KAM	kernel average misorientation
MD	molecular dynamics
nc	nanocrystalline (< 100 nm)
PIPS	precision ion polishing system
SE	secondary electrons
SEM	scanning electron microscopy
TEM	transmission electron microscopy
ufc	ultrafine crystalline (100 – 500 nm)
µc	microcrystalline (> 500 nm)

1 Introduction

Martensitic steels and cast irons are widely used in energy and automobile applications e.g. as gearbox components [1]. Due to ecologic and economic requirements, the loading and endurance requirements of those applications become more demanding. Often the tribological systems run under mixed or boundary lubrication, which might lead to higher friction coefficients and higher wear. However, an extended service time as well as low production costs and energy consumption for those components are claimed [2–4]. Well-functioning technical applications should usually operate within the ultra-mild wear regime with wear rates in the range of 10 nm/h [5]. In order to maintain such small wear rates it implies that the initially processed surface topography should be preserved for a long period of time [6]. The initial surface topography has a major influence on the tribological performance [7]. Thus, one approach to satisfy these demands is to reduce friction and wear by adjusting the surface topography and generating a beneficial subsurface microstructure [8–10]. Another way of increasing the wear resistance includes surface modifications such as coatings [11]. Ceramic materials are known to feature a high wear resistance and low friction coefficients in sliding applications. However, due to their hard and brittle nature, a breakdown or delamination of these coatings often result in catastrophic failure of the tribosystem [12–14]. In contrast, metals are generally more adaptive and robust based on their ability of plastic deformation. Here, surface treatment can be used to improve material properties. Heat treatments like carburizing or nitriding are well-established methods of increasing fatigue strength and wear resistance of highly loaded components [1, 15].

The alterations of sliding interfaces and subsurface microstructures can have a decisive influence on the tribological behavior [16–18]. However, the majority of tribological studies investigate material pairings and loading conditions which bear no relation to technical applications [19].

This work addresses the influence of surface and subsurface alteration of application related tribosystems in regard to their tribological behavior.

1.1 Challenges of tribometer testing

Properly-functioning lubricated tribological applications usually run within the ultra-mild wear regime. The conduction of tribometer tests often serves the purpose to further optimize such systems. However, a majority of these tests are carried out under too high tribological stresses and therefore display abrasion and adhesion as main wear mechanisms [20–22]. Although this facilitates quick results and eases the determination of material loss and subsurface alterations, these wear mechanisms are known to produce wear rates in the range of several µm per hour [23] which, in the case of most technical tribocontacts, would lead to failure [24]. Therefore, they are not sufficient in simulating real applications with other main wear mechanisms acting.

Nevertheless, investigations using unlubricated or wear-prone tribosystems illustrate distinct processes of material alterations [25, 26] and simplifications provide many useful insights into acting mechanisms during sliding [27, 28].

Even though the transferability regarding the wear behavior of technical application is limited, e.g. MD simulations represent a further possibility to investigate mechanisms in tribological contacts [29] and can help to elucidate elemental processes on an atomic level [30].

Implementing that acting mechanisms and wear rates of laboratory tribotests are comparable to those of technical applications significantly increases the reliability of results in regard to the transferability onto the actual application.

Still, in order to investigate wear processes at very low wear rates, material selection and surface treatment often are influenced by the need for simplified representations of acting mechanisms [31].

1.2 Surface engineering

Regarding technical surfaces, the term surface not only defines the outer form but includes a certain subsurface volume. In this work, the term surface is specified as outer boundary of the sample, whereas subsurface describes regions near but not necessarily exposed to the surface. The term near-surface refers to the region exposed to or as far as some 100 nm below the surface.

Technical surfaces often show different properties compared to the bulk structure. Depending on the application, technical surfaces have to provide certain functions. These can involve optical (reflectivity, absorbability), chemical (corrosion resistance, biocompatibility), physical (conductivity, magnetism) or tribological (wear resistance, sliding behavior) properties. The required functionality can be accomplished by applying coatings or by thermal (hardening), chemical (etching) or mechanical (cold working) alterations of surface and subsurface of a component [32, 33].

A well-directed manufacturing procedure can generate the required topographies and provide modified surface and subsurface structures. The investigation of suitable methods and process parameters is object of great interest since it can reduce time and cost for manufacturing [34–39].

Surfaces are usually specified on the basis of parameters like the average roughness R_a or maximum height of profile R_z, yet these parameters are insufficient in order to describe the surface topography. The Abbott curve provides a more accurate tool in characterizing the topography by concisely displaying the portions of profile peaks, profile valleys and bearing ratio [40].

While there is no direct relation between surface roughness and friction [41] an increase in bearing area can have a beneficial influence on tribological behavior due to a reduction in contact pressure. Profile valleys on the other hand can have a positive impact by serving as lubricant reservoir [42].

1.3 Material alterations and grain refinement

As is generally known, tribological contacts can undergo drastic alterations of their surfaces and subsurface regions [43, 44]. Schmaltz described the subsurface zone of technical surfaces after machining to consist of a very thin exceptionally fine grained surface layer with a highly deformed underlying transition zone towards bulk material [45]. Besides purely mechanical alterations due to severe plastic deformations, subsurface regions can undergo chemical alterations by incorporating substances from the lubricant and the surroundings [46, 47]. This effect, known as mechanical mixing, can distinctly influence the properties of the tribolayer [48].

Godet discussed the influence of wear particles in affecting sliding interfaces and wear behavior. After particle detachment the so called third bodies can undergo mechanical

and chemical alterations and being trapped within the contact, separate the first bodies which can have a beneficial or detrimental impact [49, 50].

The beneficial influence of subsurface microstructural alteration on the sliding wear behavior was shown by [51–53]. Fischer pointed out that merely the formation of a nanocrystalline tribolayer does not provide good wear behavior, but that a sufficient stabilization of this layer by the underlying material is essential. This was shown to be the case for materials revealing solely planar slip [54].

The phenomenon of local severe plastic deformation is also known to form in bulk materials. Dodd and Bai considered the formation of adiabatic shear bands as plastic flow due to localized heating because of large plastic strains [55]. While temperature certainly has an influence on material properties, an external input of temperature is not necessary in order to form shear bands. Farren and Taylor reported that around 85-95% of the plastic work during metal extension is transformed into heat [56].

Grain refinement within shear bands due to plastic strain localization can roughly be summed up as a result of dislocation nucleation, pileup or cell formation, with sub grains constituted of low angle boundaries, while increasing strain can lead to further grain refinement and misorientation. The alignment of crystals into shear direction can lower the shear strength, thus once a shear band has formed further strain accommodation will mainly occur within this plastically unstable region. Advanced grain refinement allows accommodating shear stresses in form of plastic flow, while dislocation movement and twinning is replaced by grain boundary sliding and grain rotation [57].

Severe plastic deformation, used in processes like high pressure torsion (HPT) or equal channel angular pressing (ECAP) in order to produce nc or ufc bulk materials, is subject to extensive research [58–62]. These materials offer improved material properties like high yield strength due to grain boundary hardening, according to the theory of Hall-Petch [63, 64]. However, several studies demonstrated decreasing strength after reaching a critically small grain size, this effect is known as inverse-Hall-Petch relation [65–68]. While ductility generally decreases with increasing strength, some studies reported an opposite trend, demonstrating excellent properties of nc or ufc materials showing high strength and ductility [69–71].

While this shows beneficial characteristics, the formation of so called white etching regions represents a detrimental form of material alterations. These regions are named

according to their appearance. White layers and bands are non-etched regions in polished and etched cross-sections which appear white under reflected light.

The occurrence of so called white etching layers (WEL) or white etching bands (WEB) is one reason of failure in highly loaded steel contacts. White etching regions can develop already during manufacturing [72] or during the operation in tribological contacts [73, 74]. Usually white etching layers exhibit a higher hardness than the bulk material and are composed of ultrafine or nanocrystalline grains [75–77]. The regions are assumed to form under high shear stresses in combination with increased temperatures and thereby fostering localized decarburization or phase transformation while others assume that the formation mechanisms are similar to those of adiabatic shear bands [72, 78, 79].

1.4 Wear models and energy dissipation

Even though a reliable prediction of wear is still elusive due to the complexity of sliding contacts, the need to describe wear resulted in a multitude of wear models. Probably the most well-known wear model is the one by Archard:

$$W = \frac{K\ s\ P}{p_m} \tag{1}$$

He described mechanical wear as the removal of particles with a linear relation of the applied load P, the sliding distance s and a wear coefficient K in regard to the flow pressure p_m of the softer material on wear W [43, 80].

While the wear model by Archard implies a constant material removal, other models describe wear as a more discontinuous and localized process after reaching a shakedown limit as a result of strain accumulation due to repeated plastic deformation during sliding [81, 82]. This is called ratchetting or cyclic creep [83–85]. These models regard wear from a mechanical side, whereas oxidational models like the one from Quinn consider wear as a tribochemical process [86–89].

The difficulty in describing wear lies in the complexity of tribological processes. Besides material and lubricant properties, overlapping and change of wear mechanisms, the evolution of wear debris and third bodies all have influence on the wear behavior. All these factors are hard to capture within a model, particularly since they can differ with time and location.

Ludema encouraged a mechanism-based modeling of tribological issues due to the limited use of existing models and the high maintenance costs caused by components subjected to friction and wear [90]. The complexity and variety of tribological applications led to the development of wear mechanism maps which can be used as a tool for the design process [91–93].

Another approach in order to describe wear is based on the dissipation of energy [94–96]. Friction work W_F represents the loss between input and output work of sliding contacts. Therefore, dissipated friction energy E_d is defined as:

$$W_F \triangleq E_d = \int F_F(s) \cdot ds = \int \mu F_N(s) \cdot ds \tag{2}$$

where F_F is the friction force, s the sliding distance μ the coefficient of friction and F_N the applied normal load.

Uetz and Föhl separated the friction energy in individual terms for deformation, fracture, thermal and secondary processes and concluded that the largest proportion is dissipated in form of thermal energy [97]. This was confirmed by other studies which described the thermal portion to contribute around 90 % of the dissipated energy [98, 99].

Fouvry and Kapsa described a threshold energy for metals under which no material loss was detected [100]. Implementing an energy related wear rate e_w constitutes a further attempt to predict wear.

$$e_w = \frac{W_V}{E_d} \tag{3}$$

with W_V being the wear volume and E_d the dissipated friction energy. By relating material loss and dissipated energy several studies implied a linear trend [96, 98, 101–103]. Contrary results were reported by [99, 104] displaying a relation between energy-based wear rate and acting wear mechanisms. These conflicting results may be related to changes in acting wear mechanisms during sliding. Shakhvorostov et al. attempted to quantify terms of energy dissipation of a lubricated steel/cast iron contact, using online tribometry. They found that approximately 70 % was dissipated in heat and the second largest part was represented by material transformation processes [105].

2 Aim of this study

In this study surface and subsurface alterations of technical materials which were exposed to different machining processes and lubricated reciprocating sliding wear tests are investigated.

A first objective of this study is the characterization of the specimens after manufacturing and to discuss possible influences of material alteration on the tribological behavior.

Further objectives are the analysis of worn specimens in regard to surface and subsurface alterations as well as the characterization of wear products. These findings ought to be discussed in regard to the frictional and wear behavior as well as dissipative mechanisms of the respective system.

3 Materials

3.1 Sample materials

3.1.1 18CrNiMo7-6

The case hardening steel 18CrNiMo7-6 (1.6587) was subject to these studies. Figure 1 shows the bulk microstructure. The nominal chemical composition for this steel is given in Table 1. Case hardening steels are widely used in energy and automobile application where they are utilized in gear units. By carburizing the steel to 63 HRC a state similar to that in gear applications was reached. Carburizing can improve the fatigue limit and wear resistance [1]. The heat treatment was conducted under a carbonaceous atmosphere. Thus, with respect to the heat treatment, this steel will be referred to as carburized steel (CS). Carburized steels are characterized by a surface layer of high hardness and a ductile core.

3.1.2 EN GJS-HB265

Cast iron (CI), specifically, EN GJS-HB265 was used as material for the base bodies of the dissimilar tribopairings. Spheroidal cast irons are characterized by globular precipitation of graphite. The globular morphology of the graphite lead to higher ductility compared to cast iron with vermicular or lamellar graphite precipitates. Hence, they are also referred to as ductile cast iron. Due to their good mechanical properties and castability, they are used in complex and highly loaded parts, like engine components such as crankshafts or pistons [106]. The bulk microstructure is shown in Figure 1, displaying a ferritic-perlitic matrix with some coarse Mo-carbides. The chemical composition is given in Table 1. The cast iron samples were flame hardened to 56 HRC, which is a widely used process in order to increase the wear resistance [1].

3.1.3 100Cr6

Commercially available bearing balls have been used as counter body for the cast iron test series. The through-hardenable bearing steel (BS) 100Cr6 (1.3505) is characterized by high strength and features a hardness of more than 60 HRC. The chemical composition, according to EN ISO 683-17, is displayed in Table 1. Besides for rolling bearings, these materials are used in applications that are exposed to high compressive stresses, e.g. contacts between camshaft and valve train [1]. The martensitic bulk microstructure, containing fine carbide precipitates, is shown in Figure 1.

3.2 Sample processing / sample history

Besides heat treatment the samples were subjected to further surface modulations in form of different machining processes before tribological testing.

3.2.1 Surface processing

The samples were machined using different processes, in order to investigate how the surface topography in regard to the roughness affects the wear resistance of the material under reciprocal sliding wear conditions. The milling, grinding and honing processes were conducted at the ISF at the TU Dortmund, Germany and are schematically shown in Figure 2.

The surfaces were prepared as following resulting in different surface topographies:

- milled condition leaving a periodic semicircled surface;
- ground after milling in order to decrease the surface roughness;
- honed after milling to reduce the peak height while preserving the profile valleys;
- polished for a smooth surface, serving as a reference sample.

In the following, the conditions will only be referred to as milled, ground, honed and polished surfaces.

The milled surfaces featured the highest surface roughness for both materials, as displayed in Table 2. Despite their likeliness in surface roughness, the honed surface exhibited a higher bearing area ratio than the ground sample, as was shown by Goeke [39].

3.2.2 Wear tests

Tribological testing of the samples was carried out by Stickel [107, 108]. The reciprocating sliding wear tests were conducted in the ball-on-plane configuration as schematically shown in Figure 3. The test parameters are given in Table 3.

Self-mating carburized steel tribopairings were tested at room temperature and high viscous industrial gear oil was used as lubricant. Figure 4 and Figure 5 display the frictional behavior and wear volumes of the CS/CS test series. The unworn and worn surfaces are shown in Figure 6.

Tribotests of the cast iron/bearing steel couples were performed at 80°C, simulating elevated temperatures as they appear in engines. These tribopairings were lubricated using commercially available engine oil. Friction coefficients and wear volumes are given in Figure 7 and Figure 8, respectively. The worn surfaces of the base and counter bodies are illustrated in Figure 9.

All systems were run under boundary lubrication conditions. A detailed evaluation of the tribotests can be found in [109].

4 Metallography and microscopy

Surface and subsurface alterations of the specimens were investigated using the following complementing techniques.

4.1 Optical microscopy and hardness measurement

For a first examination of the wear tracks and microstructures a standard optical microscope (BX41, Olympus, Hamburg, Germany) was used. The samples were cleaned in an ultrasonic bath with ethanol before analysis of the wear tracks. For microstructural investigations cross-sections of the samples were prepared. Therefore, the samples were cut using a precision cutting machine (Accutom-50, Struers, Ballerup, Denmark) and embedded with a hot mounting press (Simplimet 1000, Buehler, Lake Bluff, IL, USA) in a graphite filled polymer (Technotherm 3000, Heraeus Kulzer, Hanau, Germany). The samples were then ground using 320 – 800 SiC grit papers and mechanically polished to a final polishing step using 1 µm diamond suspension. In order to reveal the microstructure, the samples were etched in 2 % nitric acid for a few seconds.
Hardness measurements were conducted on the cross-sections according to DIN EN ISO 6507-1 using a Zwick hardness testing device (Typ 3212, Ulm, Germany).

4.2 Scanning electron microscopy

For a more detailed analysis of the wear tracks and microstructures a FE-SEM (LEO 1530 Gemini, Zeiss, Oberkochen, Germany) was applied. Micrographs were obtained in secondary electron (SE) imaging mode. Chemical analyses were performed by electron dispersive x-ray spectroscopy (EDS) with a silicon drift detector (Apollo X, Ametek, Wiesbaden, Germany). The sample preparation was according to 4.1.
Using electron backscattered diffraction (EBSD), information regarding the crystal structures and lattice parameters can be achieved. In this work, kernel average misorientation (KAM) diagrams are used, indicating lattice distortions. KAM is

calculated by averaging the misorientations of surrounding data points in regard to the point at the center. In this case, the parameters were set to a radius of 3 for neighboring data points, using all points in the kernel as illustrated in Figure 10.

EBSD measurements were carried out at an acceleration voltage of 20 kV and the step size was set to 80 nm. A Digiview IV camera (Ametek, Wiesbaden, Germany) and corresponding analytical software (OIM 6.2, Ametek, Wiesbaden, Germany) were used for the analyses.

The cross-section samples were prepared, parallel to the sliding direction, using a cross section polisher (IB-09010CP, Jeol, Akishima, Japan). Initially, the samples were cut to a certain length and height, as shown in Figure 11. After this, an approximately 300 µm thin silicon wafer was glued on top of the samples with a two-component adhesive (G2, Gatan, Munich, Germany). This step was essential in order to prevent ion induced damage to the surface and to obtain good polishing results. Subsequently, one side of the sample was ground using 1200 grit SiC paper in order to approach the targeted position. The side of the sample was then polished with Ar^+ ions at 5 kV and approximately 130 µA for several hours.

4.3 Focused ion beam

Sample preparation by means of focused ion beam (FIB), was performed using a dual beam FIB/SEM system (Helios NanoLab 600, FEI, Eindhoven, Netherlands) as schematically shown in Figure 12. The cross-section procedure contained several steps (Figure 13). First, a protective Pt-layer was deposited at the area of interest on the sample surface. After this, bulk material was removed in a wedge-shaped trench by Ga^+ ions, on one side of the area. Using decreasing energies of the ion beam, the sidewall was polished at a small glancing angle in subsequent polishing steps. The processing parameters are given in Table 4.

Micrographs of the cross-sections were obtained in SE mode at 2 kV accelerating voltage. Microstructural features emerge due to electron channeling contrast (ECC).

4.4 Transmission electron microscopy

Transmission electron microscopy (TEM) provides the highest resolution of the utilized techniques. Bright field (BF), dark field (DF) and selected area electron diffraction were performed in order to characterize the defect structure of the specimens' subsurface region. A 120 kV TEM (EM 400, Philips, Eindhoven, Netherlands) was used for the analyses.

TEM samples of the unworn state were prepared by classical cross-section preparation. Therefore, two corresponding segments of the machined surfaces were glued together in a brass rod and further prepared up to electron transparency as described in [110].

TEM cross-section samples of the wear tracks were prepared using an ion polishing system (EM-09100IS, Jeol, Akishima, Japan). Therefore, small samples parallel to the sliding direction were cut, as pictured in Figure 14 (1-4) and a silicon wafer was applied to the surface as described in 4.2. Afterwards, the samples were ground with 1200 grit SiC paper to a thickness of 100 µm. Using an ion slicer, the cross-sections were then polished on both sides with Ar^+ ions, while a thin ridge of the sample was masked by a metal foil. The process parameters are shown in Table 5.

In order to gain electron transparency, an additional ion-milling process was necessary (Figure 14-5). Therefore, the specimens were successively thinned on both sides using an ion-mill (PIPSII Model No. 695, Gatan, USA). The ion-mill was operated at accelerating voltages between 5 kV - 0.5 kV and gun angles between 5° - 10°.

4.5 Wear particle analysis

Wear debris, suspended in testing fluids, had been collected at the end of the wear tests and stored in 1.5 ml Eppendorf reaction tubes.

Particle preparation for electron microscopic analysis was carried out in two ways, by applying individual droplets of suspended particles directly on a Cu-grid (147-2, Plano, Wetzlar, Germany) or by prior embedding and sectioning of the particles.

Both methods start with an isolation process in order to extract the particles from the lubricant. Therefore, the lubricant samples were centrifuged at 20.000 g for approximately 15 minutes using an Eppendorf centrifuge (type 5424, Hamburg, Germany). Following this, supernatants were removed and the samples washed and re-

suspended with solvents. These steps were repeated multiple times using different solvents (cyclohexane, acetone, isopropanol).

Isolated particles suspended in isopropanol could then be pipetted onto copper-grids for microscopic examination.

For embedding isolated particles, an acetone diluted epoxy mixture (Epoxy 3000, Cloeren Technology, Wegberg, Germany) was filled into the tubes. This was followed by a further centrifugation step in order to segregate the particles at the tip of the tubes. The tubes were stored for several hours in a thermomixer (Eppendorf, Hamburg, Germany) at 80° for polymerization. Particle isolation and embedding protocols can be found in the Appendix.

Sectioning of the embedded particles was carried out with a diamond blade using an Ultramicrotome (EM UC7, Leica, Wetzlar, Germany). The around 80 nm thin slices were then placed onto Cu-grids.

5 Results: Carburized steel tribopairings

5.1 Initial subsurface microstructure

A micrograph of the carburized steel after heat treatment is given in Figure 15. It shows the martensitic structure of the subsurface zone and occasional manganese sulfide inclusions. The phase map of an EBSD measurement of the subsurface zone revealed a retained austenite content of less than 2 % (Figure 16). Thus, the microstructure can be assumed as purely martensitic. Figure 17 shows a TEM bright field image with corresponding diffraction pattern of this region. A hardness depth profile is given in Figure 18, displaying a case hardness of 720 HV1, a core hardness of approximately 450 HV1 and a case hardening depth (CHD) of 2 mm, according to EN ISO 2639.

5.2 Microstructural alterations after manufacturing

Depending on the machining process the samples were exposed to various stresses resulting in different near-surface appearances.

5.2.1 Base bodies

Milled:

A cross-sectional SEM image of the milled sample is shown in Figure 19. The near-surface zone exhibits a distinctly different appearance compared to the bulk structure. A high degree of deformation in this zone is indicated by EBSD measurements where a kernel average misorientation >5° and a low image quality were detected, whereas within martensite lathes a KAM in the order of 1.5° - 3.5° was measured (Figure 20). This severely plastically deformed layer has a thickness of about 1.8 µm. Figure 21 shows a cross-sectional TEM image of this near-surface region, exhibiting a high defect density. Corresponding selected area electron diffraction reveals a nanocrystalline martensitic structure with cementite precipitates.

Ground:

Solely the ground sample showed a visible strain gradient after manufacturing, as demonstrated in Figure 22. In the SEM image the strain gradient shows a depth of around 1 - 2 µm. It is evident that microstructurally altered regions caused by the milling process have completely been removed. In Figure 23, the TEM bright field image displays an increasing defect density towards the surface where a thin nanocrystalline zone is revealed, as shown by the dark field image and corresponding diffraction pattern.

Honed:

The cross-sectional SEM image of the honed specimen shows no clearly visible microstructural alterations (Figure 24). In TEM, however, a thin nanocrystalline near-surface layer with an underlying transition zone, featuring a high defect density, are visible, as shown by the TEM images and diffraction pattern in Figure 25 (a) and (b), respectively.

Polished:

In Figure 26 the subsurface microstructure of the polished sample is shown. It is evident that, at the near-surface zone, no noticeable alterations occurred. This corresponds with the TEM images, where the typical martensitic structure is visible at the surface (Figure 27).

5.2.2 Counter bodies

The spherical tips of all carburized steel counter bodies were polished. The subsurface microstructure is exemplarily shown in Figure 28. The FIB cross-section displays the martensitic microstructure with no visible alterations of the near-surface region.

5.3 Surface and microstructural alterations after wear tests

Wear depths were roughly calculated from the given wear volumes [109] and apparent contact areas. The contact areas were determined from optical light microscopy images using ImageJ [111].

5.3.1 Base bodies

Surface alterations:

The images of the carburized steel samples in Figure 6 display the macroscopic surface alterations after wear testing. The wear track of the milled sample exhibits the most obvious changes. Here, the summits of the milling marks were reduced to plateaus while the valleys prevailed. The ground surface exhibits only moderate changes, in the form of flattened asperity summits. The wear tracks of the honed and the polished samples appear, besides a few grooves, unchanged. In SEM the bearing areas of the different samples appear similar, as can be seen in Figure 29. Besides some shallow grooves and occasional small pits, the worn surfaces appear smooth; the asperities were mainly leveled out due to plastic deformation.

Microstructural alterations:

Milled:

Cross-sections of the milled CS sample are shown in Figure 30. The KAM images of the unworn (a) and worn (b) state appear similar with a highly deformed layer at the surface. Considering a wear depth of app. 1 µm for the milled base body, it is evident that the stresses during machining and tribological testing lead to similar alterations of the near-surface zone.

TEM bright field images and corresponding electron diffraction pattern illustrate the microstructural gradient of the subsurface zone (Figure 31). Zone I displays the bulk structure with the typical martensitic appearance. In zone II the increasing defect density is evident. Towards the surface the crystalline structure becomes further disturbed resulting in grain refinement to the point of crystals with a grain size below 100 nm (zone III).

Ground:

The ground sample experienced less material loss than the milled base body. A wear depth of approximately 200 nm was reached. The cross-sections of the unworn (Figure 32 a) and worn (b) samples appear alike. The strain gradient from the grinding process is visible and also the nc near-surface layer was preserved throughout wear testing.

Honed:

For the honed base body the wear volume was not detectable since the changes in topography were at the resolution limit of the confocal white light microscope [109]. Regarding microstructural alteration during the wear tests, it is evident that these were minor, at most. The comparison of the honed base body prior to (Figure 33 a) and after (b) wear testing reveals no evident changes.

Polished:

As for the honed base body, the material loss of the polished sample was vanishingly small. However, in contrast to the unworn state the near-surface region of the worn polished sample shows some grain refinement, as displayed in Figure 34.

5.3.2 Counter bodies

Surface alterations:

In Figure 6 the macroscopic changes of the bearing areas of the counter bodies after the wear tests are illustrated. The contact areas appear smooth with some grooves, which are most pronounced in the contact area of the counter body run against the polished surface. It is evident from these images, that the counter body tested against the ground surface suffered the highest material loss, whereas the counter bodies of the honed and the polished samples wore the least.

Microscopically, the bearing areas show some grooves, small pits and indentations (Figure 35). The counter body run against the polished sample additionally exhibits chatter marks in the center of the contact zone.

Microstructural alterations:

In the FIB cross-section of the counter body tested against the milled sample an increase in lattice distortion and some grain refinement of the near-surface zone are observable (Figure 36). The near-surface microstructure of the counter body tested against the ground surface exhibits, beside an increased defect density, no obvious signs of plastic deformation as can be seen from the TEM bright field image and the corresponding electron diffraction pattern in Figure 37. In contrast, the near-surface regions of the counter bodies run against the honed and the polished samples clearly reveal grain refinement as shown in Figure 38 and Figure 39, respectively.

5.3.3 Wear particles

The analysis of wear debris from the self-mating carburized steel tribotests, revealed similar appearances of the particles independent of the initial surface topography. Therefore, images of the debris are exemplary shown in Figure 40. The majority of particles found were agglomerates (a+b) consisting of many fine globular pieces of debris with sizes in the range of 50 nm to some 100 nm. Sporadically, larger compact particles were found as shown in (c).

TEM micrographs show the high defect density within single pieces of debris (Figure 41 a) as well as in particle agglomerates (b). The evaluation of electron diffraction pattern taken from the debris revealed a martensitic non-oxidized structure and some carbide reflexes.

6 Discussion: Carburized steel tribopairings

Macroscopic and microscopic analyses, using both optical and electron microscopy, of machined and tribologically tested samples are linked in this study to their respective wear behavior, which was investigated in a previous work by Stickel [109], in order to provide a better understanding of wear processes and energy dissipation.

Initial state:

The specimen analysis of the initial state after surface processing revealed a distinct influence of machining method and process parameters. Besides the obvious differences in topography, the specimens show variations in the extent of subsurface alterations. High stresses during the milling process caused the formation of a noticeable severely plastically deformed structure of the near-surface region (Figure 21). The same is shown for the ground sample, even though to a smaller degree (Figure 23). While milling and grinding processes usually have a high energy input into the surface, which can lead to substantial alterations of the subsurface regions, the energy input due to honing or polishing is considerably smaller. This corresponds with the observation that no microstructural changes were found in the polished carburized steel reference sample as well as in the polished counter bodies (Figure 27 + Figure 28). The near-surface zone of the honed specimen, however, displayed a grain-refined layer (Figure 25). This can be explained due to an adaption of the honing parameters, in order to minimize material removal [112]. Thus, the severely plastically deformed near-surface structure from the previous milling process was partially preserved throughout the honing process. The deformation depths of the machined surfaces are given in Figure 42. Implying a beneficial influence of a grain-refined subsurface zone, it could be expected from these results that the milled and the ground samples would show the best performances under reciprocating sliding wear. However, there are way more parameters influencing the wear behavior of a tribosystem, as is generally known; including surface topography, bearing area ratio, lubrication and material properties, only to mention a few.

Regarding material properties, it is commonly known that martensites show a high wear resistance due to their high strength and internal compressive stresses [113]. Another

beneficial quality of these materials is the capability to absorb additional stresses due to a strain induced phase transformation of retained austenite into martensite [114]. However, based on the small fraction of retained austenite in the carburized steel of less than 2 %, this effect might be negligible for these samples.

White etching layer:

The formation of white layers during manufacturing is commonly known to have a detrimental influence on the wear behavior and lifetime of machine parts. Due to their hard and brittle structure WEL constitute a first stage of damage to bearing surfaces [76]. WEL were subject to many studies [72, 78, 115, 116], revealing a nanocrystalline structure, which seems comparable to the structure found in the samples from this study. However, optical microscopy revealed no evidence of such a layer.

Surface alterations and frictional behavior:

The surfaces of the carburized steel samples, shown in Figure 6, demonstrate an influence of the initial surface topography on surface alterations during sliding wear. The milled and the ground sample show a flattening of the summits, which lead to an increase of the bearing area and a reduction of the roughness. The polished surface demonstrated an opposite behavior, here, grooves lead to a roughening of the contact. The influence of an optimized surface topography during manufacturing can be seen by comparing the milled with the honed sample. While the summits of the milled surface were worn during sliding a topography similar to the honed one was approached, whereas in case of the honed sample, the reduction of the milling marks was achieved already by the honing process. As a result, the surface of the honed sample showed only minor alterations and very low wear after 2 million wear test cycles. The adaption of the sliding interfaces correlate well with the friction behavior (Figure 4). Stickel showed that the milled and the ground sample display a running-in behavior with a decreasing CoF, the course of the CoF of the polished sample was slightly increasing, whereas the CoF of the honed sample stayed almost constant during the whole wear test.

The SEM analyses of the wear tracks show a smooth appearance with occasional grooves and some small pits, mostly in the contact zones of the counter bodies. Even though the carburized steel, due to its low chromium content, possesses little corrosion resistance, corrosive wear can be ruled out due to the properties of the applied lubricant. This is confirmed by the absence of corrosion products and corrosive wear appearances in the wear track of the tribocouples. Considering that the samples were run in the ultra-mild

sliding wear regime [109] micro-ploughing, plastic flow and a mild form of surface fatigue can be implied as main acting wear mechanisms [24, 117].

The opposite behavior of the ground and the milled tribocouples in regard to the wear of the counter and the base bodies, respectively, could be influenced by the orientation of the machining marks of the base bodies, as schematically illustrated in Figure 43. The grinding marks of the ground base body run parallel to the sliding direction, probably allowing the summits to plough into the counter body, thus, by facilitating micro-ploughing, subsequently fostering the higher wear of the counter body. In the milled case, the machining marks are oriented perpendicular to the sliding direction. The stresses during sliding give rise to plastic deformation at the summits of the milled topography, consequently causing material being pushed out of the contact, as can be seen in Figure 44, eventually leading to material loss. Samerski found contrary results, were tribocouples with grinding marks parallel to the sliding direction exhibited lower wear compared to those with the grinding marks running perpendicular to the sliding direction. These conflicting results on the influence of orientation of machining marks may be due to differences in contact pressures, lubricant and type of wear particles. In his case, diesel fuel was used as intermediate medium and oxidational wear was characterized [118].

Energetic evaluation and material alterations:

Using data from [109], dissipated friction energies were calculated according to eq. (2), and displayed in Figure 45, together with the total wear volume (BB+CB) for all four surface conditions. The tribological experiments have shown that there is no simple relationship between friction and wear in these tribosystems. While the ground case exhibits the highest dissipated energy and wear volume, the dissipated energies for the milled and the honed cases are similar, but their wear volumes differ by more than one order of magnitude.

While from macroscopic view the determination of friction work is straightforward (given that the variables acc. to eq. (2) are known), the distribution of the friction energy within a tribosystem is a whole different story, as schematically shown in Figure 46 and Figure 47. For instance, different amounts of energy of unknown quantity are dissipated within the base body, the counter body and the interfacial medium. Further elements for possible energy dissipation are particles which can be displaced within the contact and undergo further alterations. Then there are different mechanisms of energy dissipation.

These processes include material transformation (deformation, mechanical mixing), material loss (fracture, cutting), heat and secondary processes (chemical, noise, luminescence), which again can influence one another. Additionally, both the distribution within the elements and the dissipative mechanisms can vary with time and location [97, 105]. Due to lack of experimental data, thermal processes are not addressed in this work. However, linking the frictional wear behavior to surface and subsurface alterations observed from microscopy analysis, provides information about acting dissipative mechanisms. Thus, this is a qualitative approach to evaluate dissipative mechanisms regarding material transformation and material loss processes.

By taking a separate look at the dissipated energies of the respective systems and the wear volumes of the counter and base bodies in regard to near-surface alterations, a relationship between the formation of a grain-refined zone and the wear volume can be seen for the counter bodies (Figure 48). While the counter bodies of the honed and the polished tribocouples exhibit a distinct nanocrystalline layer which goes along with a low wear rate, the near-surface region of the counter body run against the ground sample shows no grain-refined layer and the highest wear rate, the counter body of the milled case is in between.

The formation of near-surface grain-refined structures in the counter bodies of the honed and the polished cases combined with minimal wear, hint towards the conclusion that the friction energy introduced into these counter bodies was mainly dissipated by material transformation processes. For the counter body of the ground case, however, it is reasonable to assume that a larger part of energy was dissipated in processes causing material loss since the TEM analysis merely revealed minor changes in form of an increased dislocation density. This behavior is in good agreement with the contact situations in respect to the contact pressures as described in [109].

In case of the base bodies (Figure 49), the interpretation of the data is more complex due to the different initial topographies and near-surface structures. The polished reference sample shows some grain refinement in the near-surface region at the end of the wear test and very low wear, so it is to be assumed that the energy was mainly dissipated due to material transformation. The near-surface region of the honed sample shows similar appearances in the unworn and worn state and comes along with very low wear. Therefore, in contrast to the polished surface, it can be assumed that the energy was not mainly dissipated due to grain refinement but rather as a consequence of internal

friction processes within the already nanocrystalline zone due to grain boundary sliding or grain rotation [30, 84, 119].

The higher wear rate of the milled and the ground base bodies and the presence of a nanocrystalline near-surface structure indicate that the shear stresses were accommodated by dissipating energy due to plastic flow, grain rotation as well as grain refinement. Accordingly, wear was probably mainly a consequence of material being squeezed out of the contact.

Since the here tested martensites are inapt for elaborating material transformation processes, the different stages of deformation are illustrated on an austenitic steel sample from an additional investigation. These micrographs reveal evidence of dislocation nucleation, plastic flow, grain boundary sliding and grain rotation. While the first two show little effect on the diffraction pattern, the grain-refined structure, necessary for the latter, is evident in the formation of a ring pattern. The regions of grain boundary sliding reveal a texture, while grain rotation increases the misorientation of the crystals, as displayed in Figure 50.

Energy-based wear rates are displayed in Figure 51. These were calculated according to eq. (3) using data from [109].

In some studies it was deduced that the energy-based wear rate allows for distinguishing between wear mechanisms [99, 102, 104]. In the present case of systems running under ultra-mild wear conditions, the energy-based wear rate seems to be more of an indicator for the robustness of a system, specifying how much energy the tribosystem can accommodate before a certain amount of material loss occurs. Displaying the slope of e_w by continuous measurement of friction forces and material loss, instead of the total values at the end of the wear test, probably would be more revealing, e.g. in regard to changes in wear mechanism.

Wear particles:

Although the analysis of wear particles is supposed to allow for conclusions about acting wear mechanisms, in the case of ultra-mild sliding wear it is questionable whether this method is applicable, because these assumptions are based on studies with high wear rates and micrometer-sized wear particles, showing characteristic morphologies [120–123]. However, the results of the wear debris analysis can be used to exclude certain mechanisms. Particles found from these wear tests exhibit a granular form and usually a size within the nanometer range. TEM images reveal a highly deformed structure

(Figure 41) comparable to the one of the nanocrystalline near-surface zone from the sliding bodies, supporting the conclusion that material loss took place in a small volume of the near-surface region [54, 124]. Evaluation of corresponding electron diffraction pattern, reveal a metallic structure, therefore oxidational wear can be ruled out. This is in agreement with the analysis of the wear tracks. The appearances of agglomerates could be due to repeated shifting during the wear test or, more likely, due to the particle preparation. Still, in cases where wear particles were trapped between sliding interfaces and therefore underwent further alteration before leaving the contact, conclusions regarding their origins based on their appearances should be considered carefully.

7 Results: Cast iron/bearing steel tribopairings

7.1 Initial subsurface microstructure

After flame hardening, the subsurface zone of the cast iron base bodies exhibits a martensitic matrix (Figure 52). To some extent, cementite plates are still present, causing finer martensite lathes. Evenly distributed spherical graphite precipitates and scattered molybdenum carbides are embedded within the matrix. The hardness depth profile is given in (Figure 53), revealing a conventional depth of hardening (DS) of around 1.5 mm, according to DIN EN 10328.
The subsurface regions of the through-hardened bearing steel counter bodies show a martensitic matrix with fine chromium carbides, as displayed in Figure 54. The carbides are homogeneously distributed and have sizes of 0.5 - 2.0 µm. The hardness was tested to be 750 HV1.

7.2 Microstructural alterations after manufacturing

7.2.1 Base bodies

Milled:
Figure 55 shows the subsurface zone of the milled cast iron sample. A highly deformed layer, with a thickness of around 1.5 µm, is visible at the surface. The initial perlitic structure of the material is still evident due to remains of cementite plates in the martensitic microstructure after flame-hardening. The nanocrystalline martensitic structure of the near-surface region is shown in the TEM images (Figure 56).

Ground:
The SEM image of the ground cast iron sample reveals no visible near-surface alterations, as shown in Figure 57. The TEM micrograph, however, reveals a very thin nanocrystalline surface layer with a well-defined transition to the underlying microcrystalline martensitic material (Figure 58).

Honed:

A cross-sectional SEM image of the honed cast iron sample is given in Figure 59, indicating no microstructural alterations of the near-surface region during manufacturing. Also, no alterations from the prior milling process seem to be preserved. This is confirmed by the TEM images shown in Figure 60.

Polished:

The martensitic microstructure of the polished cast iron sample shows cementite plates, as displayed in Figure 61. During polishing, no visible microstructural alterations of the near-surface zone were induced, as can also be seen from the TEM images (Figure 62).

7.2.2 Counter bodies

The microstructure of the bearing steel counter bodies is exemplarily displayed in Figure 63. The SEM image reveals the martensitic matrix with fine spheroidized carbides. Alterations of the near-surface-region are not recognizable.

7.3 Surface and microstructural alterations after wear tests

The wear depths of the respective bodies were determined as described in 5.3.

7.3.1 Base bodies

Surface alterations:

An overview of the worn surfaces is given in Figure 9. From optical microscopy images it can be seen that the wear track of the milled surface is characterized by flattened summits of the milling marks and some grooves, which are most pronounced in the center of the wear track. The contact area of the ground sample appears, besides some grooves, smooth and shiny. The honed surface appears matte; the wear track is mainly recognizable due to the worn machining marks. On the polished surface the wear track seems to be covered by a thin tribofilm; in addition, some grooves are visible.

On a microscopic level, the contact area of the milled sample reveals some grooves but most parts are covered with a patchy tribolayer (Figure 64). The wear track of the ground surface appears plastically deformed with some pits and grooves while most

grinding marks have been evened out leading to a smoother interface. Third body formation is evident at the bearing area of the honed sample. Some debris and lubricant remained in recesses at the end of the wear test. The wear track of the polished sample shows shallow grooves, pits and a thin tribolayer. Furthermore, noteworthy features are microcracks in the vicinity of graphite nodules. These are particularly characteristic for the milled and the honed samples, while the ground and polished samples show those to a considerably smaller extent.

The surface chemistry of the worn surfaces was analyzed by means of EDS. Elemental mappings on the wear track of the ground specimen, given in Figure 65, reveal molybdenum carbides and pits filled with lubricant residue. EDS maps of the honed sample indicate that the third bodies are composed of material from the first bodies and intermediate medium (Figure 66).

Microstructural alterations:

Milled:

The near-surface region of the milled base body possesses the most distinct microstructural alteration with an about 2 µm thick zone indicating severe plastic deformation, as shown in Figure 67. The nanocrystalline structure of this region is visible in the TEM image (Figure 68). Considering a wear depth of approximately 1.5 µm it is evident that this structure was formed during sliding.

Ground:

From the KAM map in Figure 67 it is observable that the ground sample features a distinct near-surface layer with a high defect density. TEM micrographs of the near-surface region revealed a grain size in the range of 100 nm (Figure 69).

Honed:

Cross-section analyses of the honed sample reveal that the depth of the grain-refined layer is less extended compared to the milled and the ground bodies (Figure 67). A gradient from bulk to ultrafine to nanocrystalline structure is observable in TEM images of the worn near-surface region (Figure 70).

Polished:

Similar to the honed sample, the near-surface region of the polished sample exhibits a discontinuous deformed surface layer with varying thicknesses (Figure 67). An

increased defect density and grain refinement can be observed after sliding. The ultrafine to nanocrystalline martensitic structure of this region is shown in Figure 71.

7.3.2 Counter bodies

Surface alterations:

The worn surfaces of the counter bodies are shown in Figure 9. From these images it can be seen that the counter bodies tested against the ground, the honed and the polished samples were worn roughly the same amount, while the counter body of the milled sample wore less. From SEM analyses, shown in Figure 72, it is evident that the wear tracks of the counter bodies are characterized by mild grooves, small pits and third-bodies sticking to the surface. The contact areas sporadically show some microcracks and µm-sized pits. These are most evident in the wear track of the counter body from the ground sample, followed by the counter body tested against the milled sample.

Microstructural alterations:

From FIB cross-sections of the counter bodies tested against cast iron, it is evident that the thickness of the third bodies, observed on the surface of all BS counter bodies, is in the range of some 10 nm (Figure 73 - Figure 76). For the honed and the polished cases, the near-surface regions only indicate minor alterations, whereas the counter bodies of the milled and the ground samples clearly reveal grain refinement in the near-surface region after sliding. The cross-section of the counter body from the ground case reveals microcracks running at a small angle below the surface.

7.3.3 Wear particles and third bodies

For the cast iron versus bearing steel tribocouples, two types of wear debris were mainly found; larger metallic particles (Figure 77) and small plate-like cementite debris (Figure 78). In Figure 79, the flaking of a particle in the vicinity of a graphite nodule is shown. Some pieces of debris were trapped in machining marks whereas others remained in the contact zone resulting in the formation of a patchy third-body (Figure 80).

8 Discussion: Cast iron/bearing steel tribopairings

Initial state:

The analysis of the machined cast iron samples shows, particularly for the honed surface, differences in surface topography compared to the carburized steel samples, even though the specimens were machined using the same process parameters. The surface roughness of the cast iron samples are higher compared to the carburized steel samples as shown in [112]. Cross-sectional analysis of the cast iron specimen after machining, using electron microscopy, revealed the highest energy input in form of a grain-refined near-surface layer in the milled sample. Here, a nanocrystalline near-surface layer of around 1.4 µm thickness was observed (Figure 55 + Figure 56). The honing and polishing processes, on the other hand, did not visibly affect the near-surface material, while grinding led to a thin nanocrystalline layer (Figure 57 - Figure 62). The smaller deformation depth of the ground CI sample compared to CS could be attributed to stabilizing effects of hard phases such as cementite plates.

Surface alterations and friction behavior:

While for the CS a correlation between macroscopic surface alterations and friction behavior could be found, this is different for the CI/BS couples. Even though the milled, ground and honed surfaces show an adaption of the sliding interfaces in form of reduced summits (Figure 9), only the CoF of the ground case shows a decreasing trend. The slope of the CoF for the milled base body stayed relatively steady during the whole test, whereas it initially decreased and later increased for the honed case (Figure 7). An explanation could be the third body formation. On a microscopic level, the ground and polished surfaces appear slightly plastically deformed with third body seemingly smeared on the wear track, but the contact area predominantly appears smooth (Figure 64). The contact areas of the milled and honed samples on the other hand show patches of third body sticking to the surface of the wear track (Figure 80). The different appearances of the third body are also evident in the SEM images and EDS maps of the honed and ground wear tracks. While in the ground case the third body is most

prominent in recesses within the wear track (Figure 65), on the honed sample the third body protrudes from the wear track (Figure 66).

While the flattening of the machining marks lead to an increase in contact area and therefore decreasing the contact pressure and roughness, a reduction of the friction coefficient would be expected [109]. The formation of additional asperities and debris particles in the contact zone, however, has a detrimental effect as also shown by [125]. These additional asperities can procure further jamming events and therefore result in higher frictional forces [33, 124, 126]. The formation of those patchy third bodies could be emanated due to the occurrence of larger wear debris, as they were found for the milled and the honed cases. Surface damages in form of microcracks were observed in the vicinity of graphite nodules. Under cyclic loading during the tribotest the propagation of these cracks results in the formation of larger particles. The detachment of such a particle is shown in Figure 79. The appearance of microcracks was mainly observed on the milled and honed surfaces. These unstable regions around graphite nodules could be induced by the development of metal sheath during machining, where material is either smeared over [127] or pushed into graphite nodules, as schematically illustrated in Figure 81.

The lower CoF of the ground and polished CI/BS tribocouples compared to the CS could be attributed to graphite released from the nodules acting as solid lubricant [1, 128, 129]. However the beneficial influence of the graphite seems to be limited to the polished and ground series. Stickel assumed that the released graphite was deposited in machining grooves and thus could not act as a solid lubricant for the milled and honed test series [108]. It is also quite possible, that the release of graphite into the contact was hindered in the first place due to closed graphite nodules [130] or that the patchy third body represents no suitable surface for the graphite in the honed and milled cases.

A noteworthy observation of the cross-section analysis was that some regions of the ground CI below the wear track exhibited a distinctly different microstructure. This could be a result of the flame hardening process where the rapid heating can cause insufficient diffusion times for carbide dissolution and ferrite → austenite phase transformation [1]. The optical micrograph reveals an incomplete martensitic transformation of the subsurface region (Figure 82). Therefore the hardness of this region of the ground sample shows considerably lower values compared to the properly flame hardened zone of the other CI samples as displayed in Figure 83. This is in

contradiction to the common doctrine that good wear resistance is achieved by a higher hardness [33, 131, 132] since the ground CI base body showed the least wear. In this case the lower hardness could have supported an easier adaption of the interfaces and thereby improving the contact conditions, resulting in less wear.

Energetic evaluation and material alterations:

Alterations of the subsurface region due to tribological loading during the sliding process were analyzed by electron microscopy. The deformation depths measured from cross-section samples are displayed in Figure 84. It can be seen that all base bodies developed a distinct grain-refined zone, whereas the counter bodies show less near-surface alterations.

From the TEM images it is evident that the milled and the honed specimen exhibit a smaller grainsize than the ground and polished samples, which could be linked to the higher friction forces. Buckley demonstrated a correlation of friction forces and the extent of dislocation density in Co single crystals [133]. A connection between friction coefficients and the extent of grain refinement was also shown by [18, 31], where the proceeding disturbance of the crystalline structure led to a grain-refined surface layer. These kind of disturbances were reported to occur due to local instabilities [27, 57, 134–136] not only in tribological contacts but also in form of shear bands in fatigue tests. Here, the shear stresses are accommodated in the formation of a grain-refined zone and subsequently, according to [17, 137, 138], due to grain rotation. A similar behavior was found by Stoyanov et al. by MD simulations of tribological contacts where shear stresses led to dislocation nucleation and indicated a rotation of atom cluster [30]. The formation of shear bands was also observed within a nanocrystalline near-surface region of an austenitic high interstitial steel (AHIS) after tribological loading from further investigations (Figure 85). In this case, the additional grain refinement was probably brought by due to adhesion of the counterfaces and therefore temporarily shifting the sliding interface into one of the bodies before the contact was broken and the sliding resumed to the initial sliding interface between the two bodies.

Although, as mentioned earlier, the transferability into application related systems is limited, tribological and microscopic investigations of more ductile or less wear resistant materials offer the advantage that features like material loss or material transformation, due to their extent, are easier to quantify. Therefore, these methods provide indications about elemental mechanisms as described in chapter 6.

Plotting the wear volumes and dissipated friction energies, using data from [109], it can be seen that there are basically two levels of material loss and energy dissipation within the investigated tribosystems (Figure 86). While the wear volumes of the milled, ground and polished tribotests are similar, the dissipated friction energy was nearly twice as high in the milled case. The dissipated energies of the milled and the honed systems, however, are similar, with the wear volume of the honed case being around 50 % higher compared to the milled one. This indicates that a major part of the friction energy in the milled system was dissipated due to material transformation processes, while in the other cases comparatively more energy was dissipated in form of processes leading to material loss. As deduced by Stickel, the higher values in the honed case were probably caused by the more severe contact conditions.

Linking the dissipated energies to the deformation depth and material losses of the respective bodies provides indications about the distribution of energy dissipation, as illustrated in Figure 87 and Figure 88.

The energy input into the milled system led to lattice defects and eventually grain refinement of the near-surface zones of the counter body and the propagation of the already grain-refined zone into the bulk material of the base body. The very fine structure and the extent of the grain-refined zone in the base body in relation to the similar material loss of both bodies, indicates that in this case more energy was dissipated within the base body.

Interestingly, although the ground and the milled counter bodies reveal similar near-surface alterations, the wear volume of the ground counter body is twice as high, with the amount of dissipated energy within the systems being only about half as much compared to the milled one. This could be caused by a change in wear mechanism during the test, where the ground CB initially wore more while adapting the contact area, eventually reaching a stable corridor and allowing the generation of an easily sheared zone as found in the near-surface region after 2 million cycles. This would be comparable to the correlation regarding the energetic corridor during running-in and wear behavior as described by Scherge et al. [139].

The near-surface zone of the ground base body on the other hand clearly demonstrates material transformation as predominant dissipation mechanism. This was presumably favored by the lower hardness and higher deformability and, in consequence, allowed to accommodate more energy without material loss. The higher wear of the polished base

body seems to be attributed to less energy accommodation within deformation processes, rather than within processes leading to material loss, such as surface fatigue, which is evident in the wear track of the polished case (Figure 89). The counter body of the polished couple shows minimal near-surface alterations, thus in this body energy dissipation most likely also happened preferentially due to mechanisms facilitating material loss, e.g. surface fatigue.

A further process of energy dissipation represents the movement and alteration of wear particles. Depending on their size and location within the wear track, they can either be trapped within recesses, such as milling marks or graphite nodules, without affecting the wear behavior if they are small enough, or act as additional bearing asperities [50]. If particles happen to be between sliding counterfaces, they can cause abrasion and indentations as a result of a higher hardness [140] or surface fatigue due to an increase in local contact pressures. Furthermore, pieces of debris between sliding bodies can undergo plastic deformation and mechanical mixing. Those particles remaining within the contact and, sticking to one of the surfaces, form a third body. This was observed for all CI/BS tribocouples. However, regarding the dissipated energies and deformation structures found within the near-surface regions it can be assumed that for the milled and the honed tribocouples energy dissipation in form of movement and alteration of wear debris played a significant role in the friction behavior. This kind of behavior was also described by [141].

The energy-based wear rates e_w for the CI/BS tribosystems and their respective bodies are plotted in Figure 90 using data from [109]. However, one should keep in mind that the informative value of e_w for the separate bodies is highly limited, as long as the actual amount of dissipated energy within each body is unknown. In this case the milled tribocouple reveals the lowest energy-based wear rate, indicating the highest robustness of the different surface topographies.

In the CI/BS tribotests, the bearing steel counter bodies as a tendency showed the highest wear, implying less wear resistance compared to the cast iron. However, as the milled and honed cases illustrate, parameters characteristic for shifting wear to one or another body of a tribosystem should not be sought solely within material properties of the respective bodies, but rather other influences such as bearing area ratio or the orientation of machining marks should also be considered.

While most wear prediction models assume more or less linear wear rates, it is obvious that, particularly under ultra-mild wear conditions, wear is a highly discontinuous and locally occurring process. Due to the microstructural inhomogeneity of cast irons it is even more pronounced. This becomes apparent by determining the linear wear rate per stroke. In case of the ground counter body, which showed the highest wear, the linear wear rate would be in the range of 0.01 Å per stroke which is two orders of magnitude smaller than the size of an atom. Thus the question arises whether the occasional occurrence of grooves resulting from mild abrasion, could be accountable for most of the wear. Micro-cutting could have been caused due to abrasive particles such as broken molybdenum carbides or other hard phases. This would present a possible explanation for the minor alterations of the near-surface region found in some bodies, since in the case of micro-ploughing a distinct deformation zone would be expected according to [23].

9 Conclusions

In this study the influence of tribological stresses on material alterations of application related tribosystems were investigated from an energetic point of view.

Therefore self-mating carburized steel as well as cast iron/bearing steel tribocouples with the respective four different surface conditions were analyzed using microscopic techniques.

Although the exact amounts of dissipated energy into the respective elements of a tribosystem are unknown due to the complexity of those systems, the microscopic evaluation of these systems provide some insights into dissipative mechanisms. These in turn help to elucidate the frictional behavior of sliding interfaces.

It is incidental that the formation of a grain-refined near-surface structure improves the robustness of these tribosystems by acting as an easily sheared layer. These very fine-grained structures facilitate shear accommodation, without particle detachment, due to energy dissipation by internal frictional mechanisms like grain boundary sliding and grain rotation. In how far the formation of an easily sheared zone therefore facilitates an increasing friction coefficient in contrast to the influence of surface topography characteristics is still open, but certainly depends strongly on the respective loading conditions and material properties. Thus, the analysis of the mechanical properties of the grain-refined zone should be subject to further investigations.

The analysis of wear debris was found to give little indications about acting wear mechanism under ultra-mild wear conditions, since in this case wear is highly discontinuous and most wear debris undergo alterations before leaving the contact. However, it was indicated that particle formation occurs due to material being squeezed out of the contact, mild surface fatigue and abrasive mechanisms such as micro-ploughing or even micro-cutting.

It was also shown, in contrast to popular assumptions, that a higher hardness and smoother surfaces of the counterfaces are not necessarily accompanied by a better wear resistance. The ability for an adaption of sliding interfaces, on the other hand, can ease tribosystems into a stable frictional behavior. Additionally, these results confirm that due to a well-conditioned surface, the wear-intensive running-in phase can be omitted

or considerably reduced. Thus, by that approach, a significant step towards higher lifetimes of systems running under boundary lubrication can be reached.

Still, it must be pointed out that the transferability from one tribosystem to another is limited. For instance, microstructural inhomogeneity or instabilities, due to manufacturing processes, show a significant influence on the tribological behavior. This was particularly apparent for the cast iron specimen. Even though graphite can act as a solid lubricant, metal lids hindering the release of graphite and cracks in the vicinity of graphite nodules, consequently acting as source for the detachment of large wear particles, have a detrimental influence on the wear behavior.

The complexity of tribological contacts limits the use of wear models in predicting tribological behavior, particularly for application related systems. Therefore, high resolution microscopic analyses of surface and near-surface regions of tribologically loaded specimens provide a valuable tool for gaining information about wear processes. Consequently, these can be used for a systematic optimization of tribological applications.

10 Outlook

In order to verify the influence of machining marks on the diverging wear behavior of base and counter body, further tests with varying orientations of milling and grinding marks could be conducted. Additionally, the surface topography of the counter bodies could be varied.

The determination of mechanical properties of ultrafine grained and nanocrystalline martensite should be investigated in future studies. Specimen with similar structure and of sufficient size for those investigations could be produced for example by high pressure torsion.

Conduction of self-mating wear tests with specimen featuring the same topography and geometry, for instance in a crossed cylinder setup, could provide further information regarding energy dissipation within the respective elements of a tribosystem. Force and temperature profiles as well as material loss of both bodies should be monitored continuously during the wear test. Surface and subsurface alterations should be analyzed by complementary microscopical techniques.

11 Tables

Table 1: Chemical compositions of the investigated materials

	weight - %								
	C	**Si**	**Mn**	**Mg**	**P**	**S**	**Cr**	**Mo**	**Ni**
18CrNiMo7-6 (acc. to DIN EN 10084)									
min.	0.15	-	0.50	-	-	-	1.50	0.25	1.40
max.	0.21	0.40	0.90	-	0.025	0.035	1.80	0.35	1.70
EN GJS HB265 (*acc. to DIN EN 1563)									
min. *	3.30	2.00	0.20	0.02	-	-	-	-	-
max. *	3.80	3.00	0.50	0.07	0.10	0.01			1.00
acc. to EDS	3.36	1.35	0.12	0.06	-	-	-	0.58	-
100Cr6 (acc. to DIN EN ISO 638-17)									
min.	0,93	0,15	0,25	-	-	-	1,35	-	-
max.	1,05	0,35	0,45	-	0,025	0,015	1,60	0,10	-

Table 2: Roughness values of machined surfaces [112]

	maximum height of profile R_z [µm]	
	carburized steel	**cast iron**
milled	1.4 – 1.6	2.4 – 3.5
ground	0.1 – 0.8	1.4 – 1.9
honed	0.2 – 0.4	1.8 – 2.3

Table 3: Parameters and setup of reciprocating sliding wear tests [109]

base body	**carburized steel (plate)**	**cast iron (plate)**
counter body	**carburized steel (pin)**	**bearing steel (ball)**
CB (tip) radius	5 mm	5 mm
stroke δ	6 mm	6 mm
normal force F_N	30 N	30 N
test frequency	5 Hz	5 Hz
lubricant	Mobilegear SHC XMP 320	Mobile 1™ ESP Formula 5W-30
oil viscosity (at 40 °C)	320 cSt	72.8 cSt
oil temperature	20 °C	80 °C

Table 4: FIB cross-section preparation parameters

	acceleration voltage [kV]	**ion current [nA]**	**stage tilt angle [°]**	**shape**
fast milling	30	6.5	52	regular cross section
milling	30	2.8	52	cleaning cross section
polishing	30	0.46	53	cleaning cross section
polishing	30	$93 \cdot 10^{-3}$	54	cleaning cross section
cleaning	5	$47 \cdot 10^{-3}$	55	rectangle

Table 5: Ion slicer polishing parameters

	acceleration voltage [kV]	**gun tilt angle [°]**	**interval [s]**	**time [h]**
milling	5	1	77	5
cleaning	2	1.5	77	0.25

12 Figures

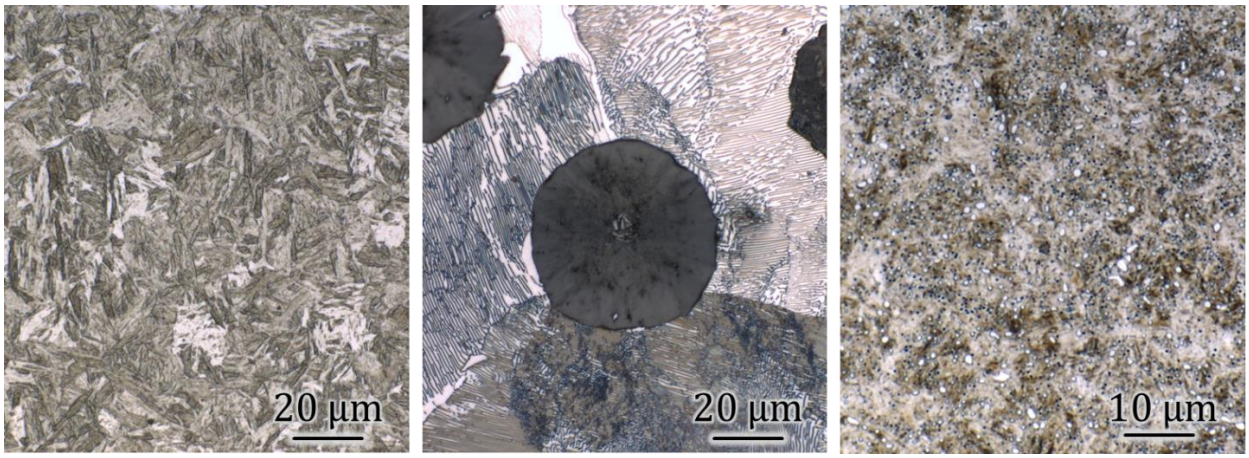

Figure 1: Bulk microstructures of (l.) quenched 18CrNiMo7-6, (m.) normalized EN GJS-HB265 and (r.) quenched 100Cr6

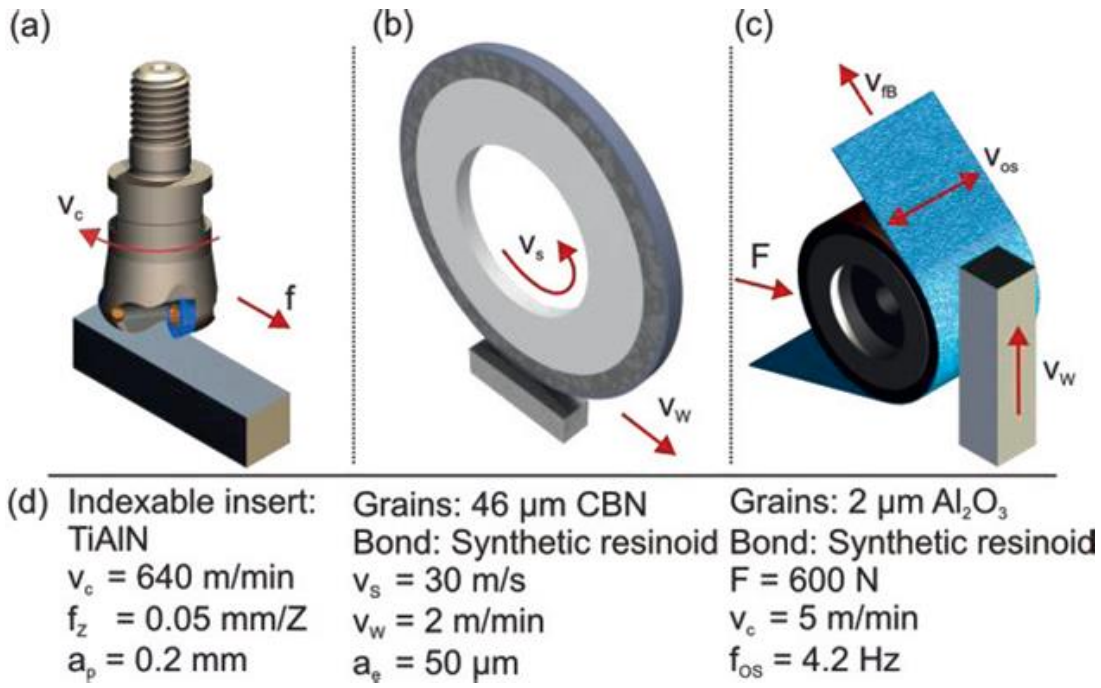

Figure 2: Schematic illustration of machining processes (a) milling, (b) grinding, (c) honing and (d) processing parameters [39]

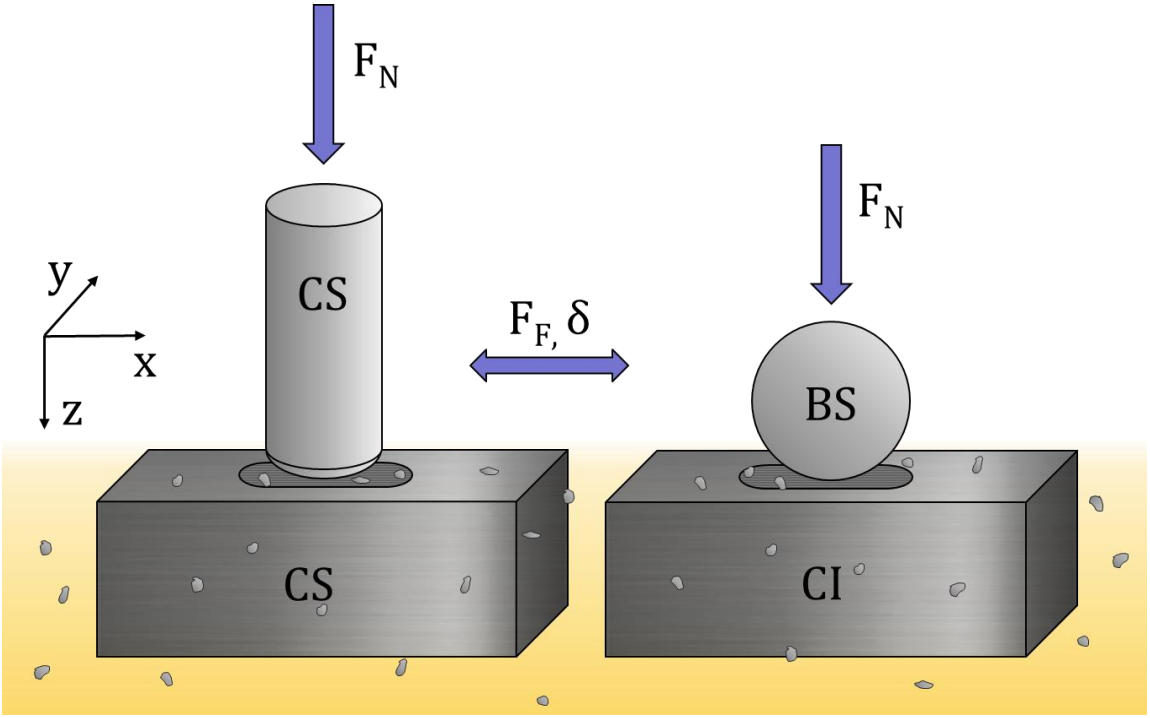

Figure 3: Schematic diagram of the tested tribosystems carburized steel vs. carburized steel and bearing steel vs. cast iron; x is in the direction of the main velocity vector, y is perpendicular to the sliding direction

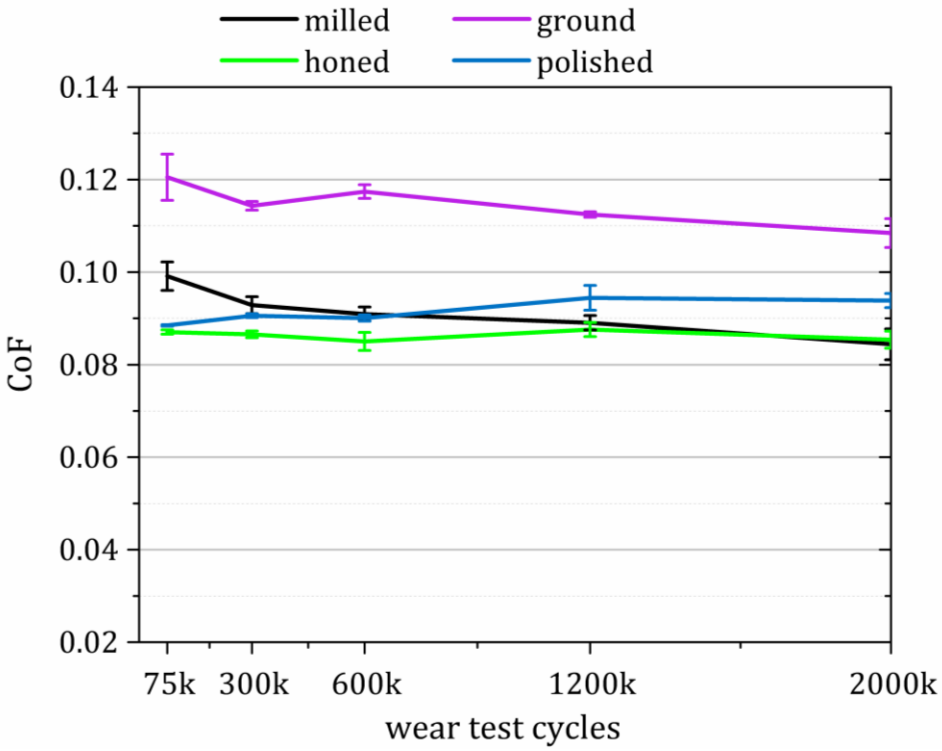

Figure 4: Coefficient of friction over cycles for the CS vs. CS wear tests [109]

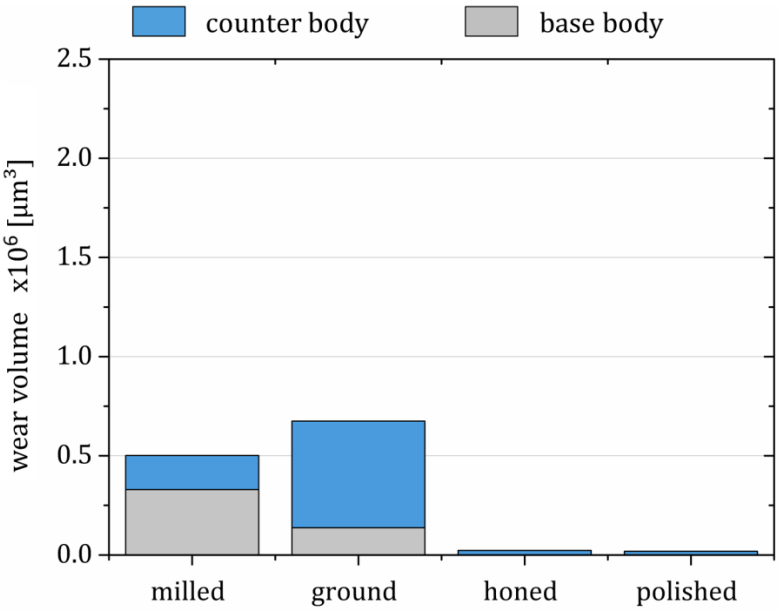

Figure 5: Wear volumes of CS base and counter bodies after 2 million cycles [109]

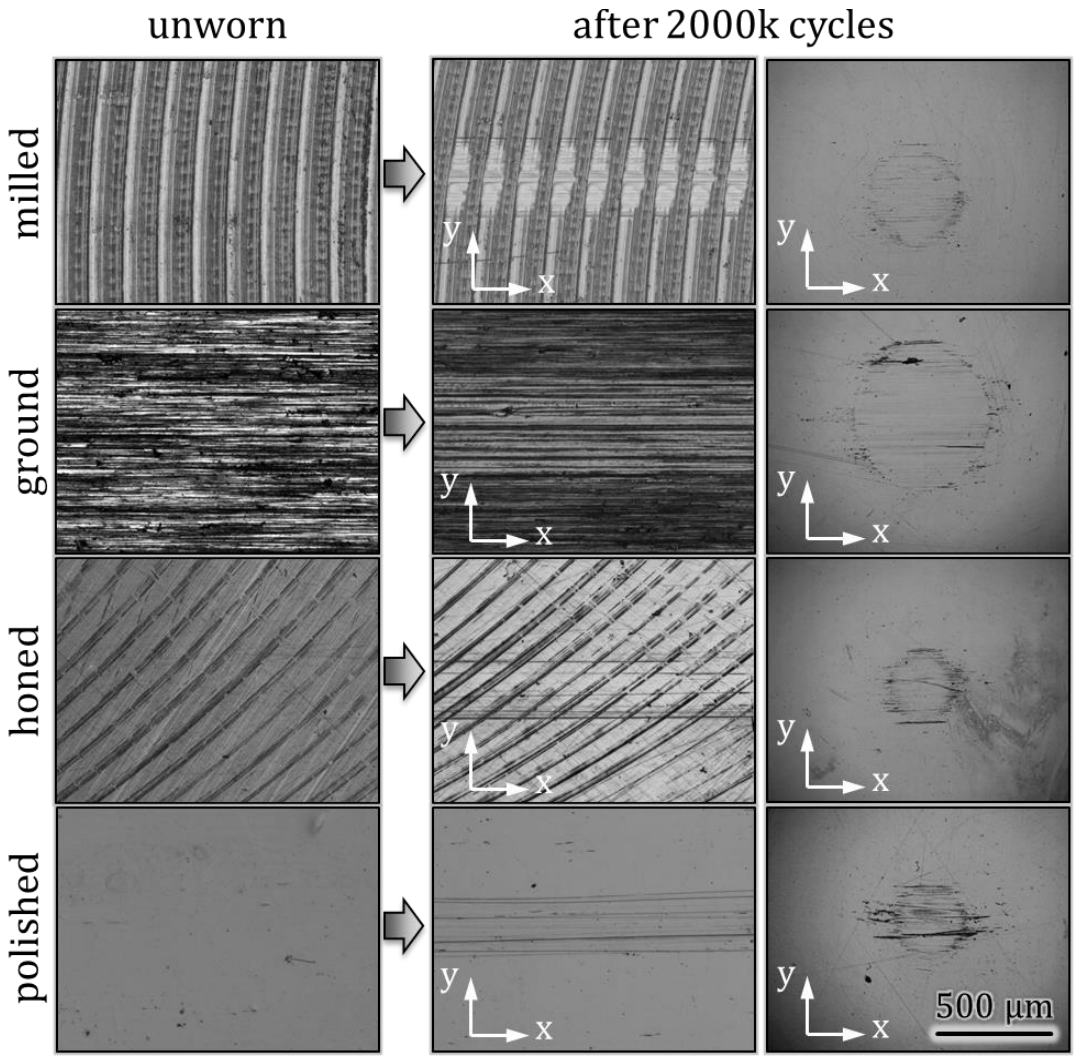

Figure 6: Optical micrographs of carburized steel samples, (l.) base bodies after machining, (m.) base and (r.) counter bodies after wear tests

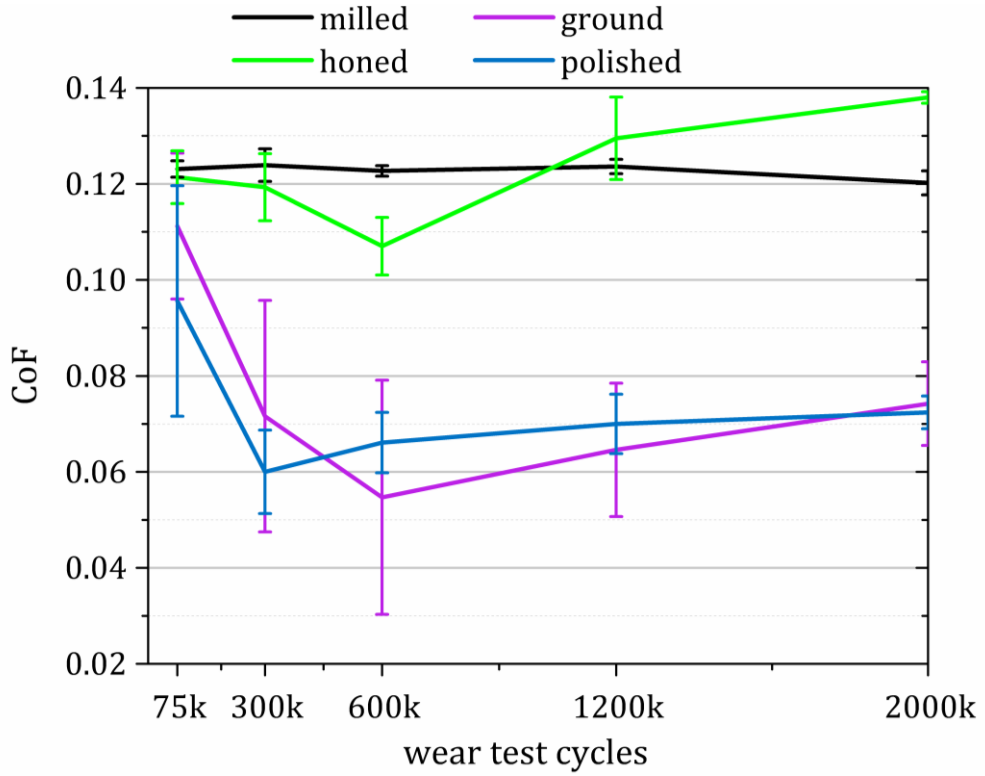

Figure 7: Coefficient of friction over wear test cycles for CI vs. BS wear tests [109]

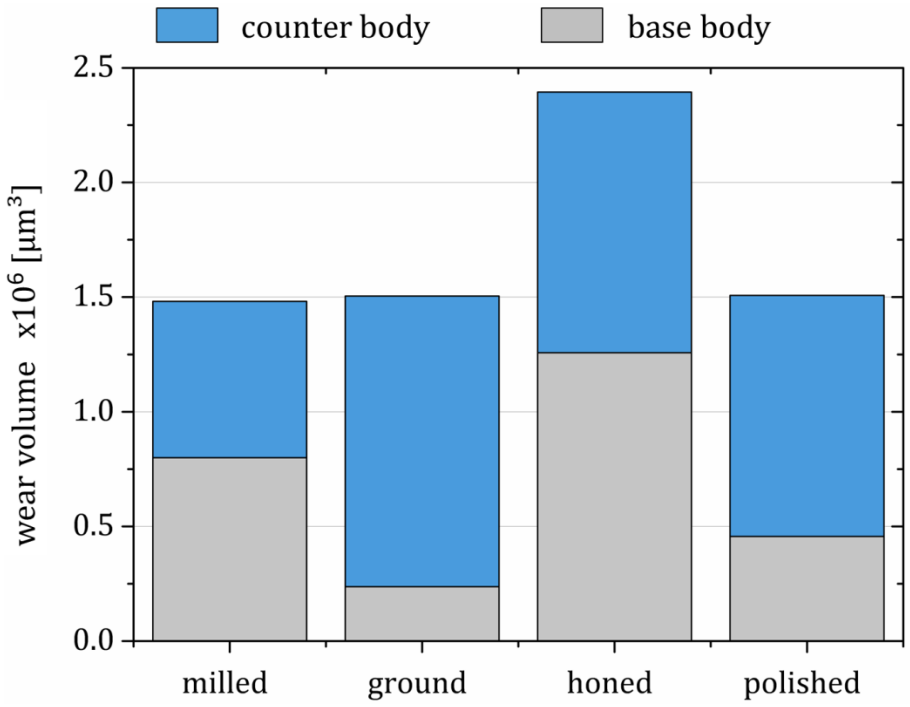

Figure 8: Wear volume of the CI base and BS counter bodies after 2 million cycles [109]

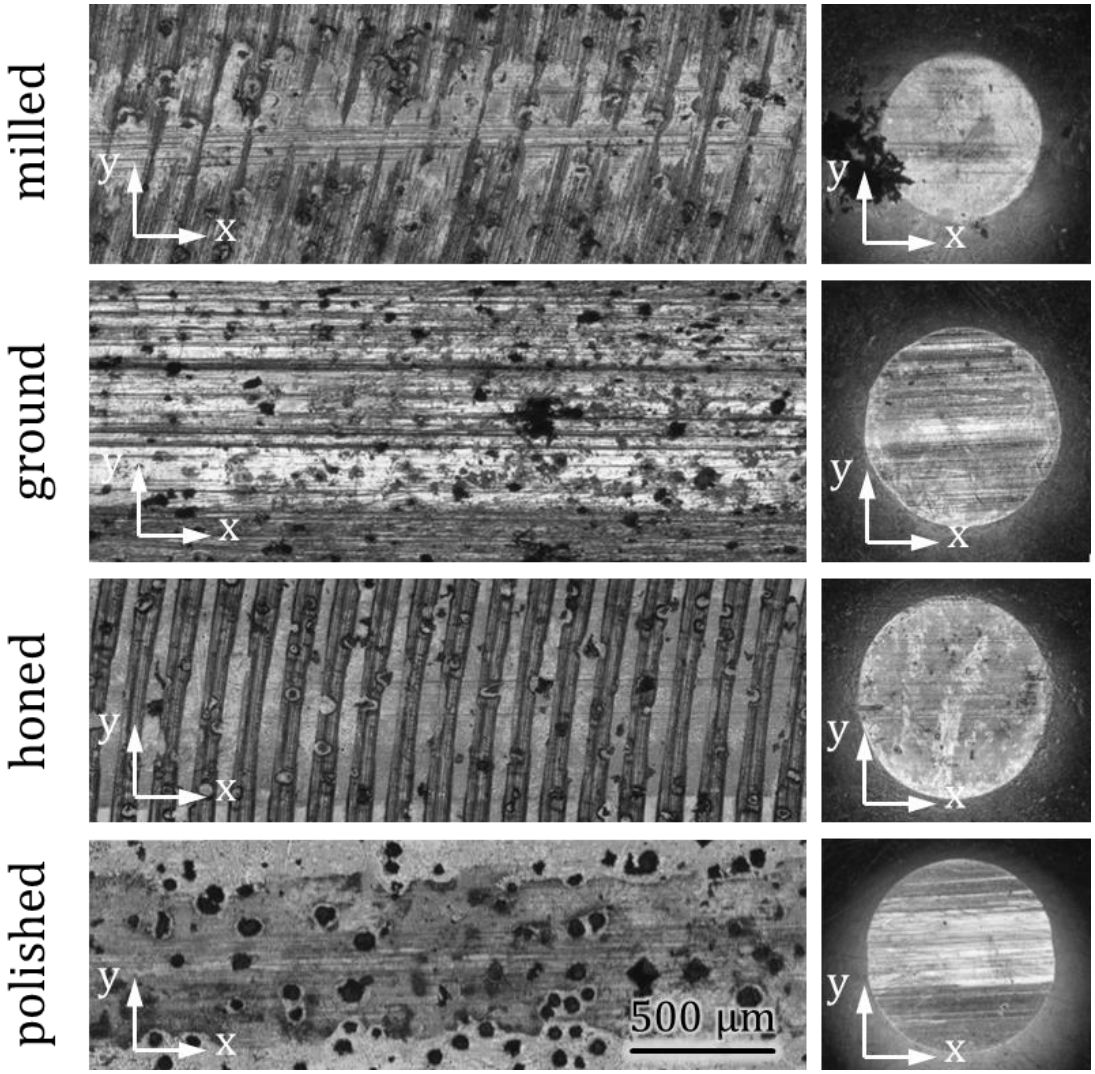

Figure 9: Optical micrographs of cast iron vs. bearing steel couples after wear tests

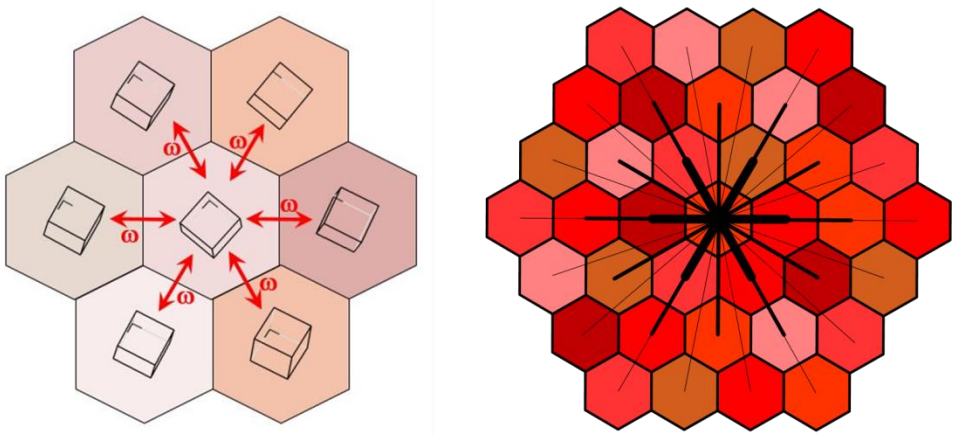

Figure 10: Schematic illustration of (l.) determination of the kernel average misorientation [142] and (r.) all points in kernel setting [143]

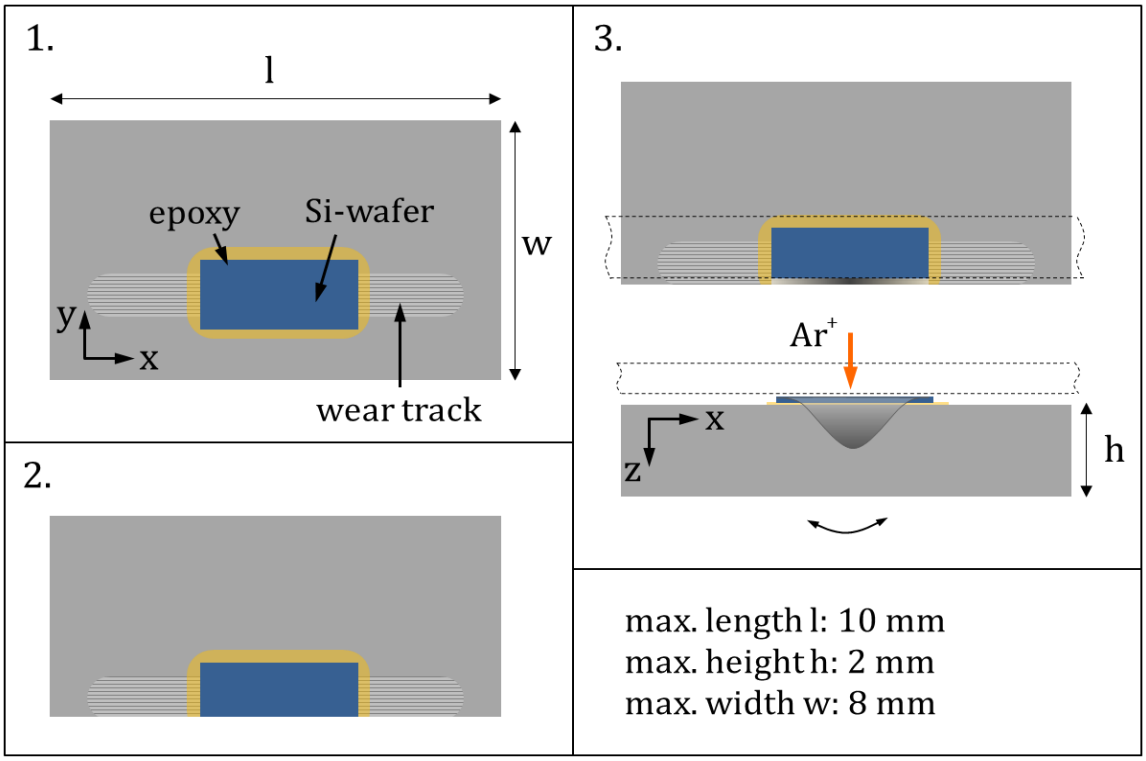

Figure 11: Cross-section specimen preparation for EBSD by means of a CSP

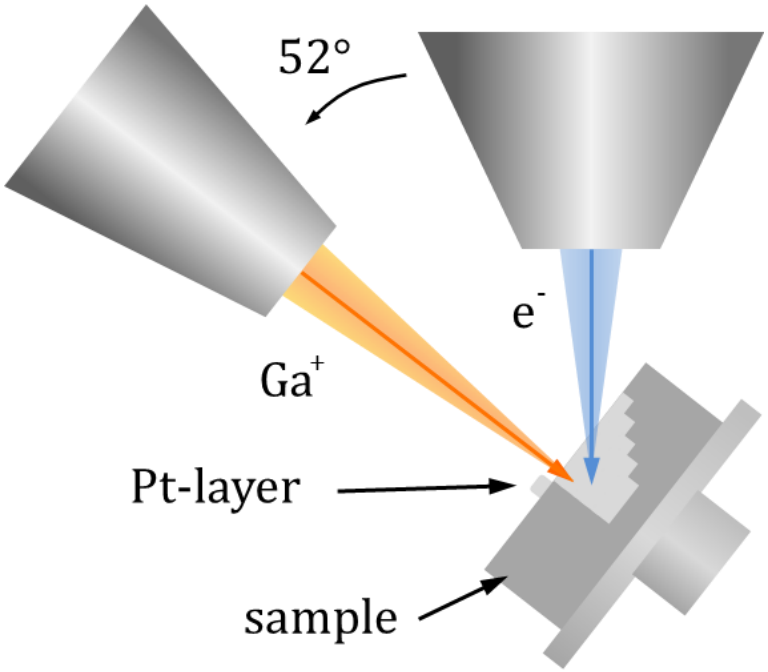

Figure 12: Cross-section preparation using a dual-beam FIB/SEM system

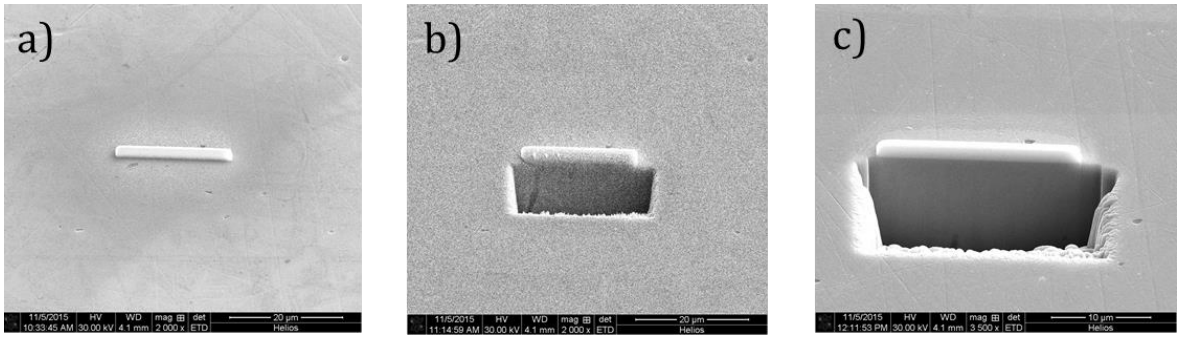

Figure 13: FIB cross-section preparation a) protective Pt-layer, b) fast material removal by high kV ion milling, c) low energy ion polishing – reducing ion damage and smoothing of the sidewall

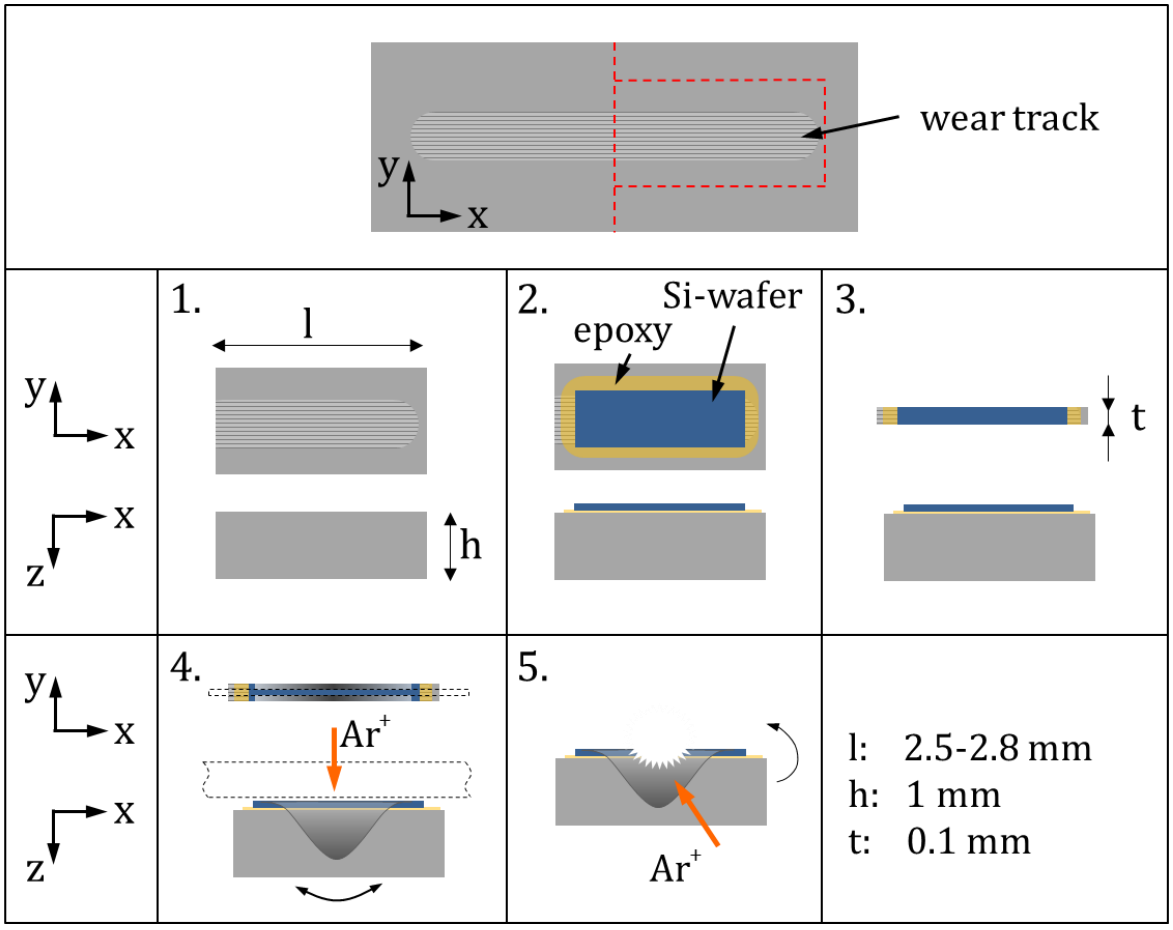

Figure 14: TEM cross-section preparation 1. cutting the sample to a certain size, 2. applying a protective Si-wafer on top of the wear track, 3. grinding the sample down to a thickness of 100 µm, 4. ion polishing of the cross-section (IS), 5. final sample thinning (PIPS)

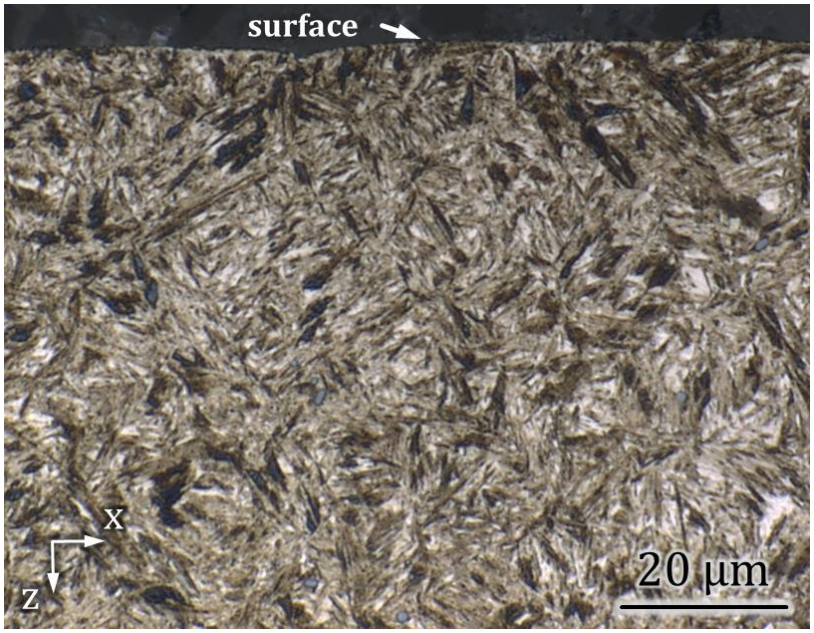

Figure 15: Optical micrograph of a cross-section of carburized steel after heat treatment

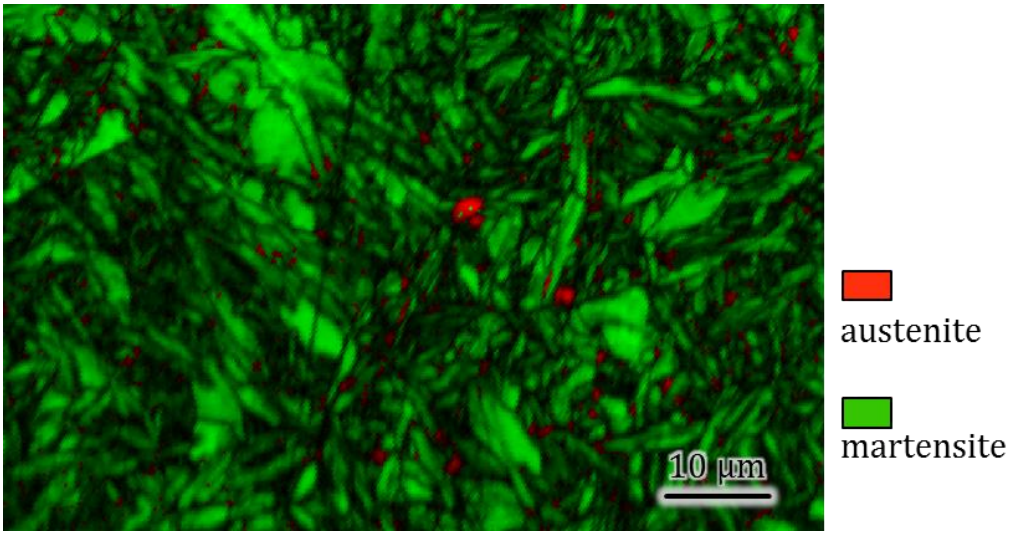

Figure 16: EBSD phase map of CS shows a martensitic matrix with less than 2 % retained austenite

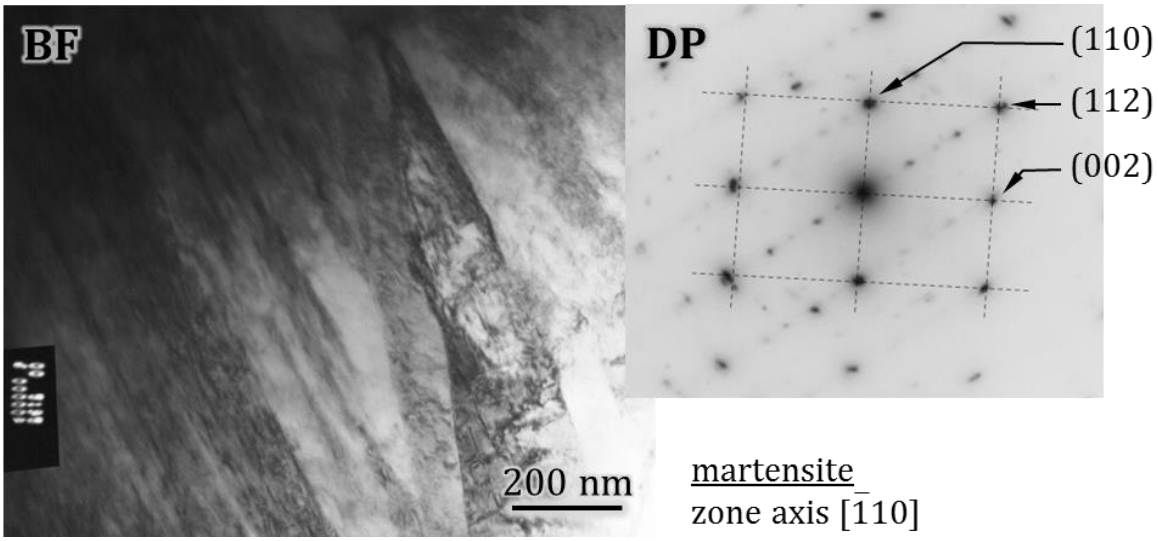

Figure 17: Martensitic microstructure of carburized steel

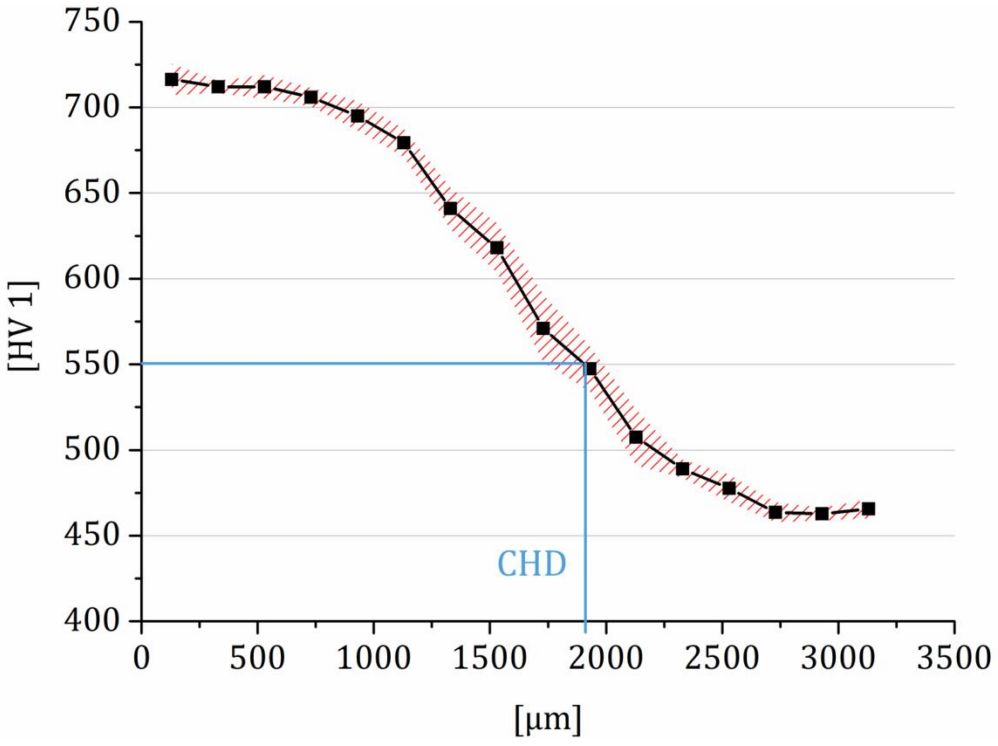

Figure 18: Hardness depth profile of carburized steel

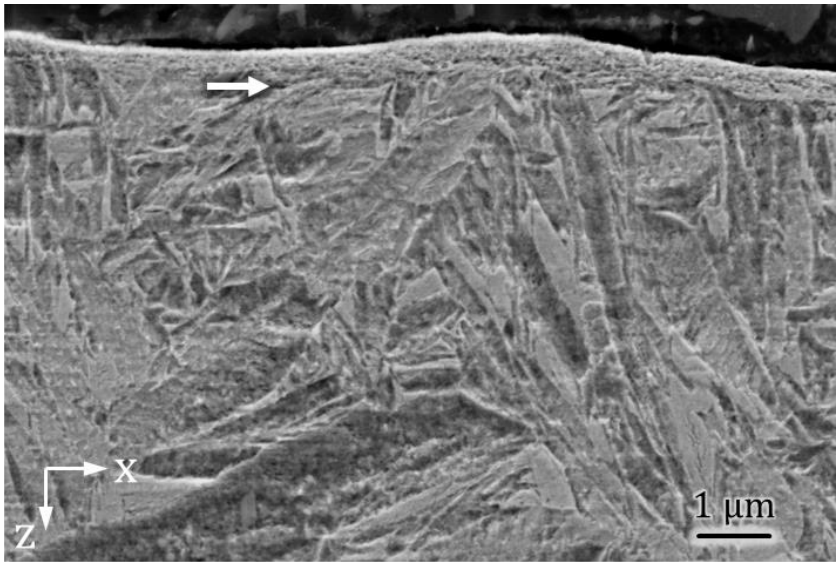

Figure 19: Cross-section of milled carburized steel, arrow indicates transition from bulk to highly deformed near-surface zone

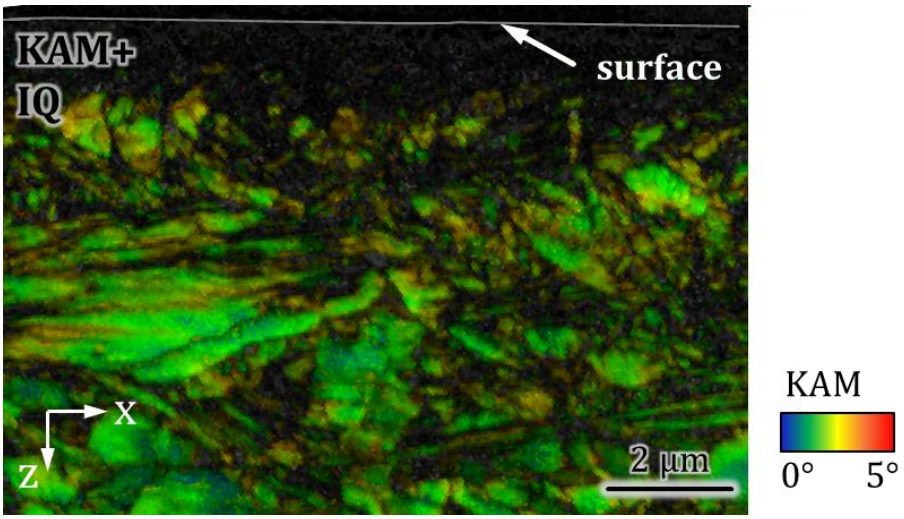

Figure 20: KAM map of milled carburized steel, severe plastic deformation in the near-surface zone restricts EBSD pattern quality

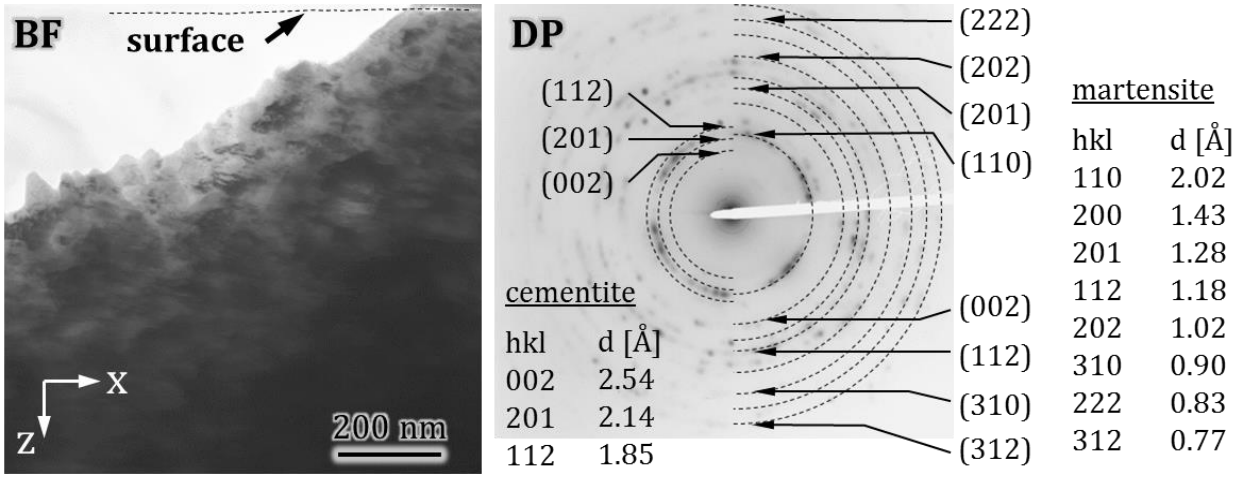

Figure 21: TEM micrograph of milled CS, diffraction pattern of near-surface zone exhibits nc martensite and some carbide reflexes

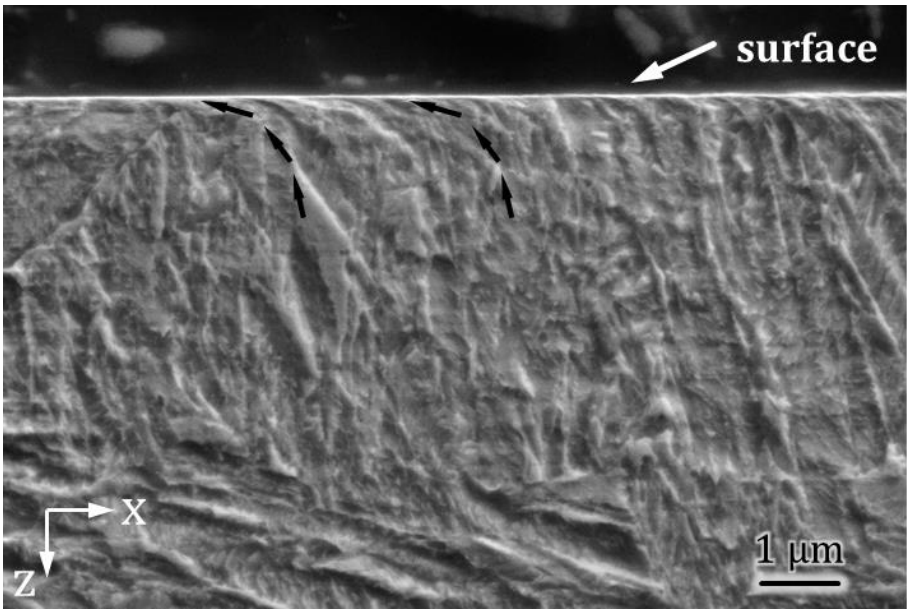

Figure 22: SEM image of cross-section of ground CS, a shear gradient is visible below the surface

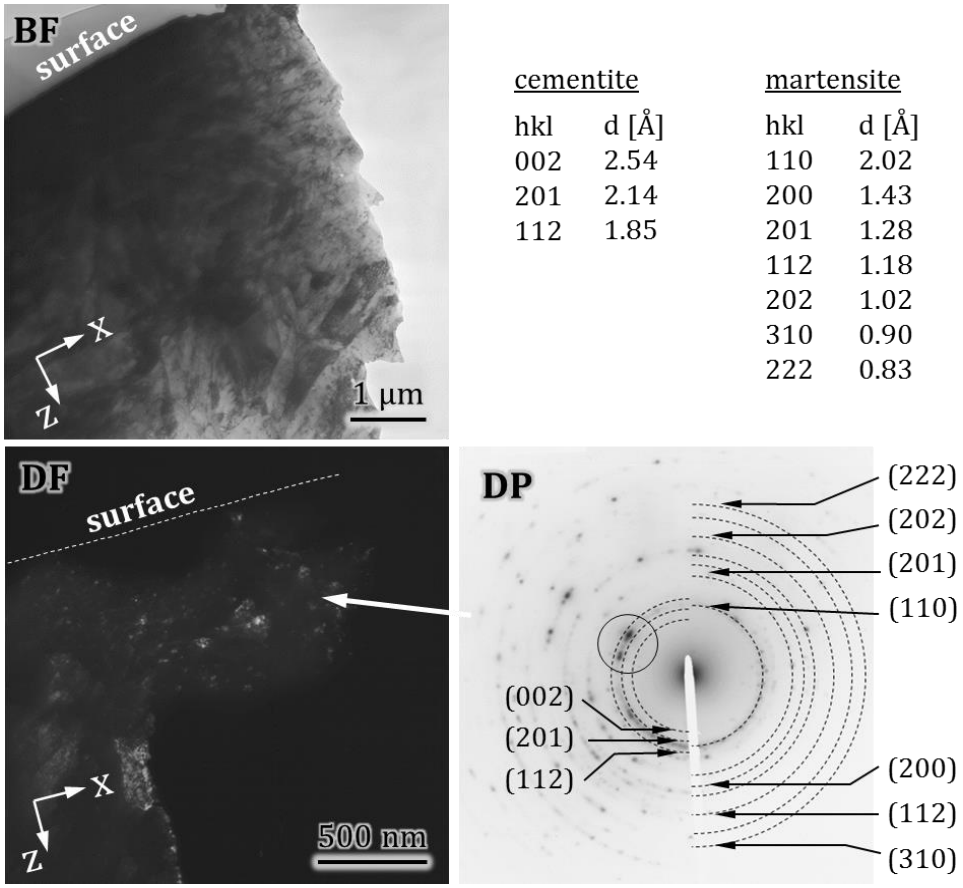

cementite		martensite	
hkl	d [Å]	hkl	d [Å]
002	2.54	110	2.02
201	2.14	200	1.43
112	1.85	201	1.28
		112	1.18
		202	1.02
		310	0.90
		222	0.83

Figure 23: TEM micrograph of ground CS, shows thin nc martensitic layer and cementite precipitates

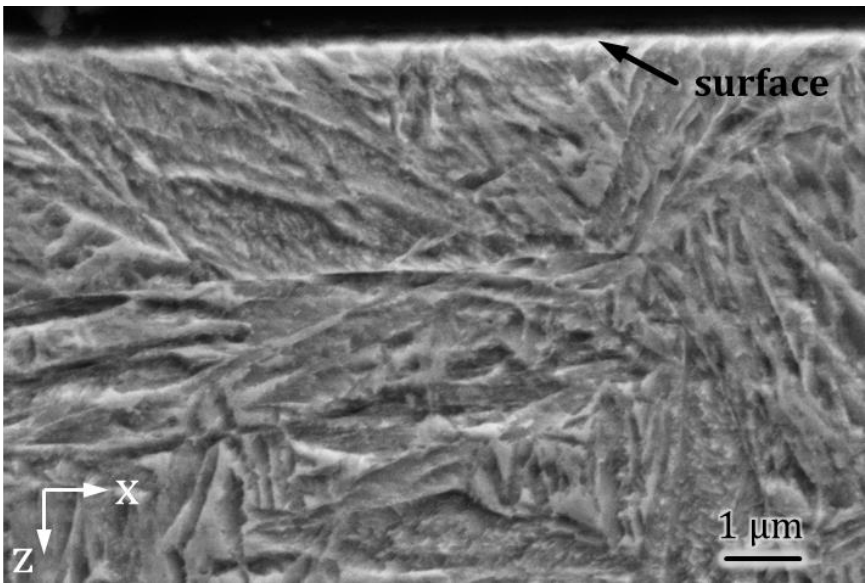

Figure 24: SEM cross-sectional image of honed CS shows no visible alterations towards the surface

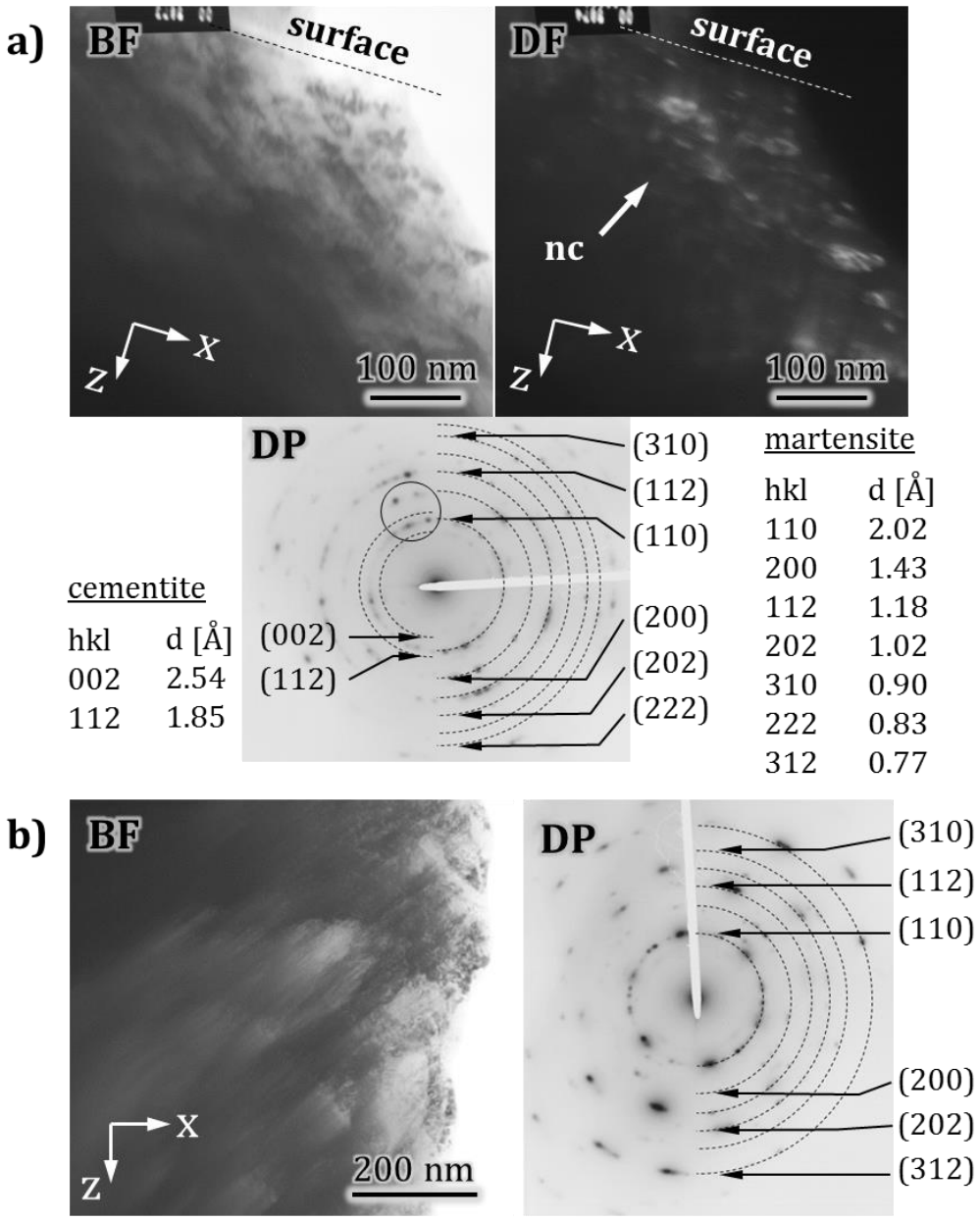

Figure 25: TEM images of honed CS a) nc near-surface zone and b) transition zone

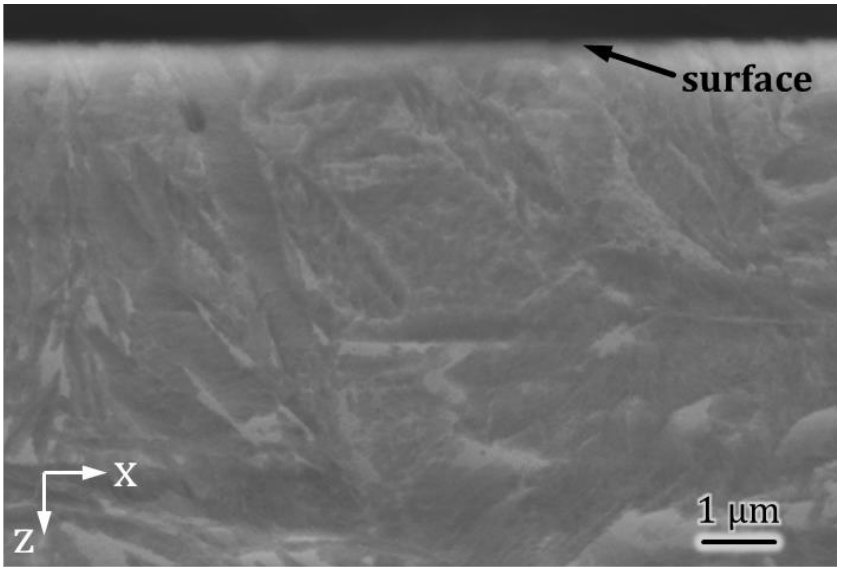

Figure 26: SEM cross-section image of polished CS reveals no visible microstructural alterations

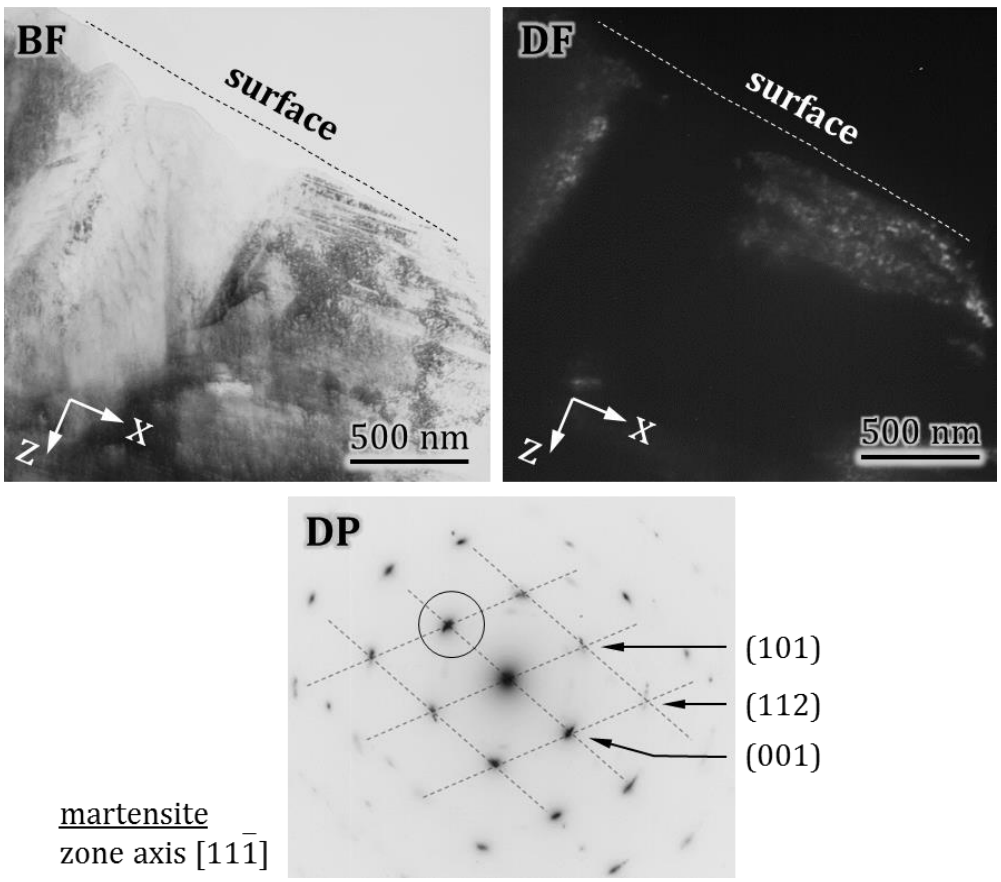

Figure 27: TEM image of near-surface region of polished CS base body shows µc martensite

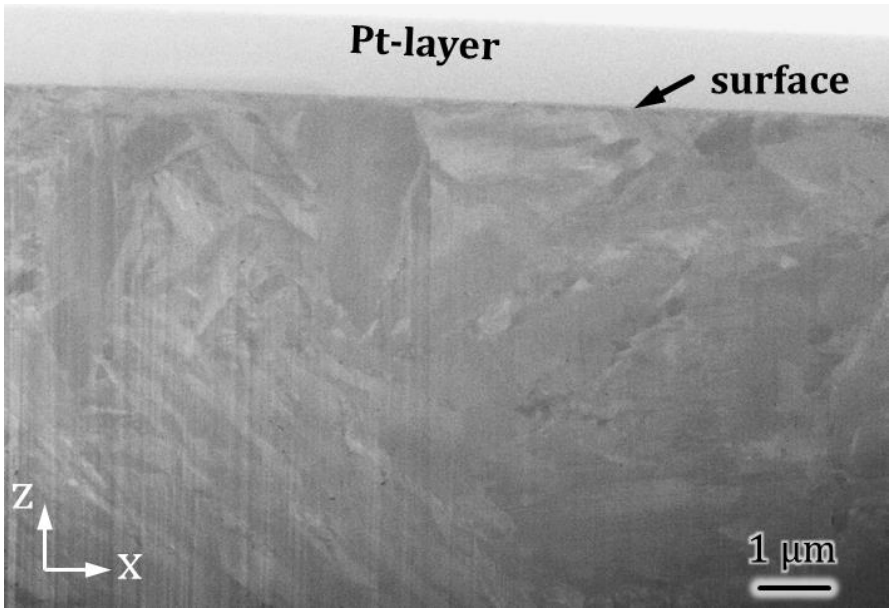

Figure 28: FIB cross-section of carburized steel counter body

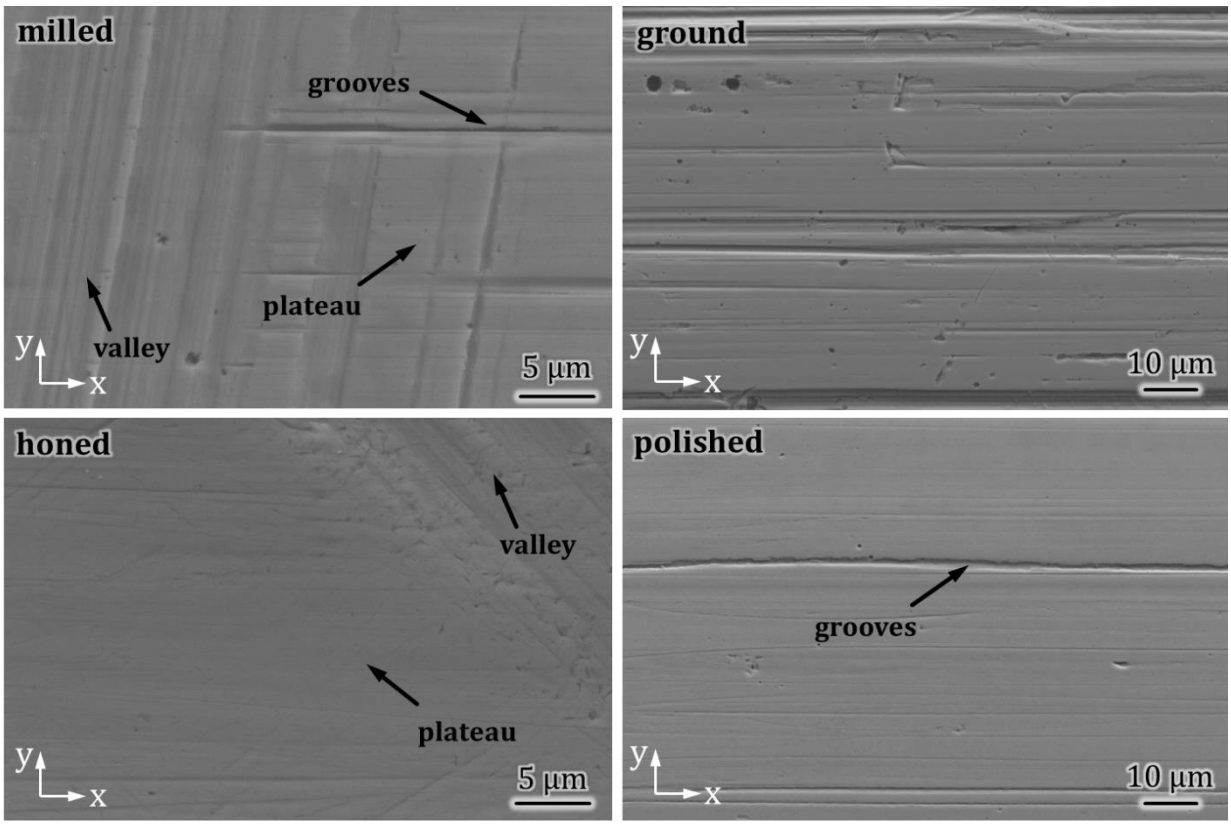

Figure 29: Worn surfaces of the CS base bodies reveal flattened asperities in the contact area, while some valleys from machining marks remained

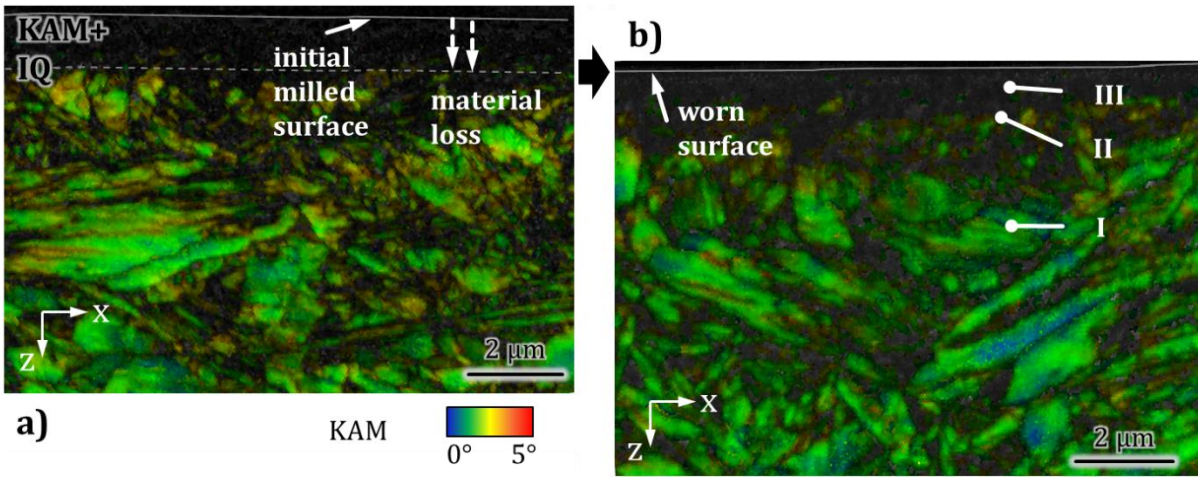

Figure 30: Cross-section of milled CS a) after manufacturing and b) after wear test; a) dashed line marks presumed surface after wear test, b) actual near-surface region after wear test exhibits similar structural gradient like the one after milling process

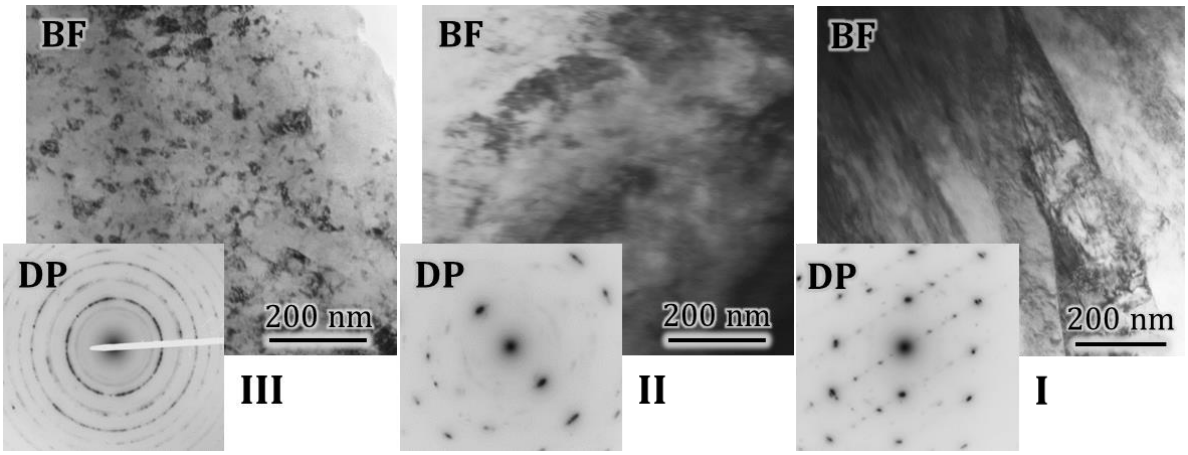

Figure 31: TEM micrographs displaying different microstructural appearances of the deformation gradient shown in Figure 30, (III) nc martensite, (II) transition zone, (I) martensite lathes, bulk structure

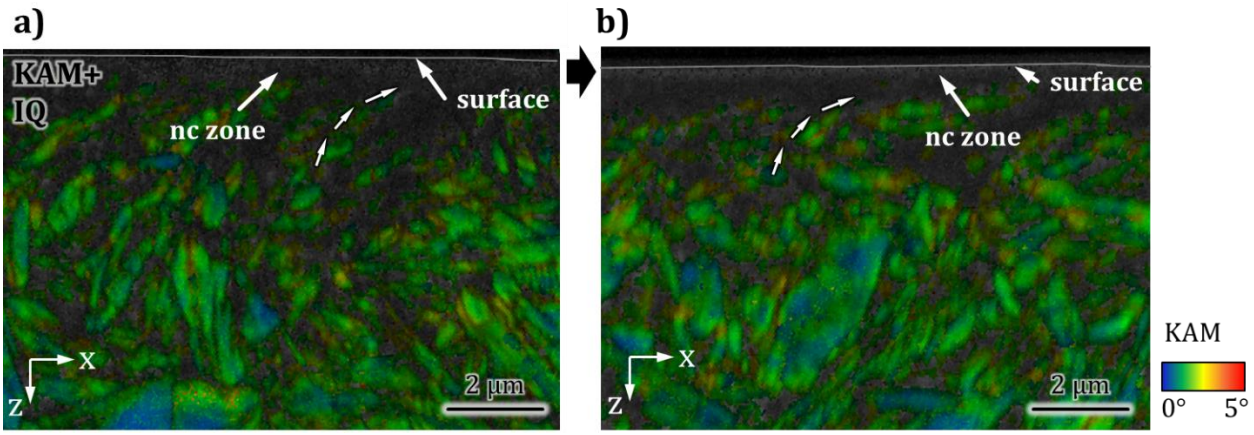

Figure 32: KAM maps of cross-sections of ground CS base body, a) unworn and b) worn

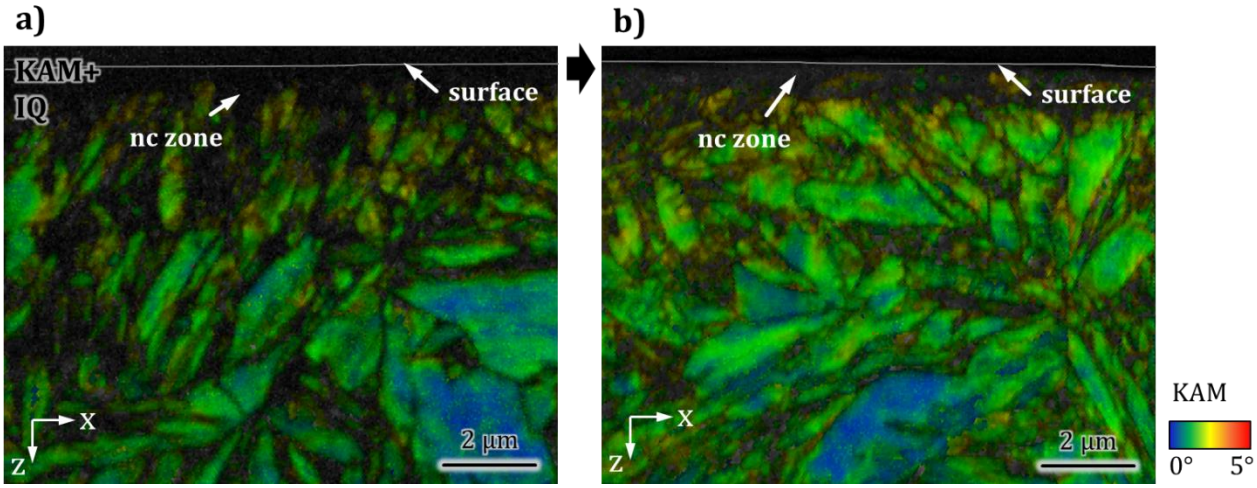

Figure 33: Honed CS a) after manufacturing and b) after tribotest, KAM maps exhibit no visible near-surface alteration during wear test

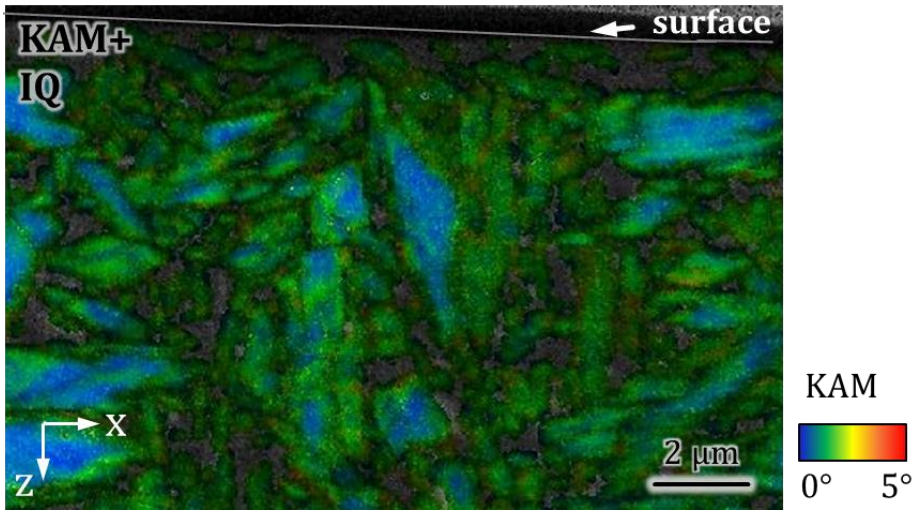

Figure 34: KAM map of the polished CS BB after wear test shows moderate grain refinement of the near-surface region

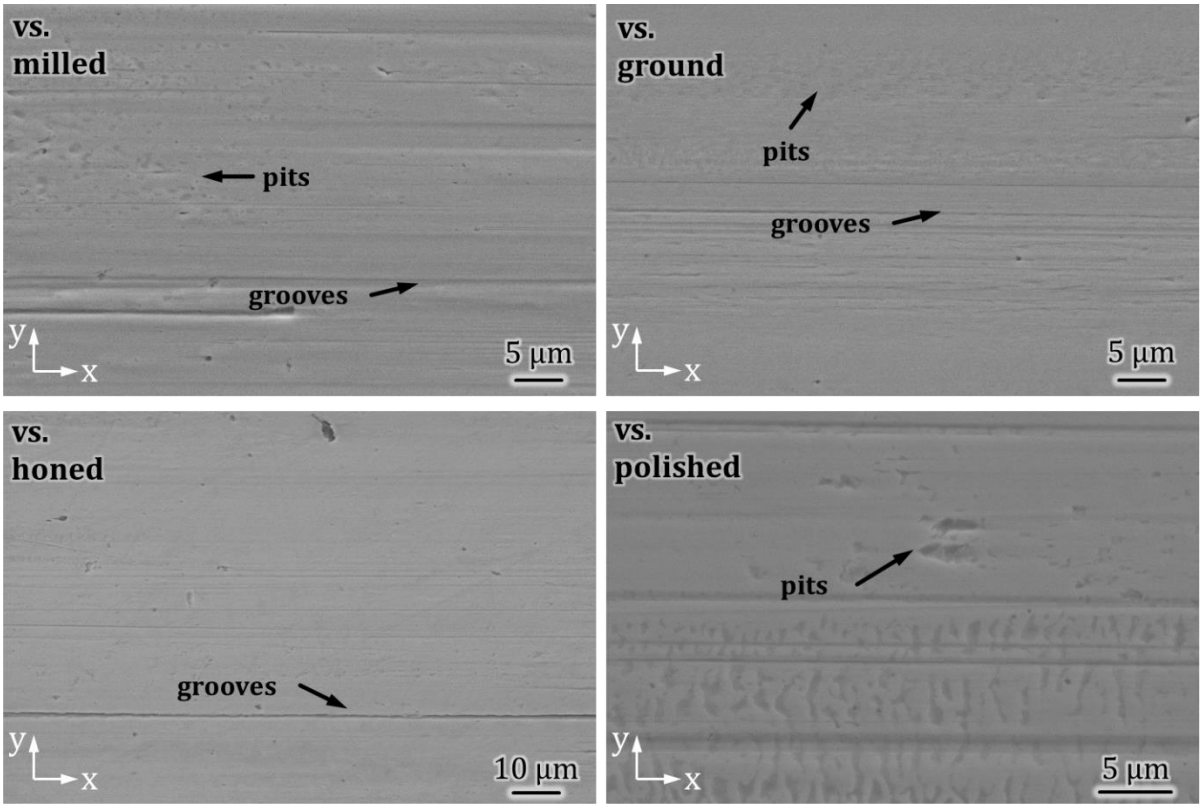

Figure 35: Contact areas of the CS counter bodies

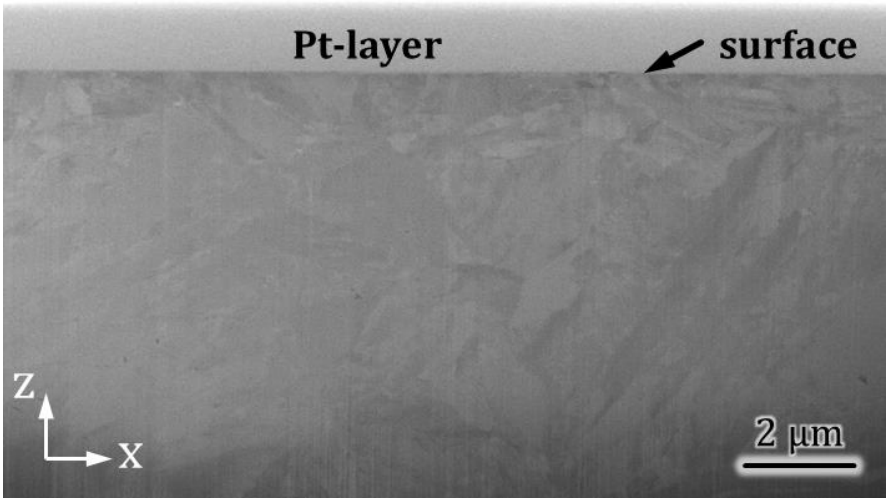

Figure 36: FIB cross-section of the carburized steel CB tested against the milled BB

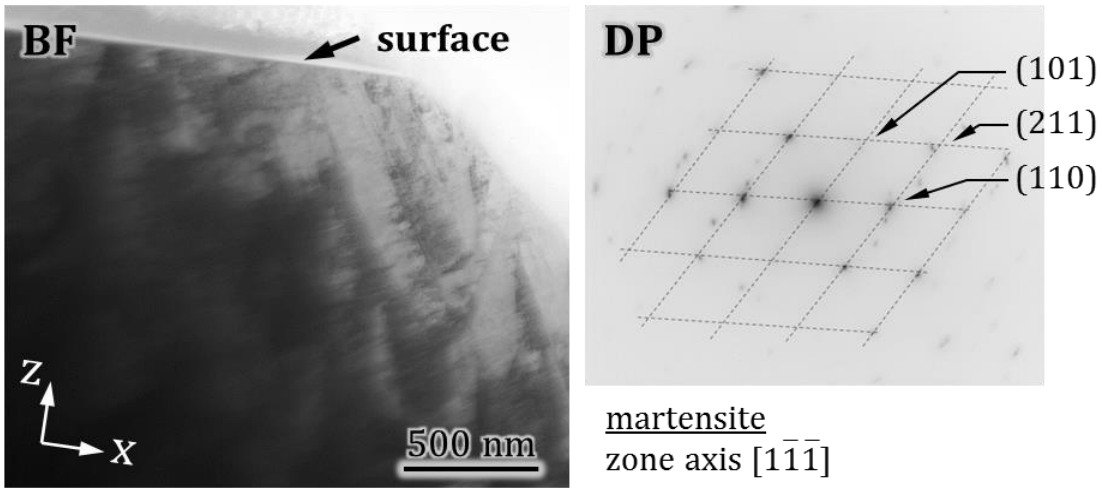

Figure 37: TEM image of the carburized steel CB tested against the ground BB

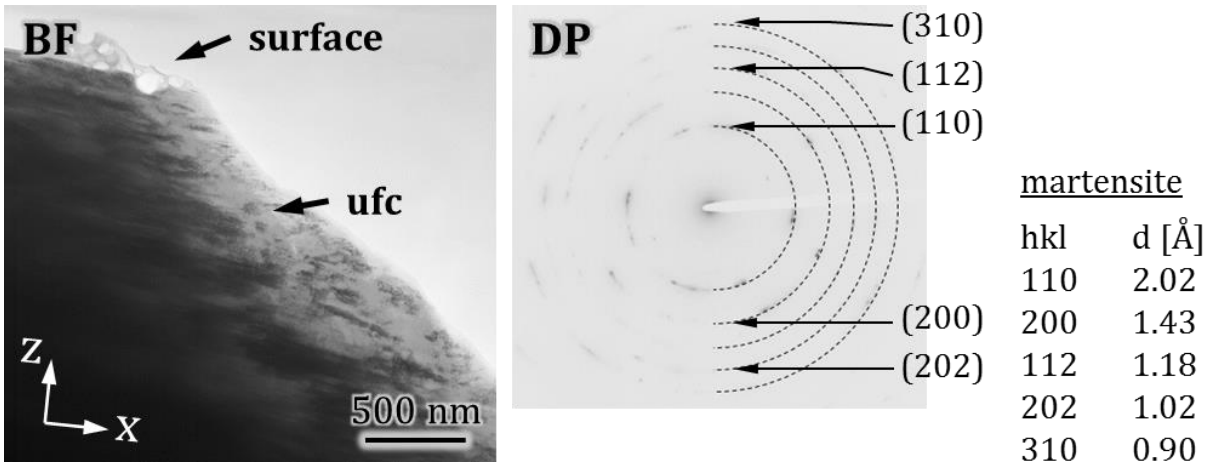

Figure 38: TEM micrograph of the carburized steel CB tested against the honed BB

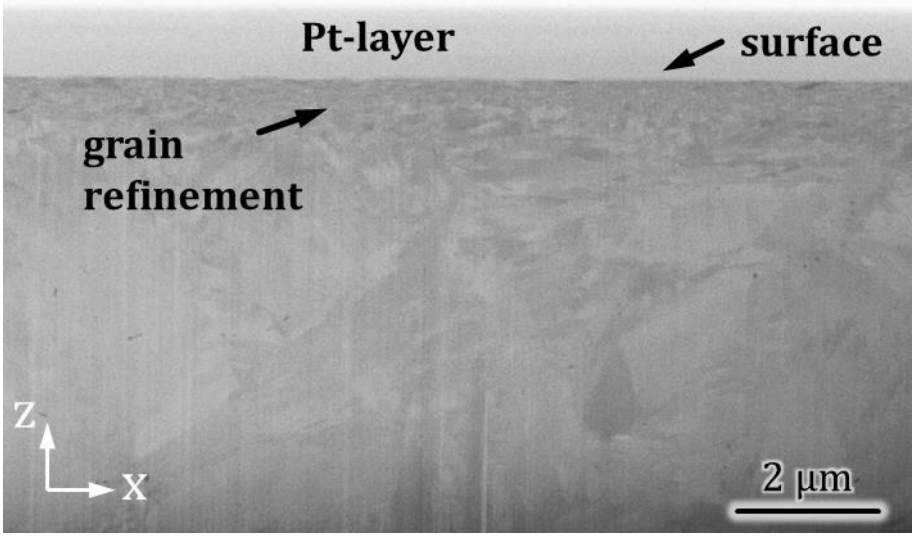

Figure 39: FIB cross-section of the carburized steel CB tested against the polished BB

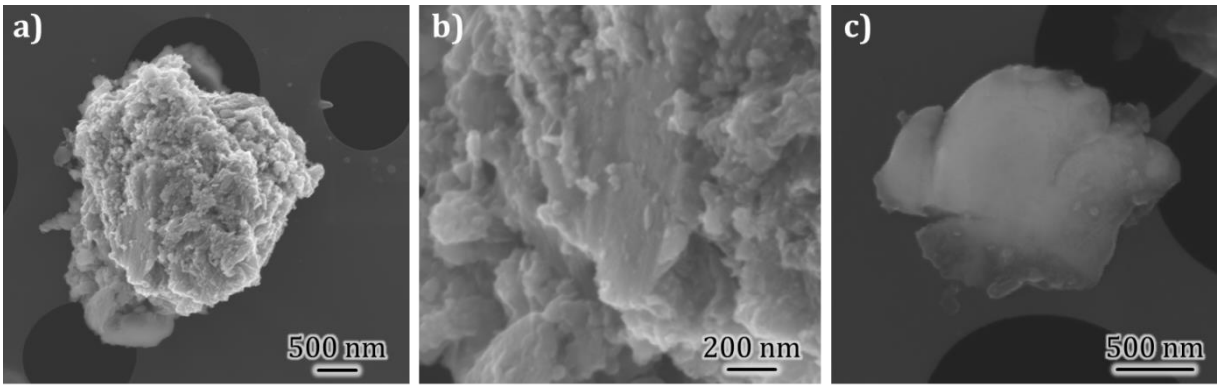

Figure 40: SEM images of debris from self-mating CS wear tests, a) agglomerate of mostly nm-sized particles, b) detailed view of a), c) larger wear particle

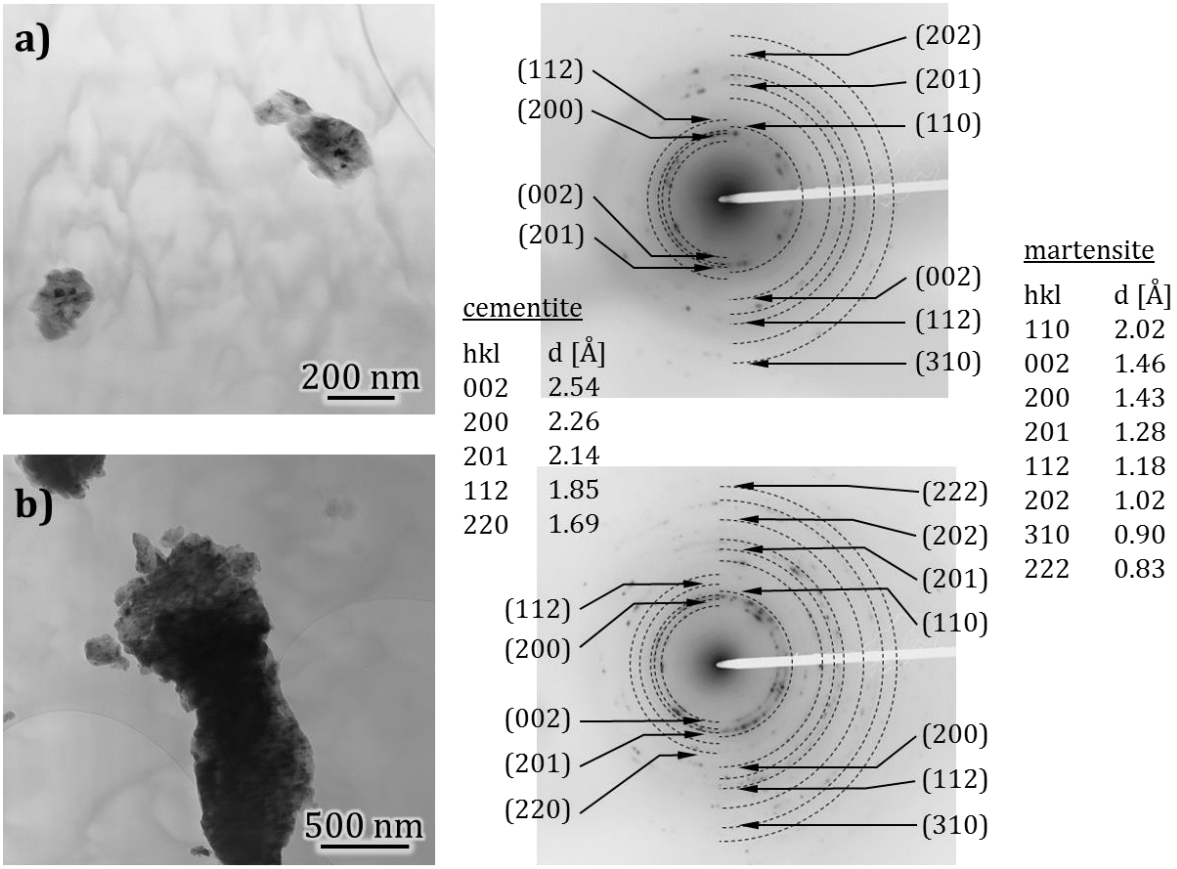

Figure 41: TEM micrographs of particles extracted after CS wear tests

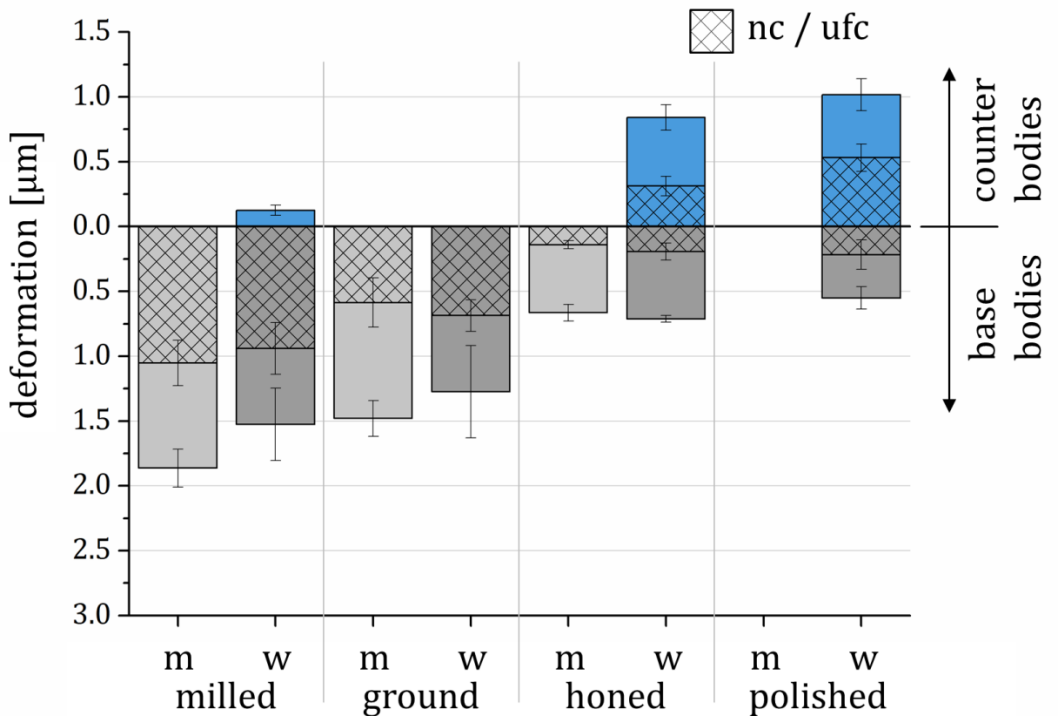

Figure 42: Deformation depths of machined (m) and worn (w) carburized steel samples

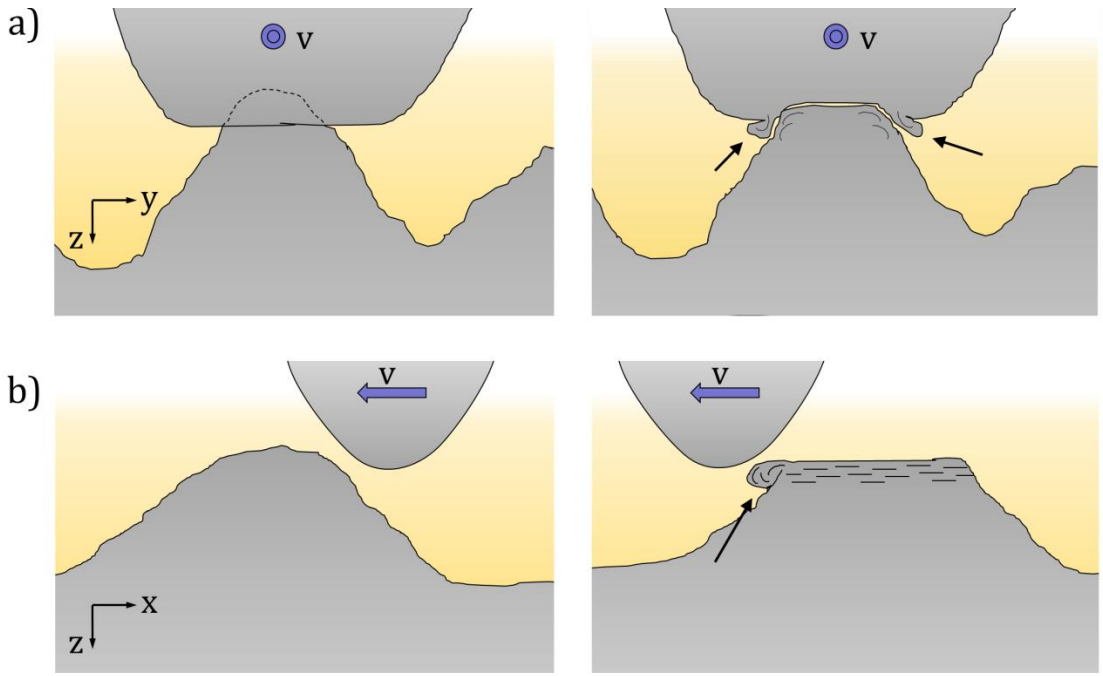

Figure 43: Schematic illustration of the influence of the machining mark orientation on damage mechanism (a) for the ground and (b) for the milled specimen

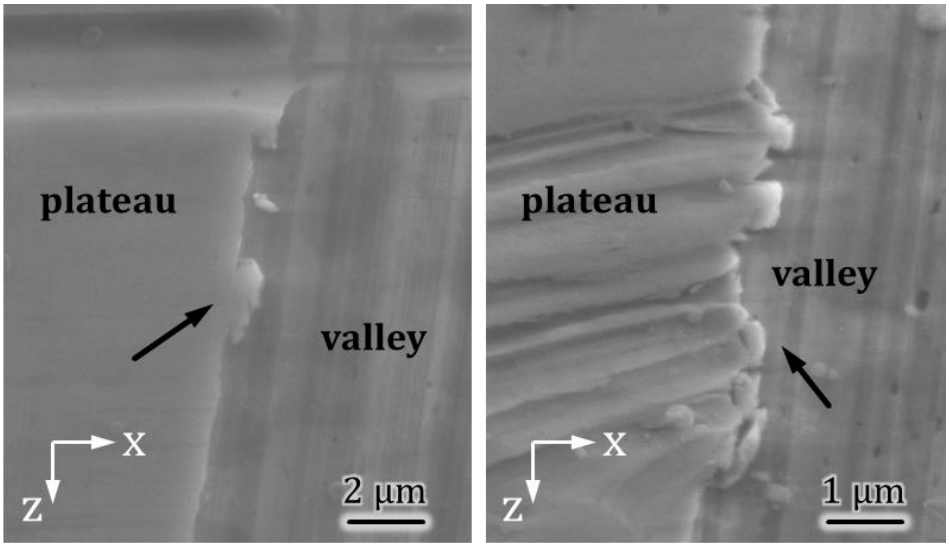

Figure 44: SEM image shows a detailed view of the milled carburized steel wear track, material is pushed out at the transition from plateau to valley leading to particle formation

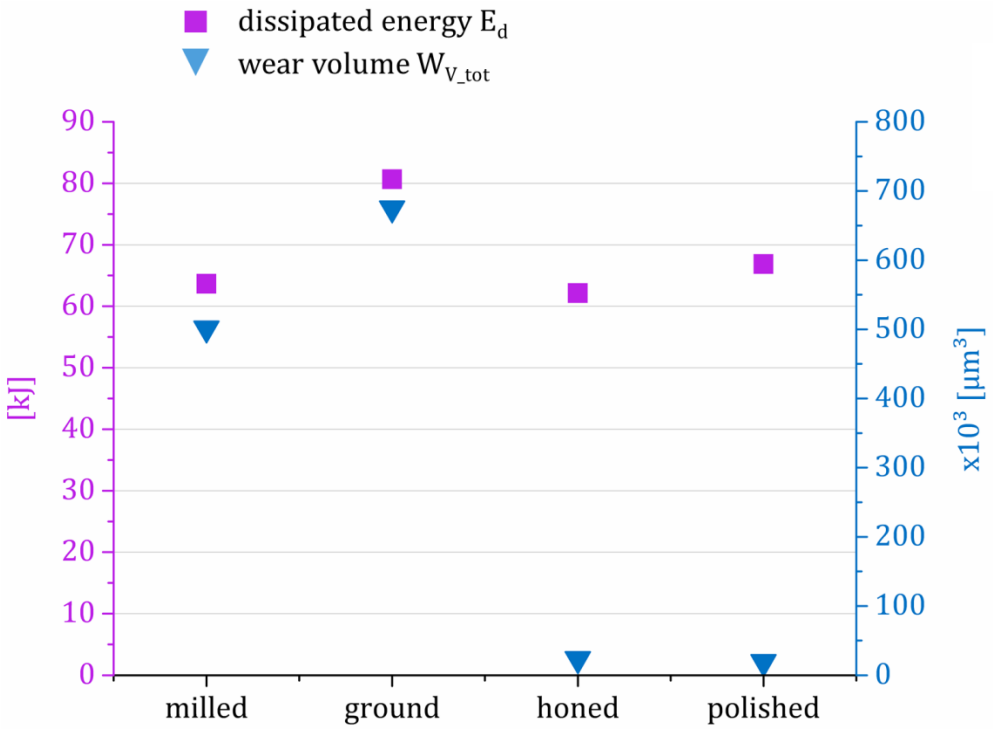

Figure 45: Dissipated friction energy and total wear volume for the carburized steel tribocouples

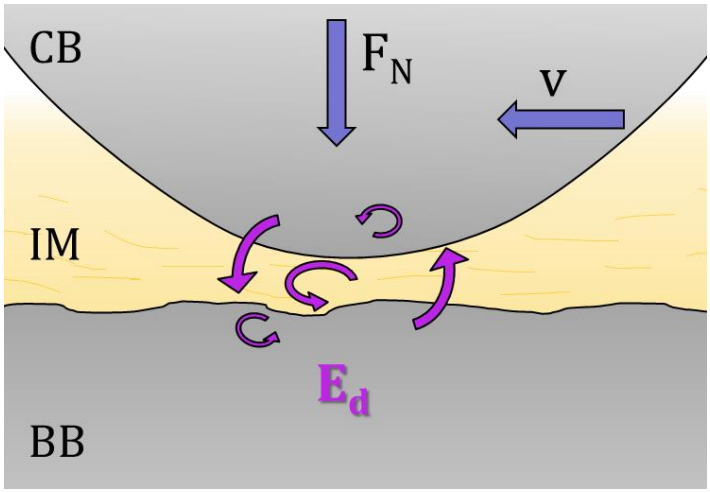

Figure 46: Energy dissipation can occur in all three elements of a tribosystem, the amount of dissipated energy (E_d) is different for base body (BB), counter body (CB) and interfacial medium (IM)

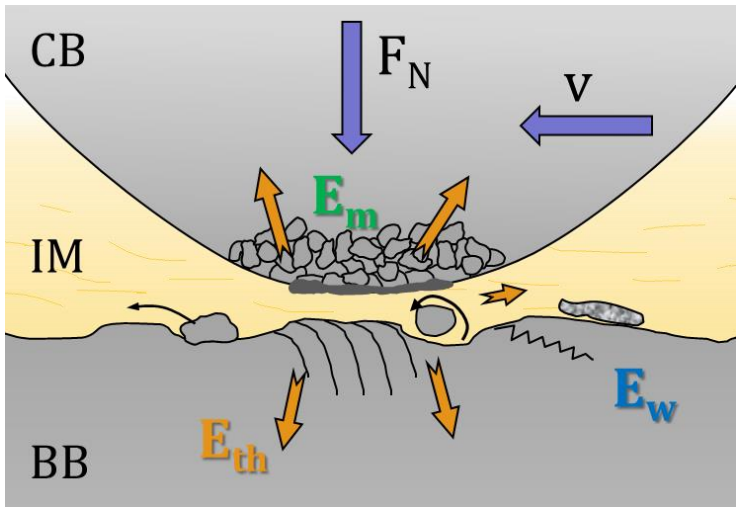

Figure 47: Processes causing heat (E_{th}), material transformation (E_m) or material loss (E_w) as well as secondary processes contribute to the dissipated friction energy

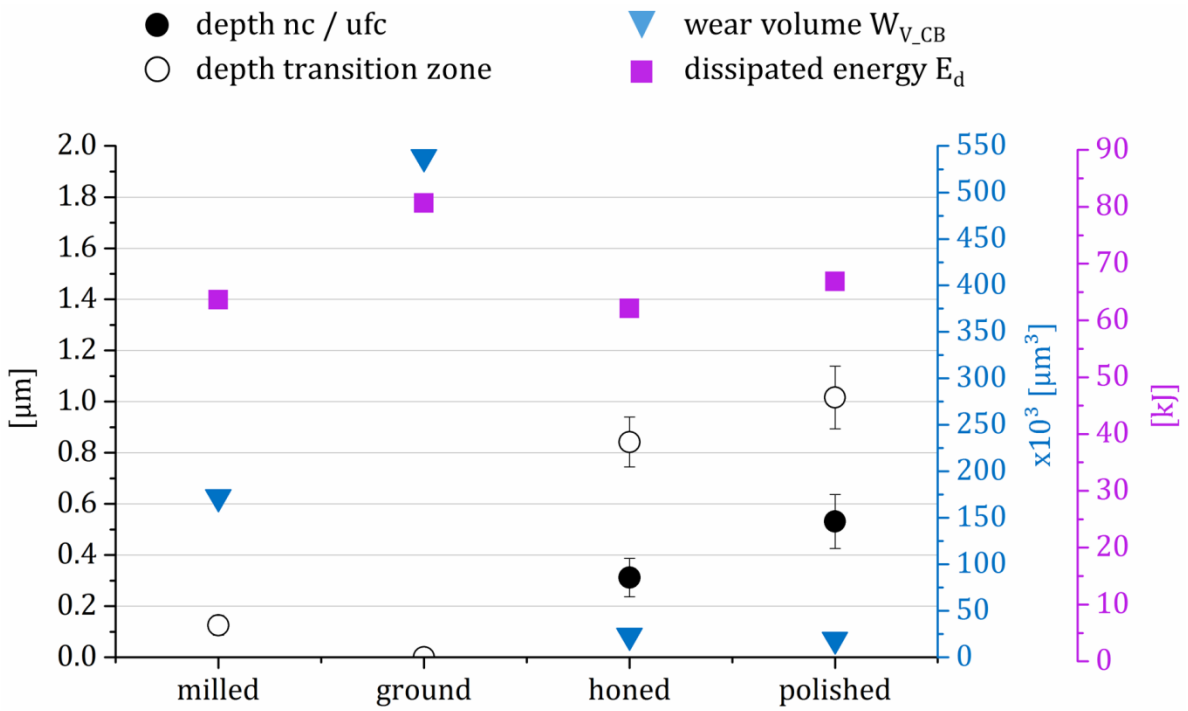

Figure 48: Dissipated friction energy linked to the wear volumes and deformation depths of the carburized steel counter bodies

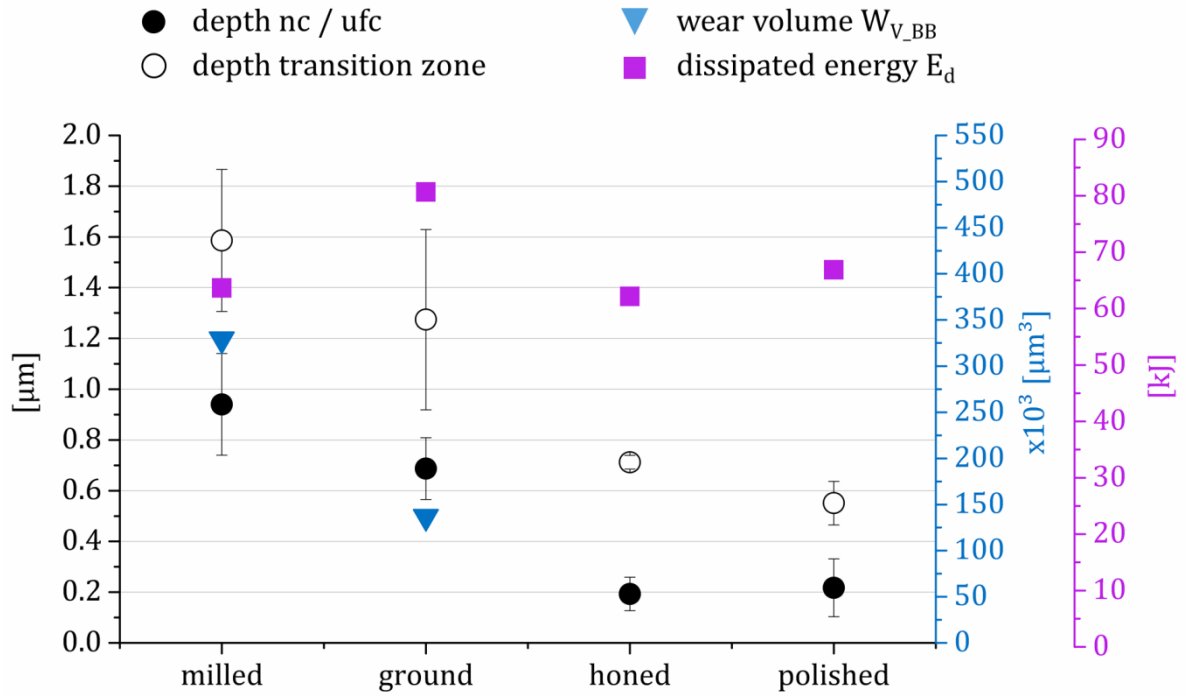

Figure 49: Dissipated friction energy linked to the wear volumes and deformation depths of the carburized steel base bodies

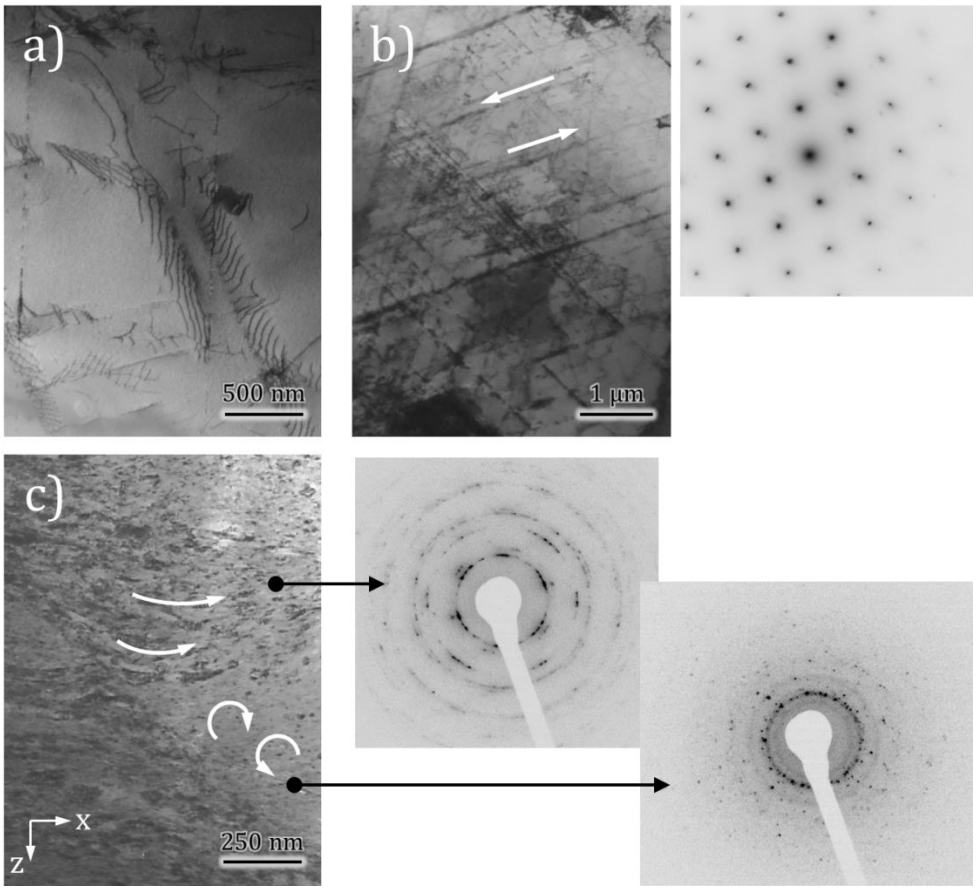

Figure 50: Deformation processes: (a) dislocation formation, (b) plastic flow, (c) grain boundary sliding and grain rotation

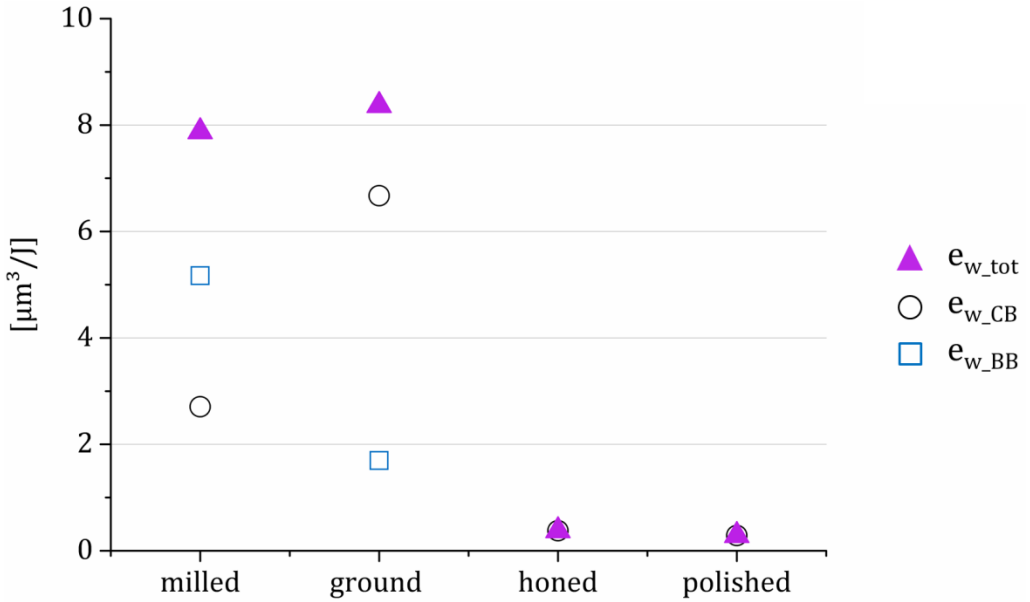

Figure 51: Energy-based wear rates e_w for the carburized steel tribocouples display the dissipated energy related to the total wear volumes (w_tot) and to the wear volumes of counter (w_CB) and base bodies (w_BB)

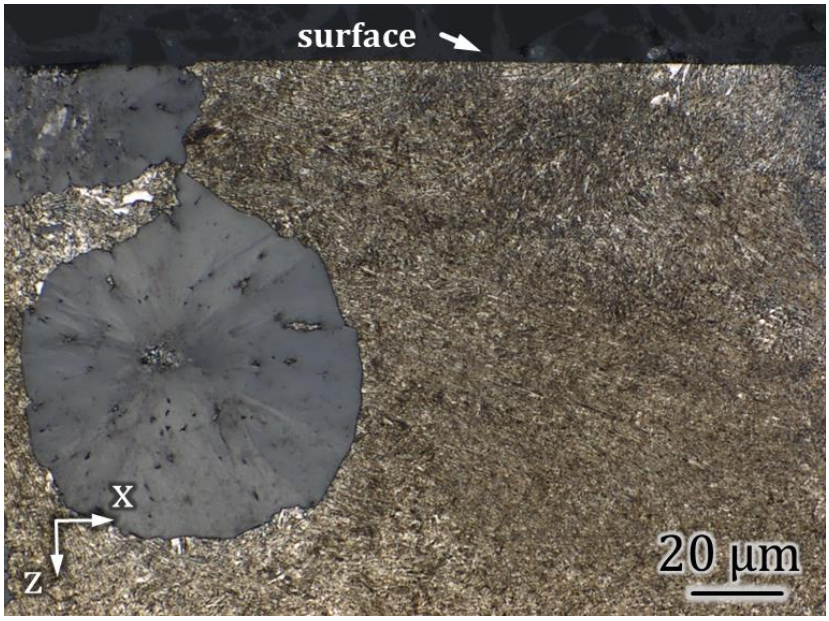

Figure 52: Optical micrograph of the cross-section of cast iron after heat treatment

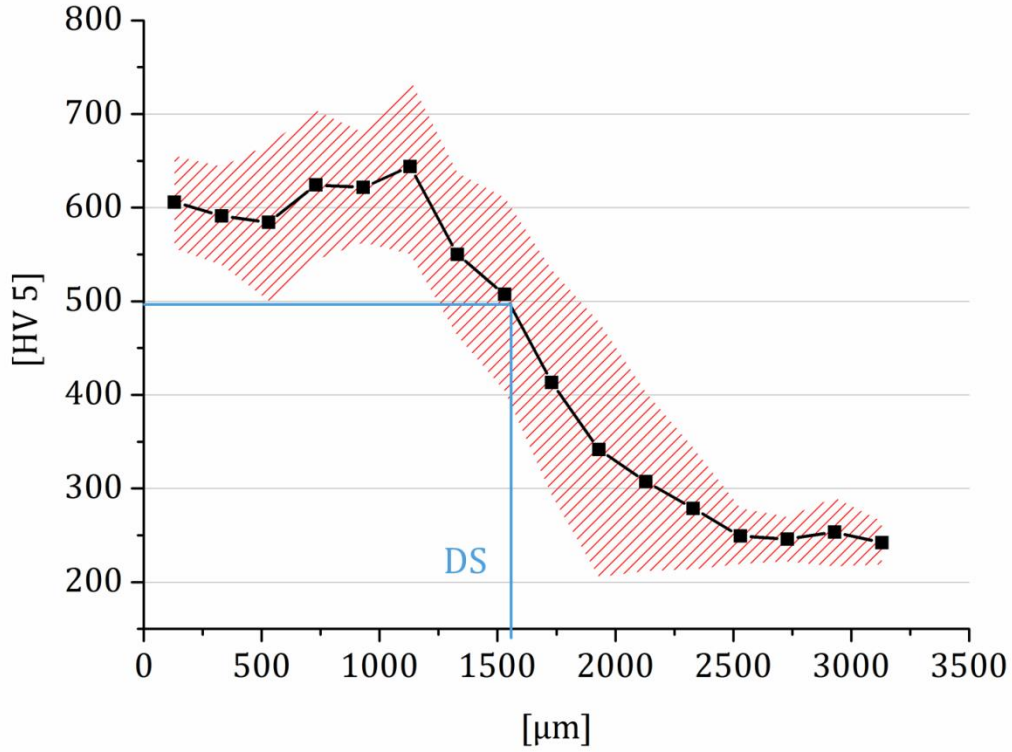

Figure 53: Hardness depth profile of cast iron

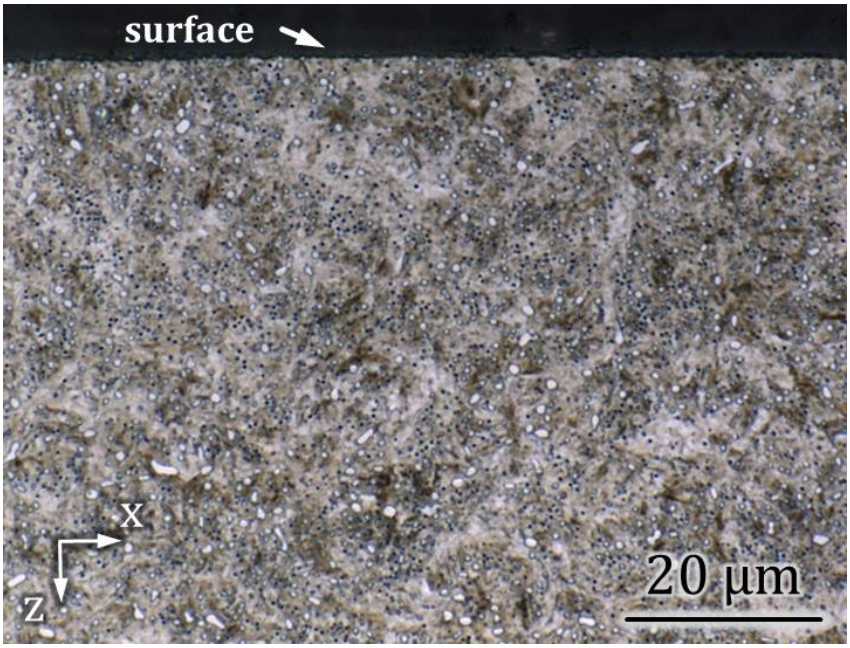

Figure 54: Optical micrograph of the cross-section of a bearing steel counter body

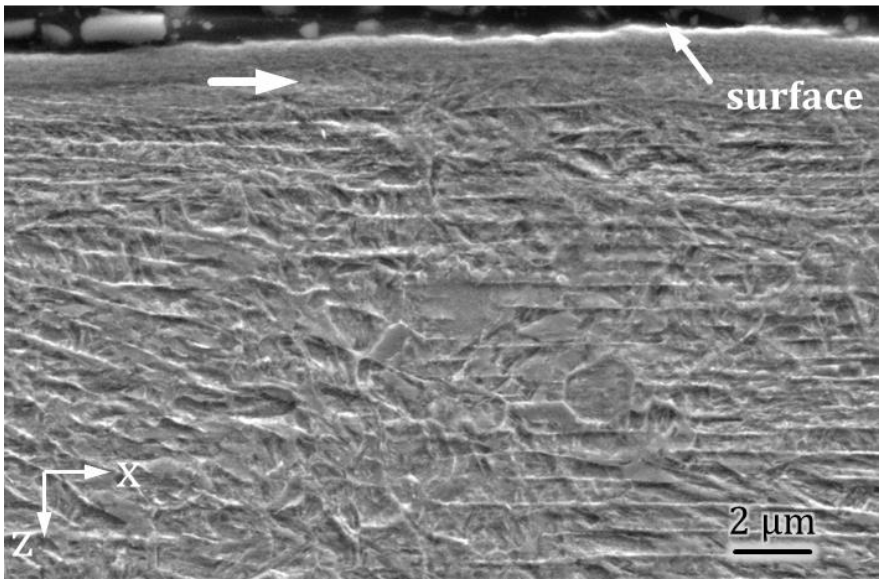

Figure 55: Milled CI exhibits severe plastic deformation of the near-surface zone, arrow indicates transition to bulk structure

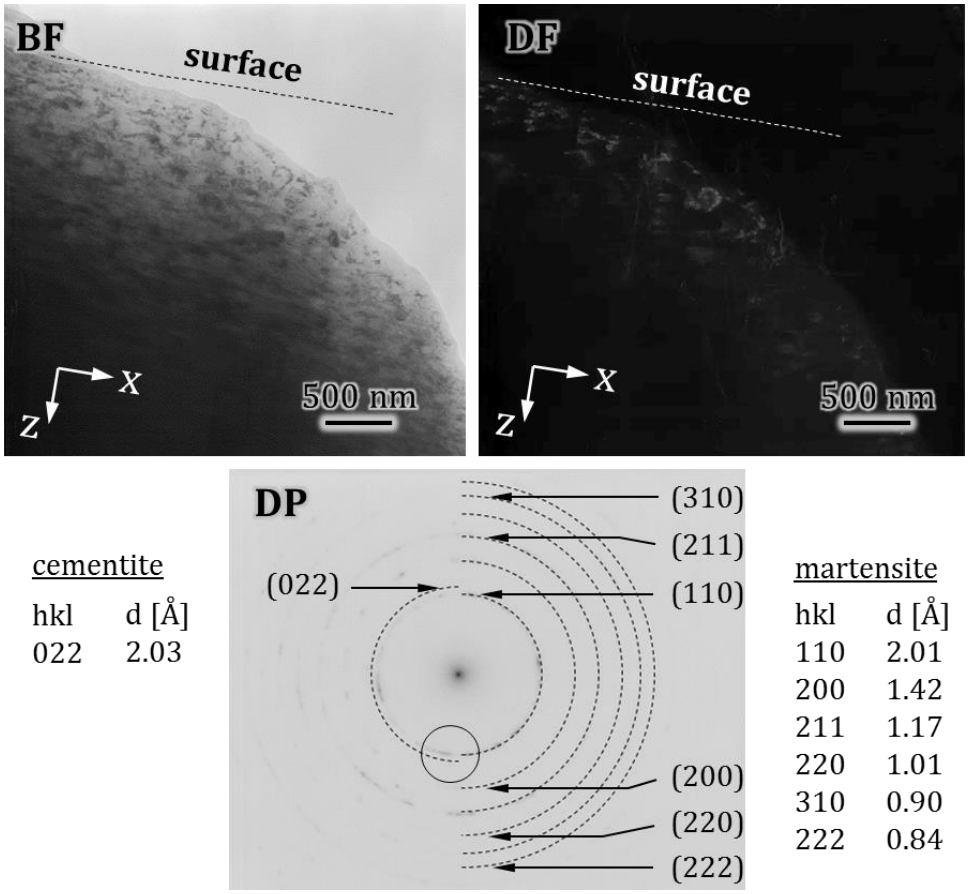

Figure 56: TEM micrograph of milled CI near-surface zone reveals a nc structure

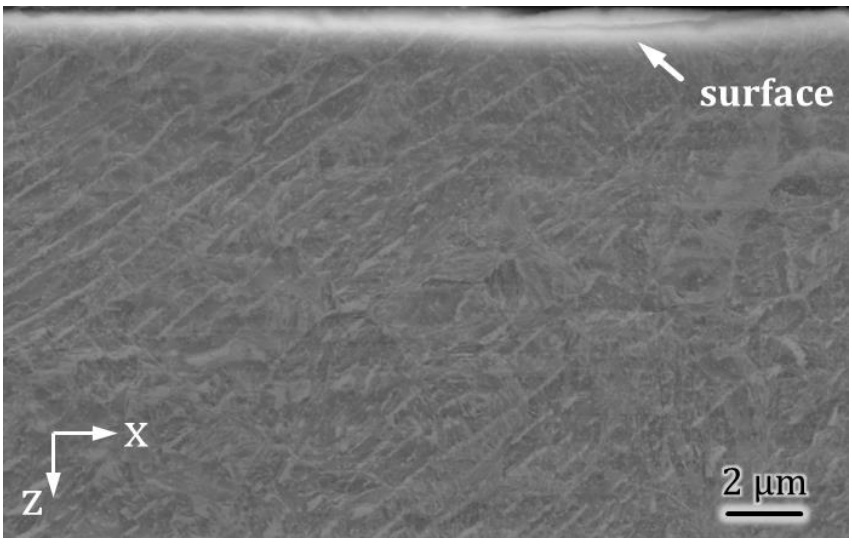

Figure 57: SEM image of ground CI cross-section shows cementite plates within the martensitic matrix

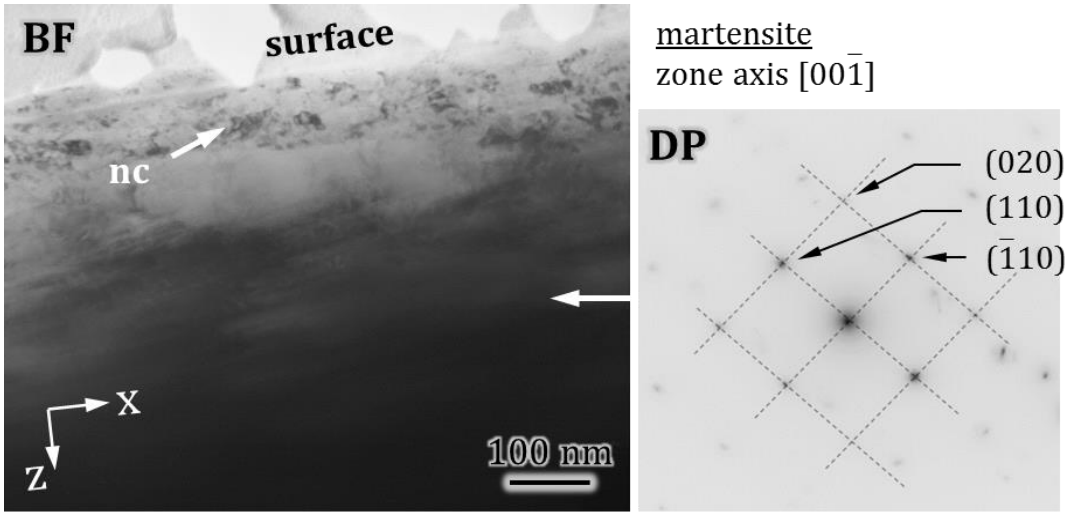

Figure 58: TEM image of ground CI shows distinctive boundary between nc layer and subsurface structure

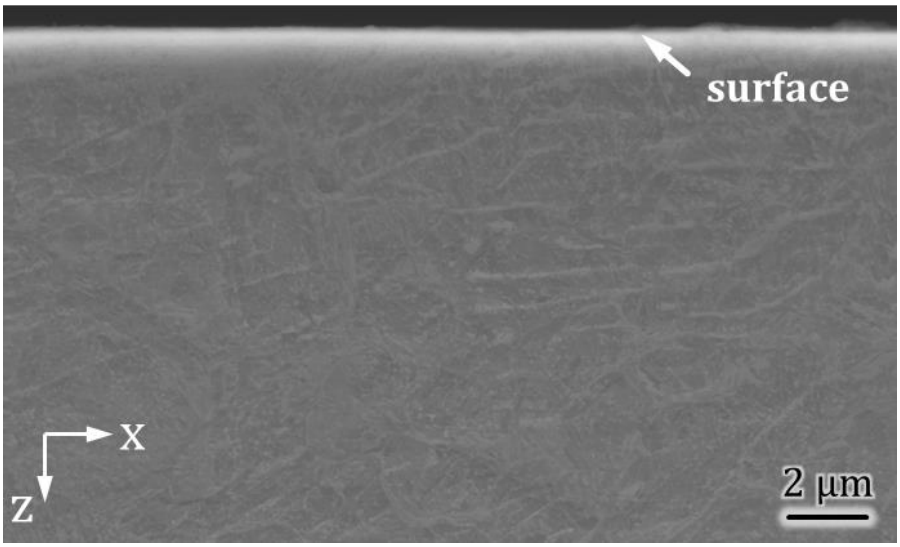

Figure 59: SEM image of honed CI cross-section shows no visible alterations

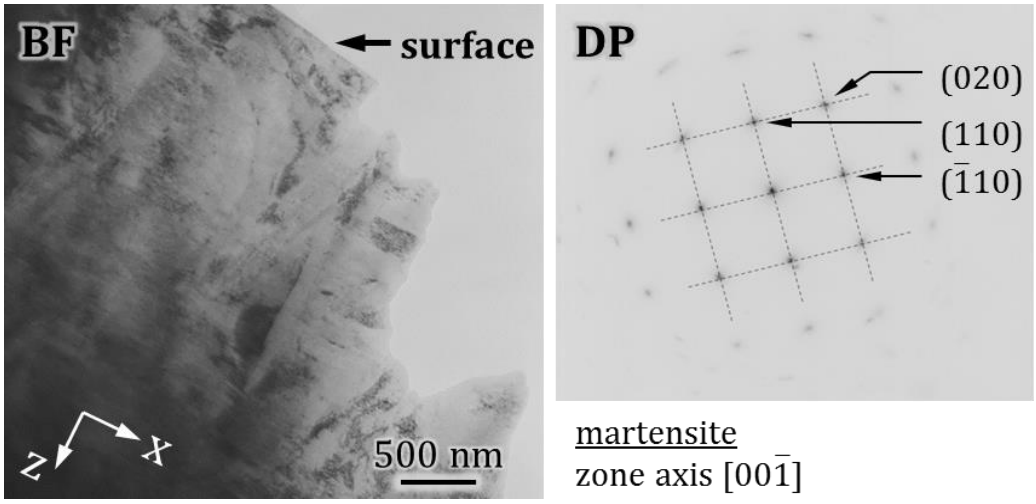

Figure 60: TEM image of honed cast iron shows no microstructural alterations of the near-surface zone

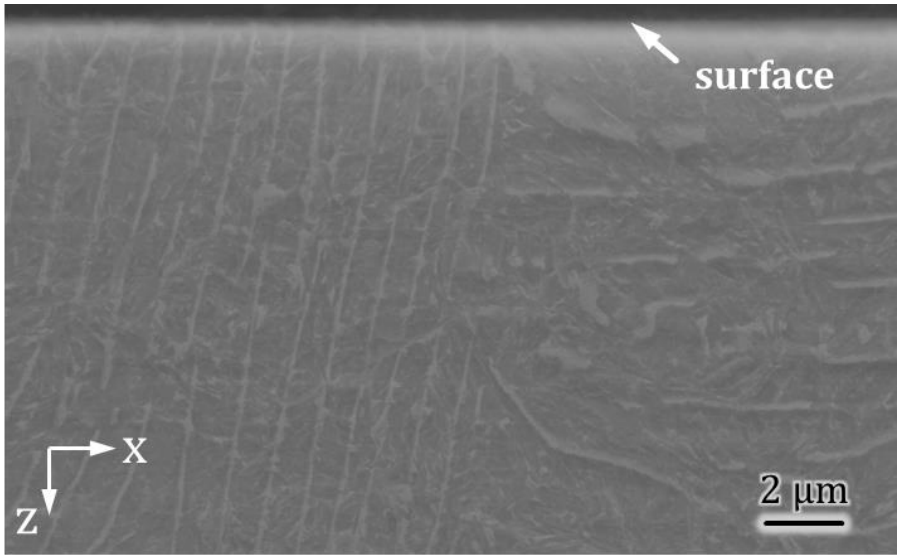

Figure 61: SEM cross-section of polished CI reveals no alterations of the near-surface zone

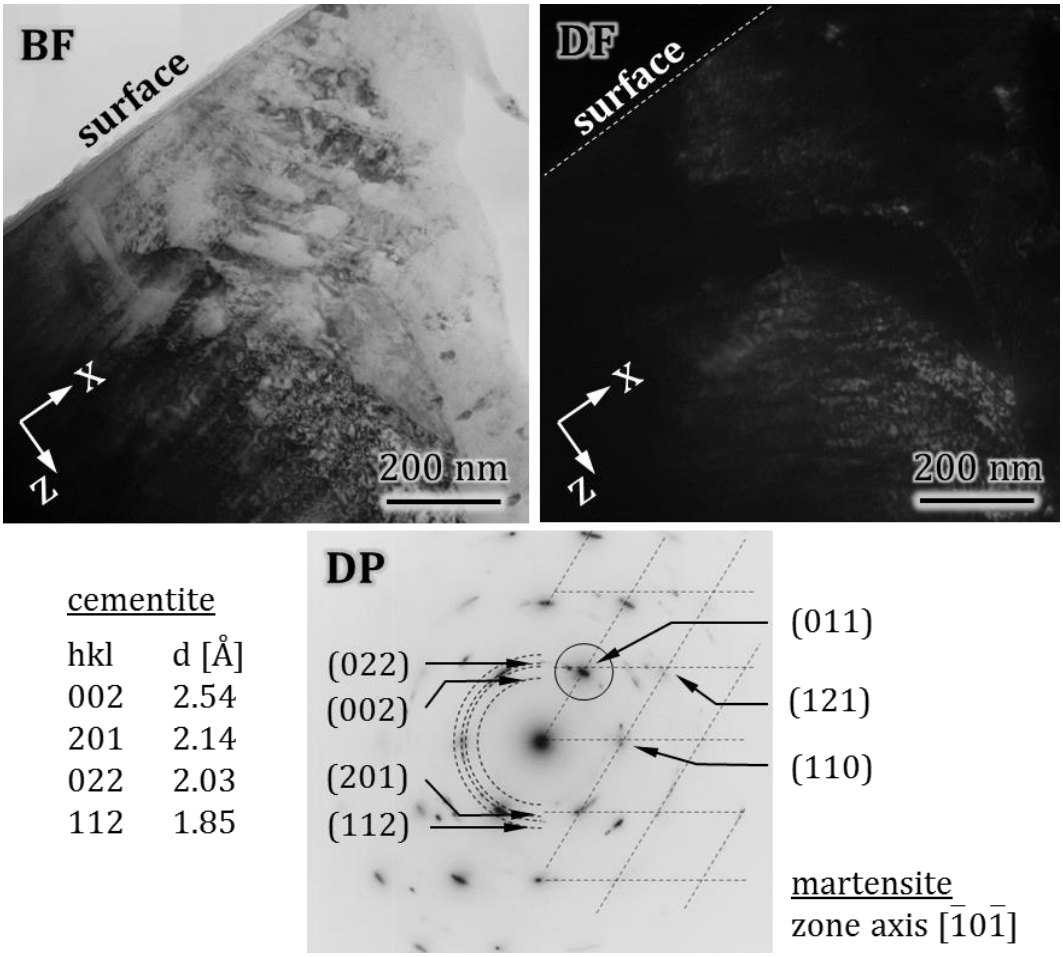

Figure 62: TEM images of the near-surface zone of the polished cast iron sample shows µc martensite matrix and some cementite reflexes

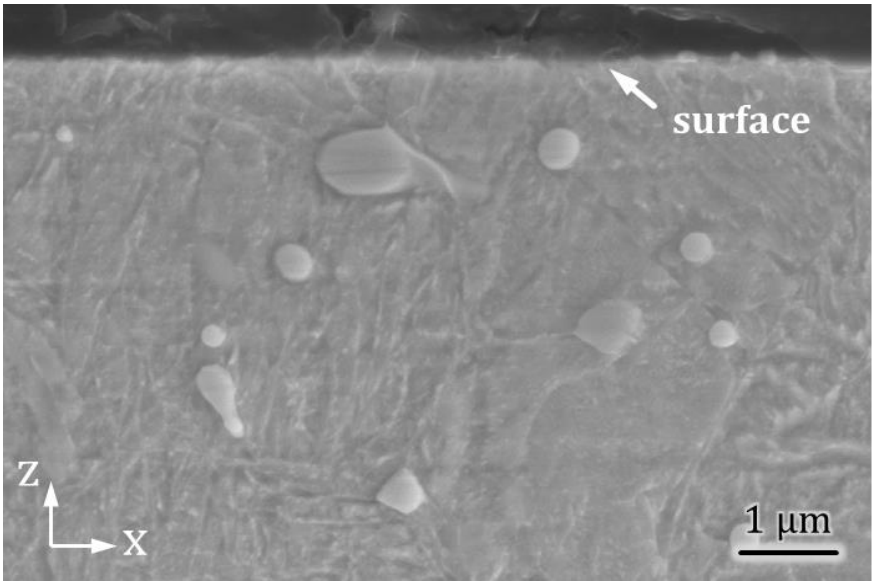

Figure 63: SEM cross-sectional image of the bearing steel counter body shows no visible alterations of the near-surface zone

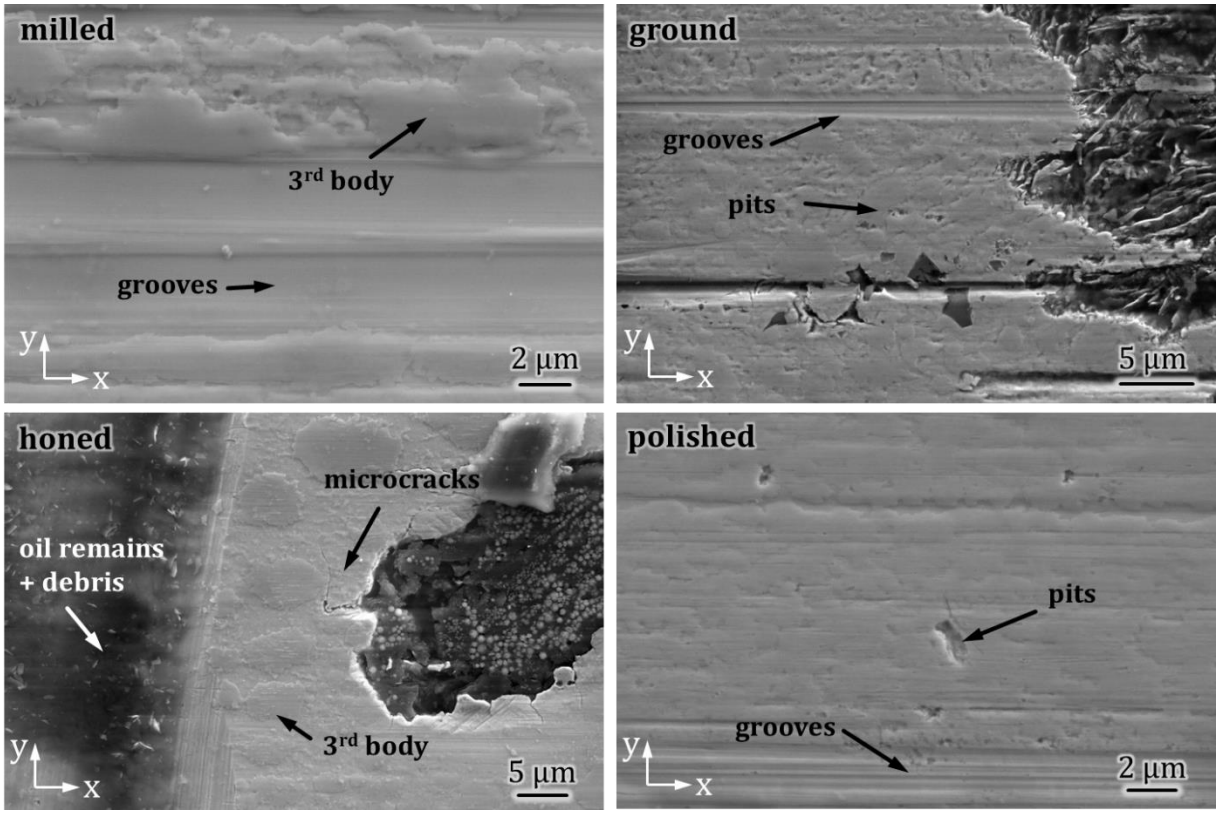

Figure 64: SEM images of the wear tracks of the cast iron base bodies

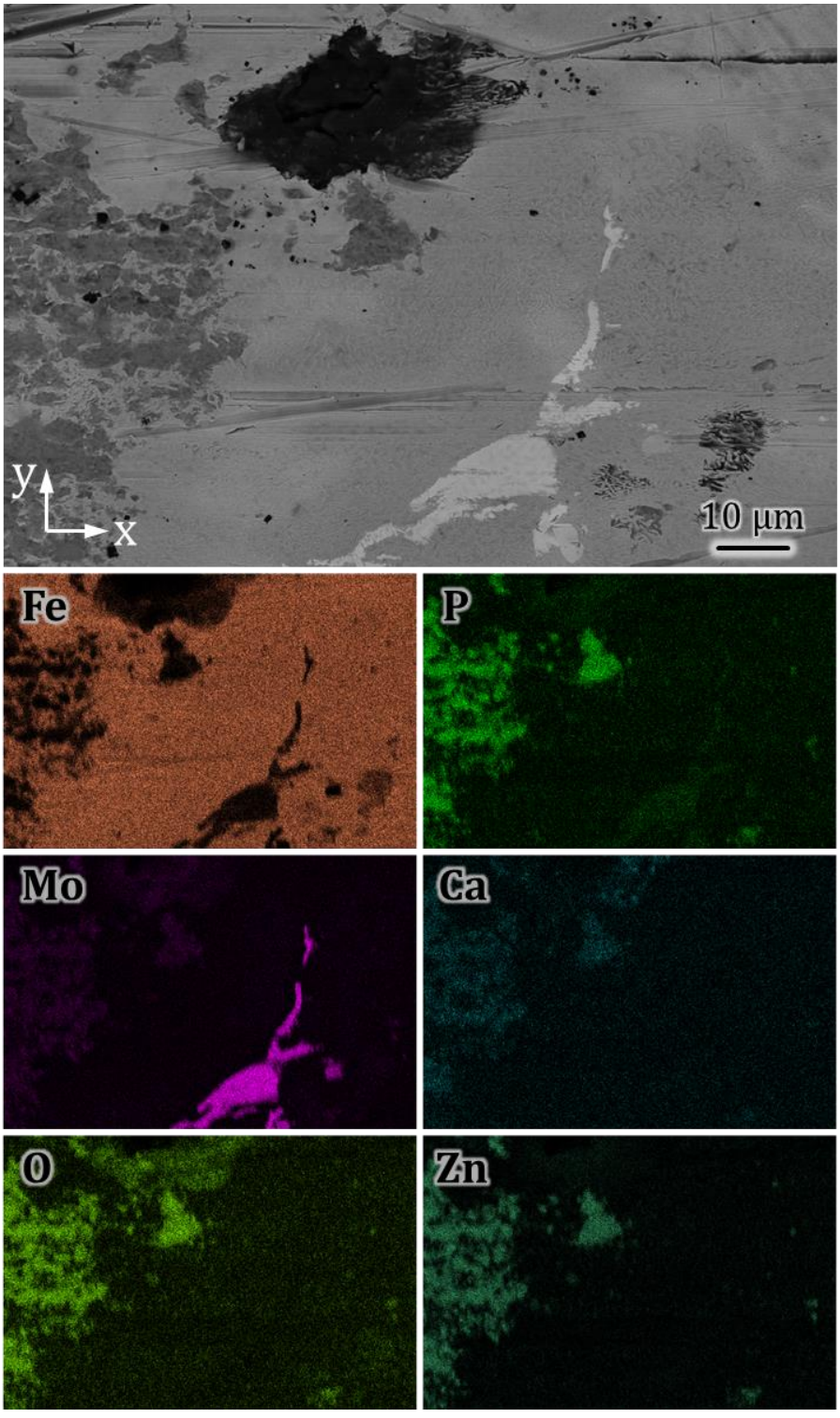

Figure 65: EDS maps taken within the wear track of the ground CI sample

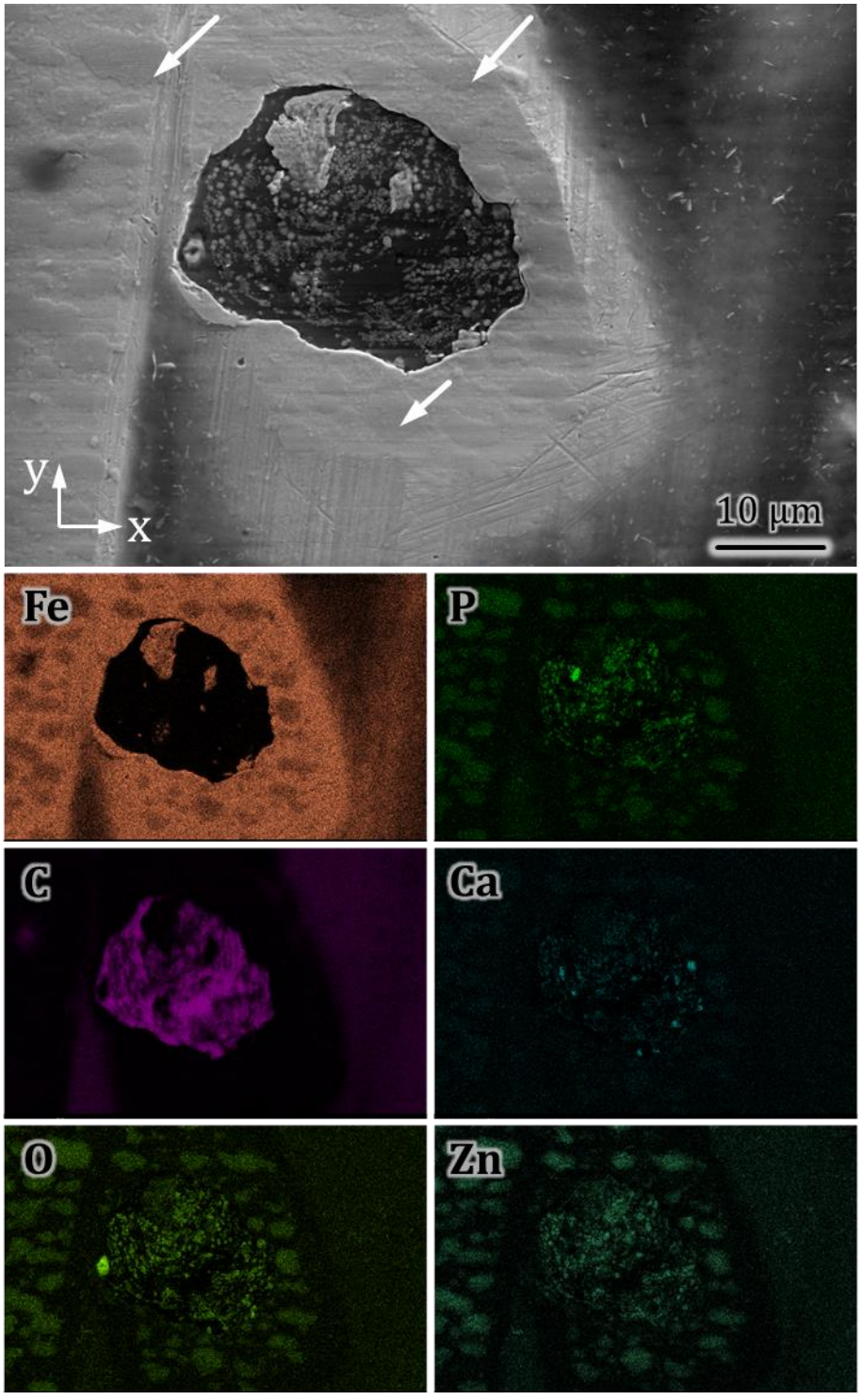

Figure 66: Elemental maps of the contact area of the honed CI reveal a patchy third-body

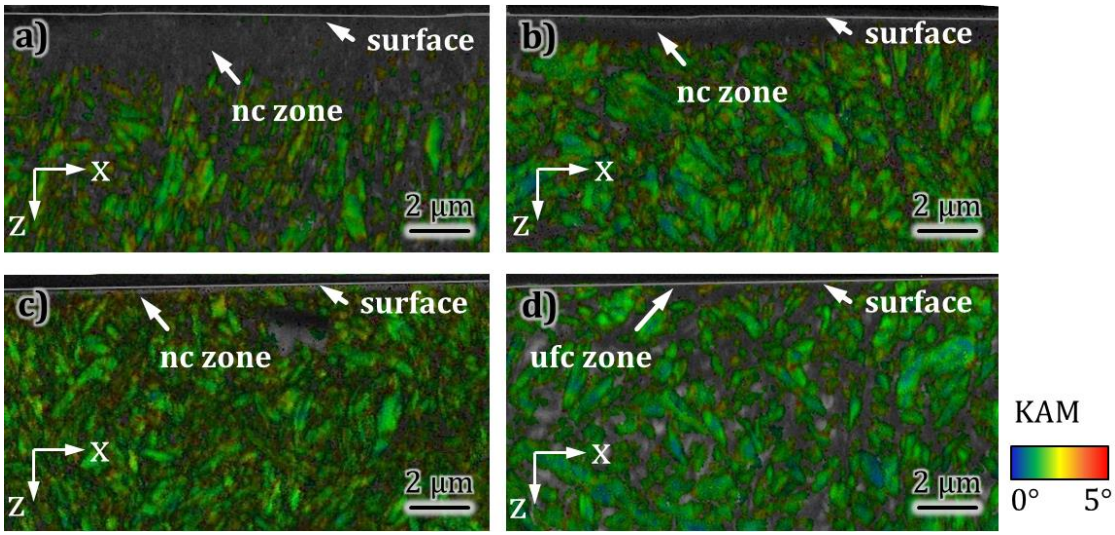

Figure 67: KAM maps of worn cast iron cross-sections of the (a) milled, (b) ground, (c) honed and (d) polished base bodies

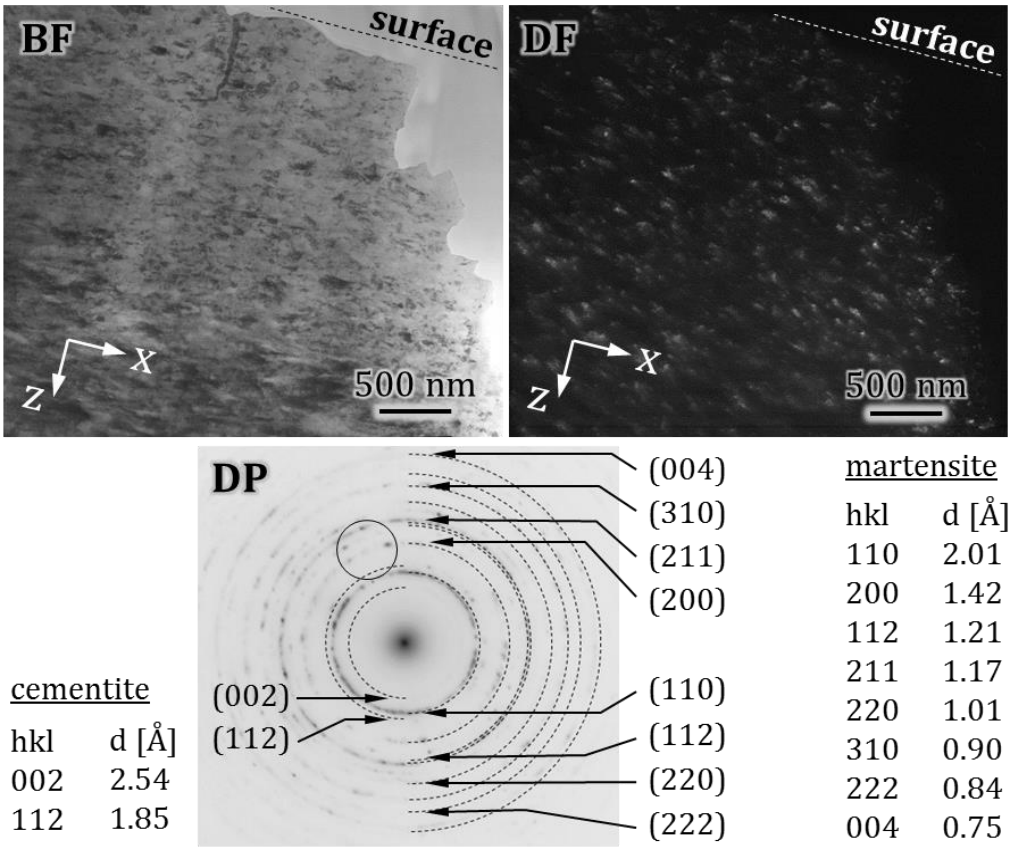

Figure 68: TEM micrograph of worn milled cast iron, shows a noticeable nc zone

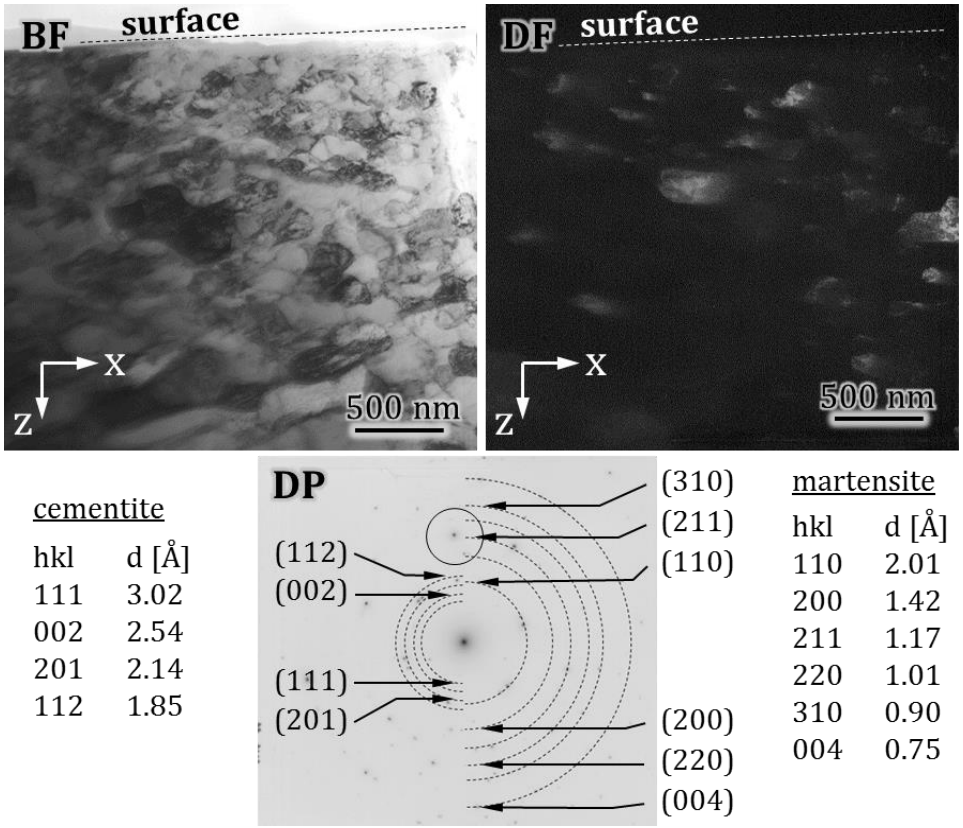

Figure 69: TEM image of worn ground CI near-surface zone reveals a grain-refined structure

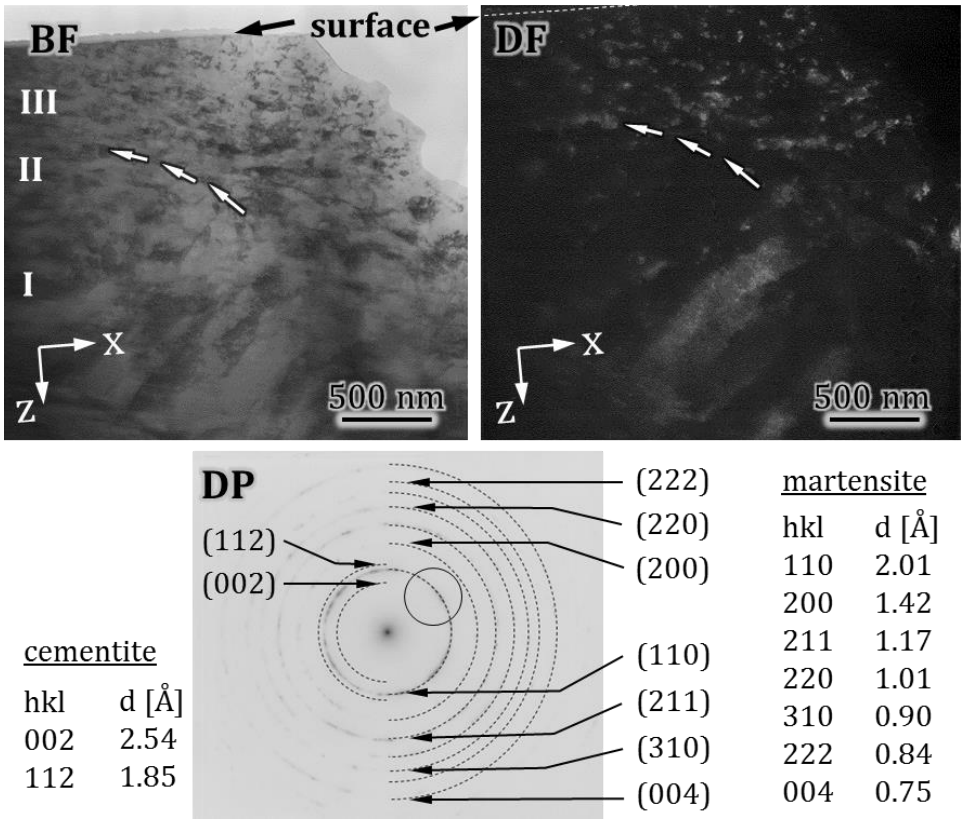

Figure 70: TEM image of worn honed CI exhibits a nc near-surface zone

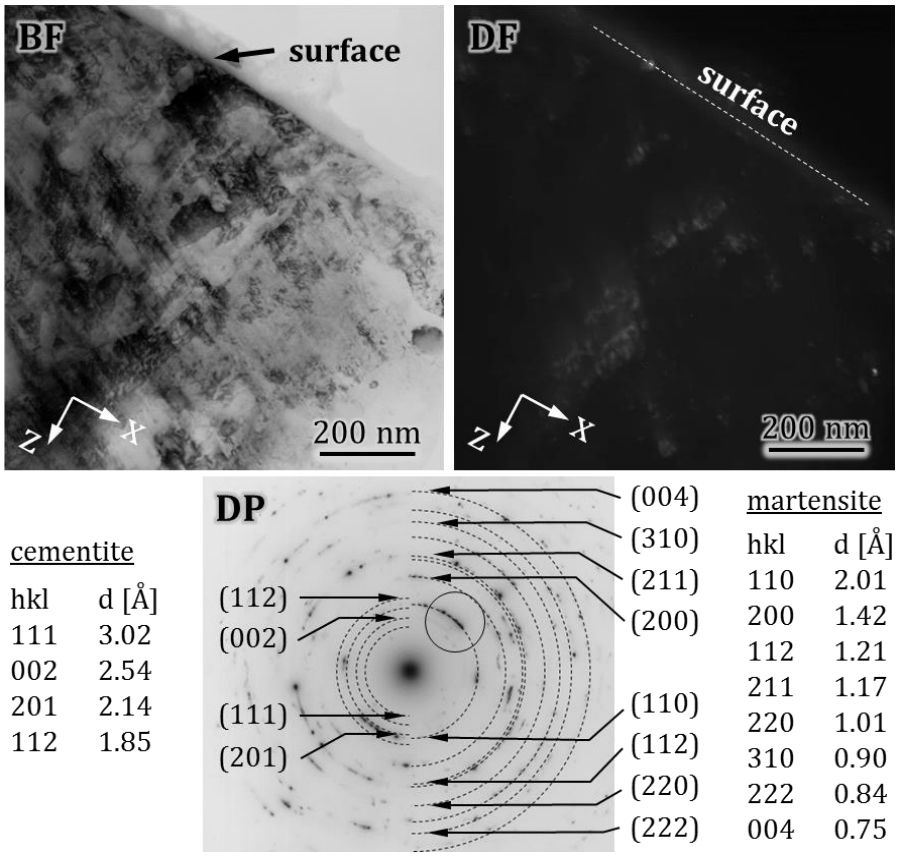

Figure 71: TEM image of the worn polished CI base body shows a grain-refined structure

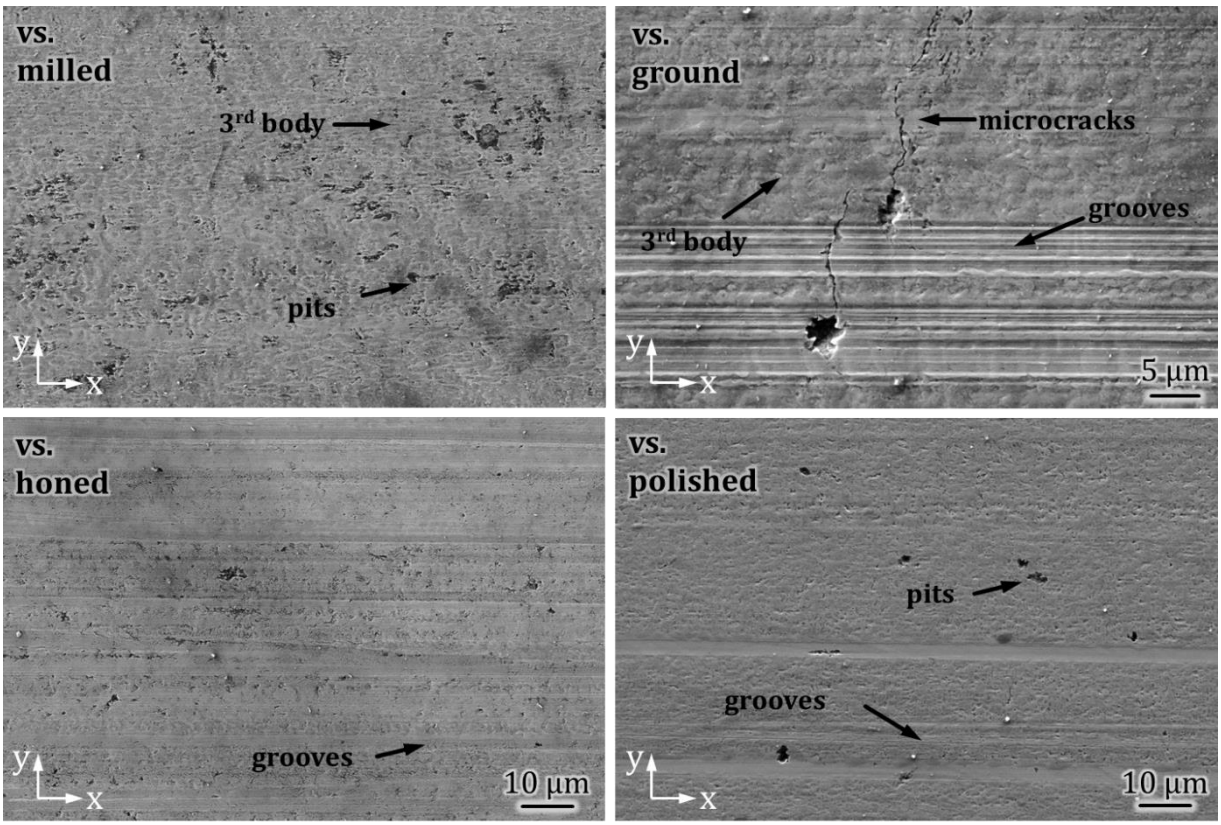

Figure 72: SEM images of bearing surfaces of the worn BS counter bodies

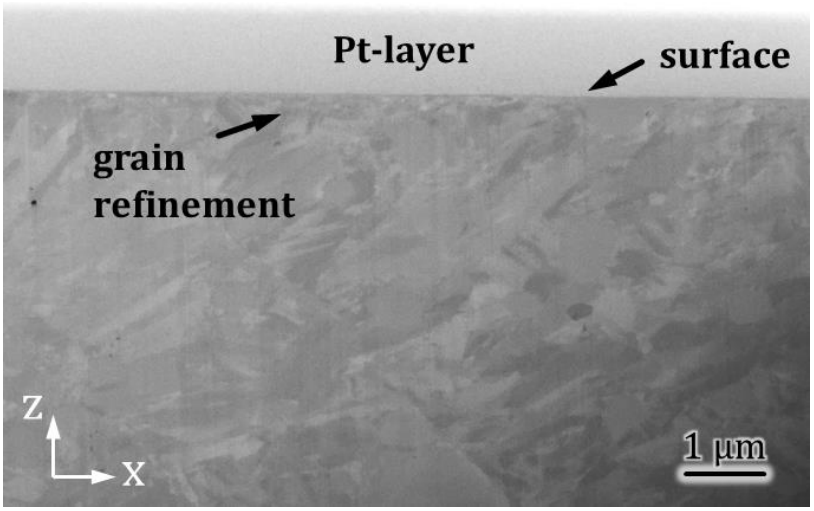

Figure 73: FIB cross-section of the bearing steel CB tested against the milled CI BB

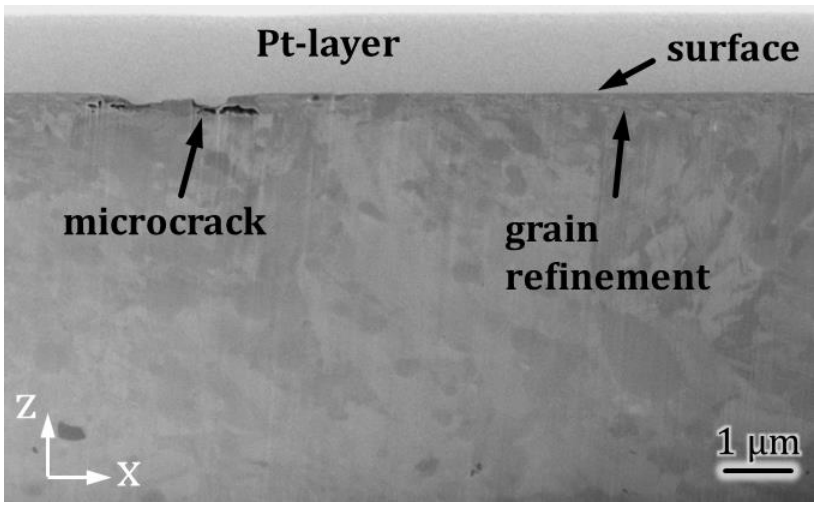

Figure 74: FIB cross-section of the bearing steel CB tested against the ground CI BB

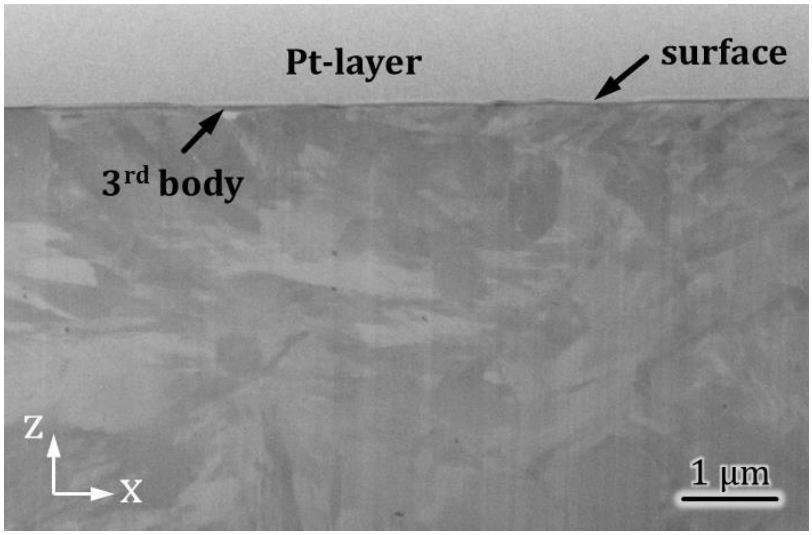

Figure 75: FIB cross-section of the bearing steel CB tested against the honed CI BB

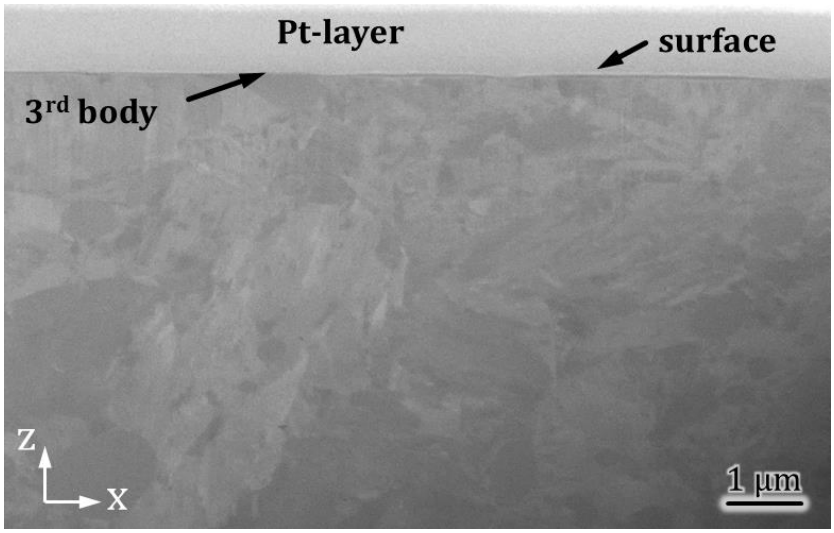

Figure 76: FIB cross-section of the bearing steel CB tested against the polished CI BB

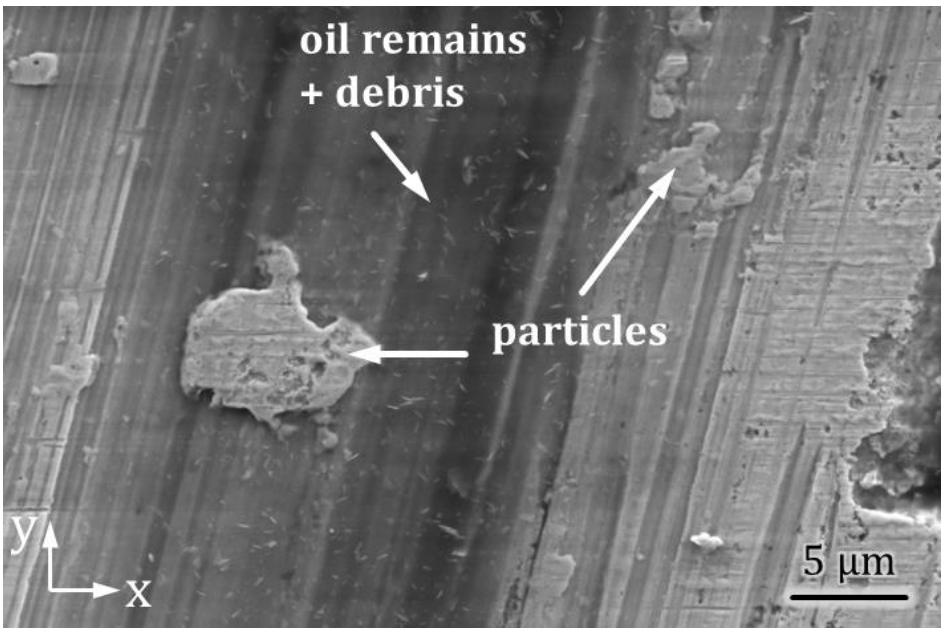

Figure 77: SEM image of the wear track of the milled cast iron shows debris trapped within a machining mark

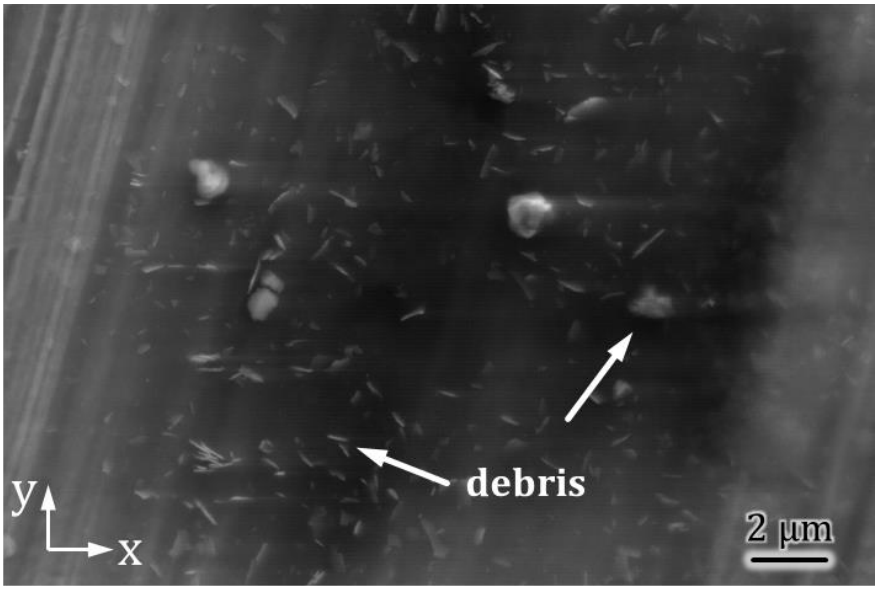

Figure 78: SEM image of flake-like cementite debris and oil residue within a machining mark

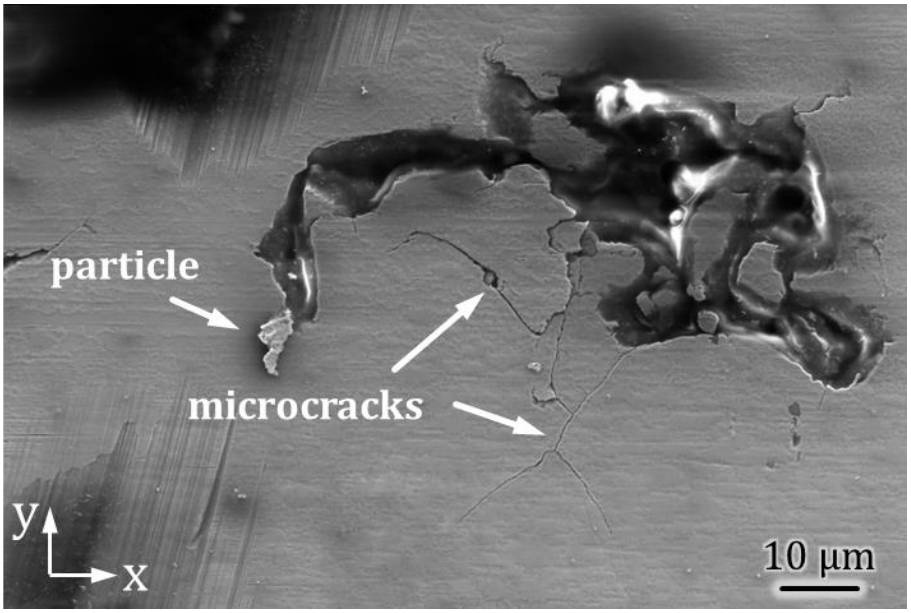

Figure 79: SEM micrograph of the worn honed CI sample shows cracks in the vicinity of graphite nodules

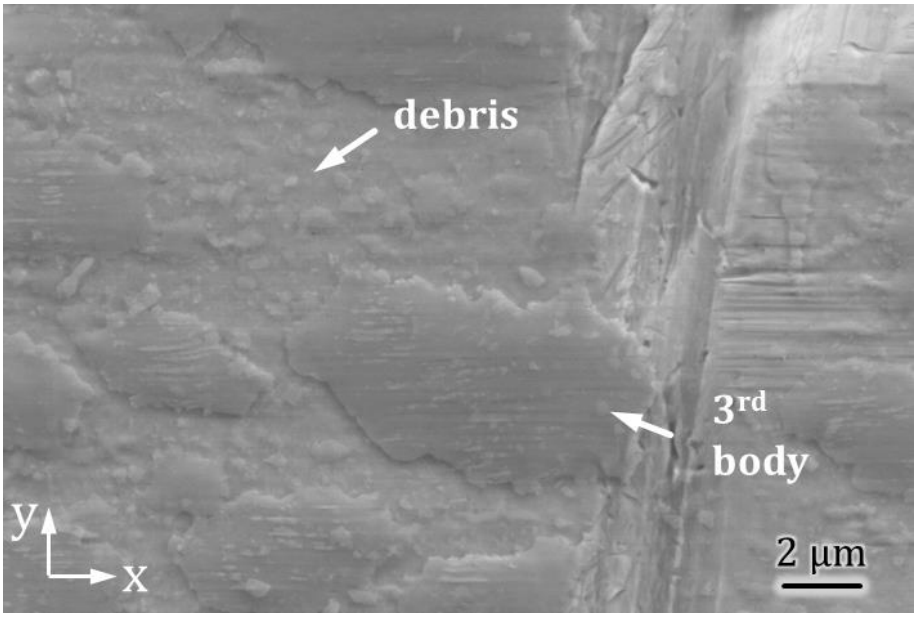

Figure 80: SEM image of the honed CI after wear test reveals patchy third bodies covering the bearing surface

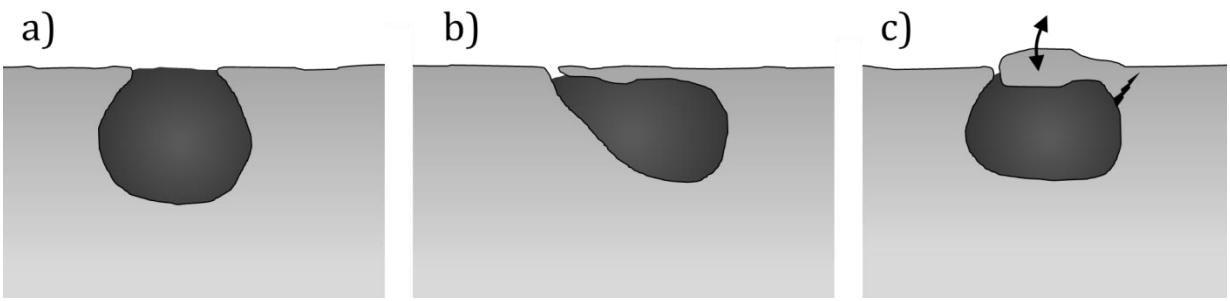

Figure 81: Schematic illustration of (a) open and (b+c) closed graphite nodules at the surface; (b) material smeared over and (c) material pushed into graphite nodule

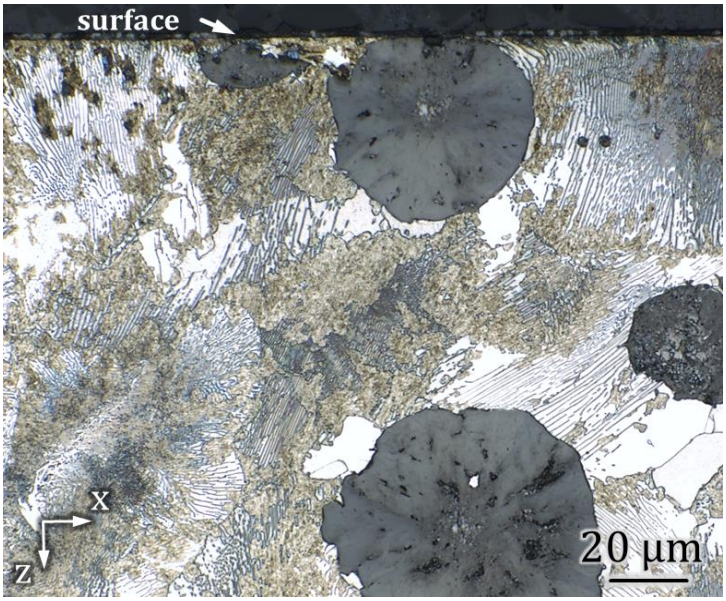

Figure 82: Optical micrograph of the subsurface zone of the ground cast iron reveals incomplete surface hardening

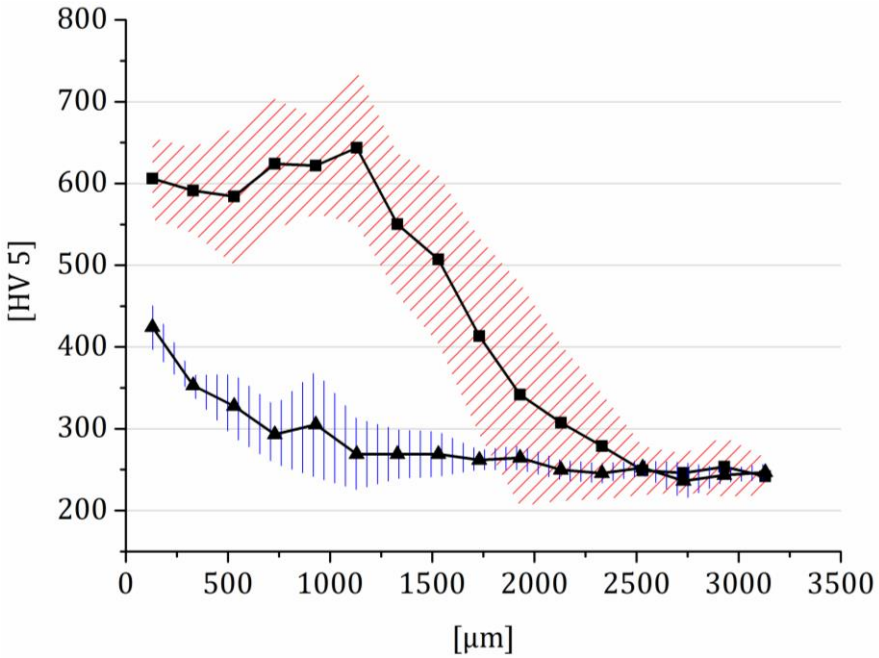

Figure 83: Hardness depth profile of properly flame hardened cast iron (red) in comparison with the hardness profile of the incomplete hardened region of the ground cast iron wear test sample (blue)

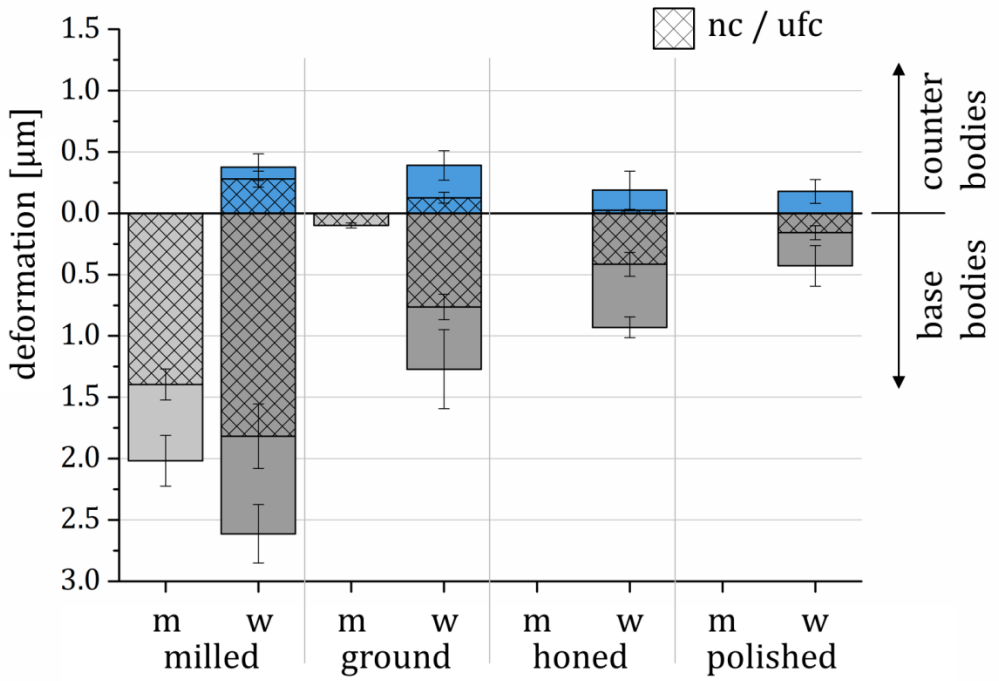

Figure 84: Deformation depths of the (m) machined and (w) worn cast iron and bearing steel samples

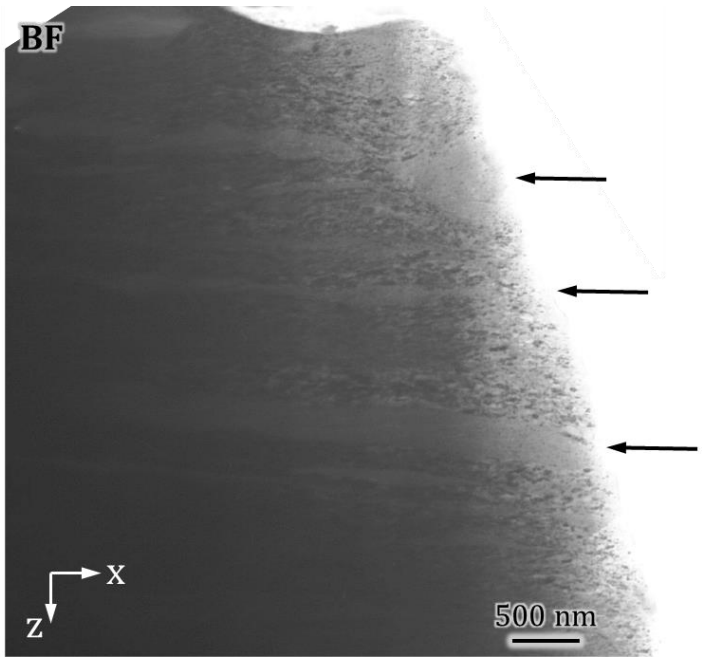

Figure 85: TEM image of shear bands in an AHI steel after tribological loading

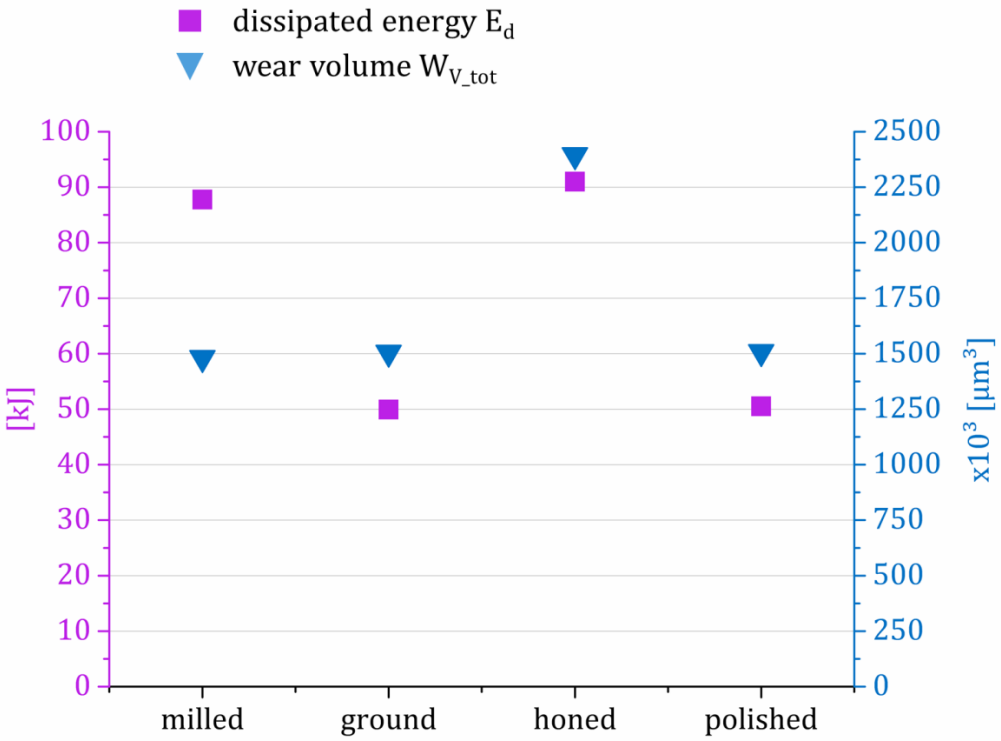

Figure 86: Dissipated friction energies and total wear volumes of the cast iron/bearing steel tribocouples

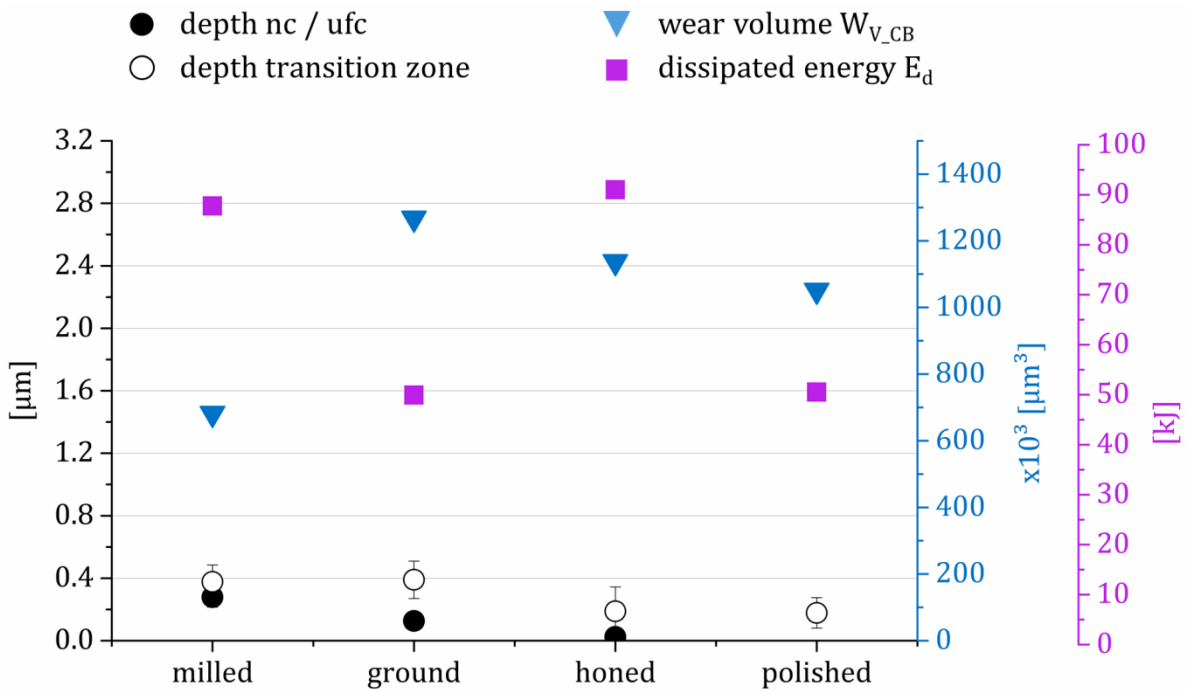

Figure 87: Dissipated friction energies linked to wear volumes and deformation depth of the bearing steel counter bodies

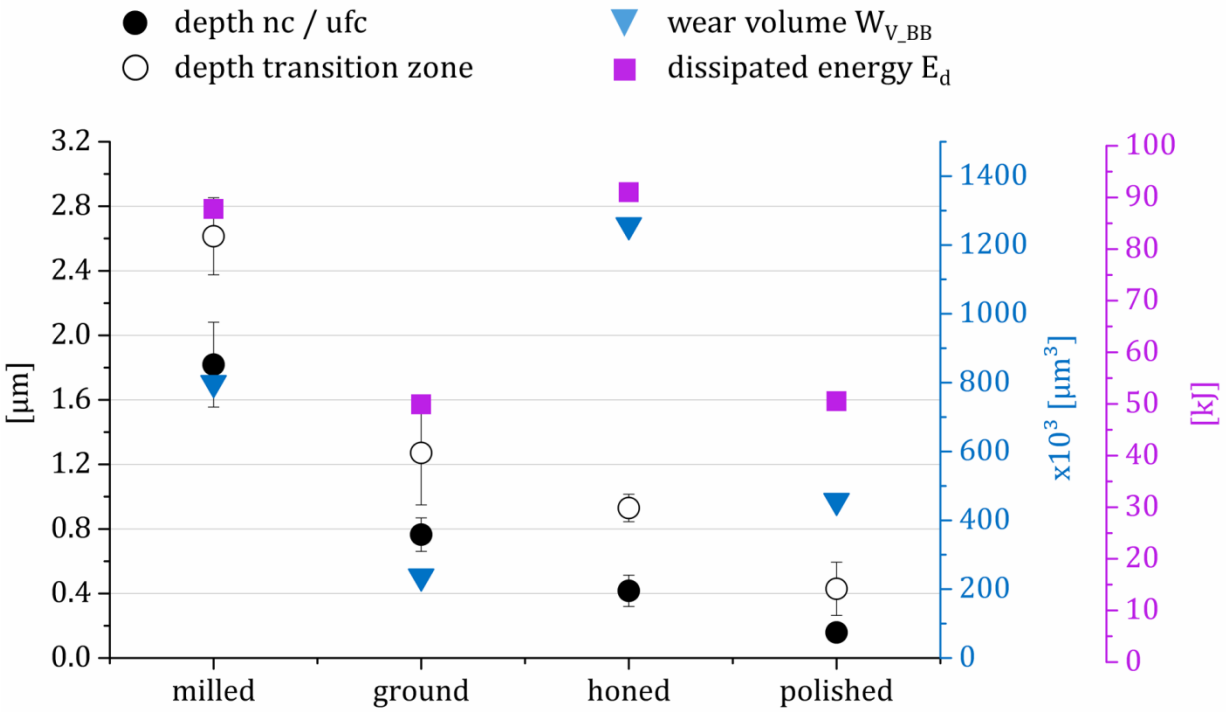

Figure 88: Dissipated friction energies linked to wear volumes and deformation depth of the cast iron base bodies

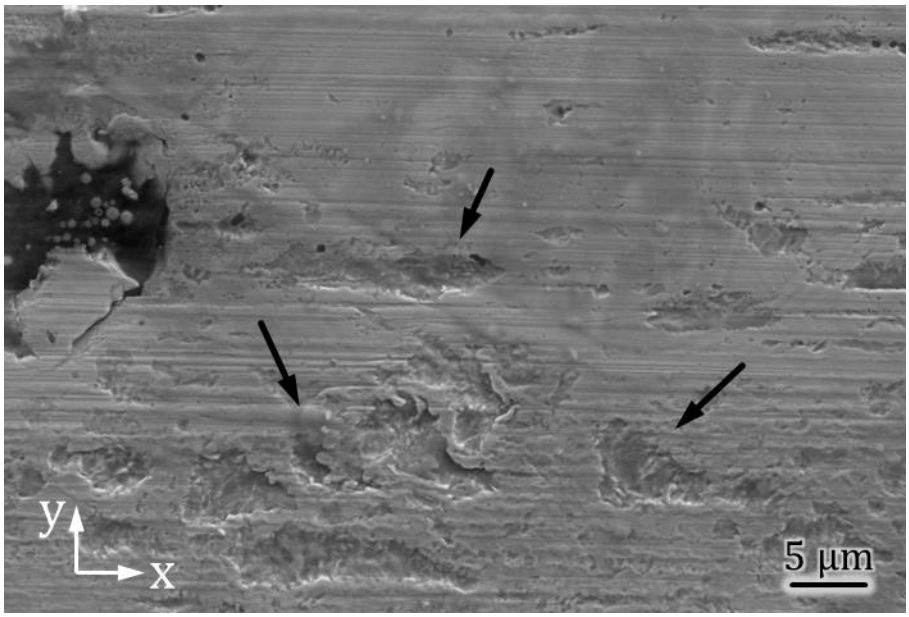

Figure 89: SEM image within the wear track of the polished cast iron specimen shows evidence of surface fatigue

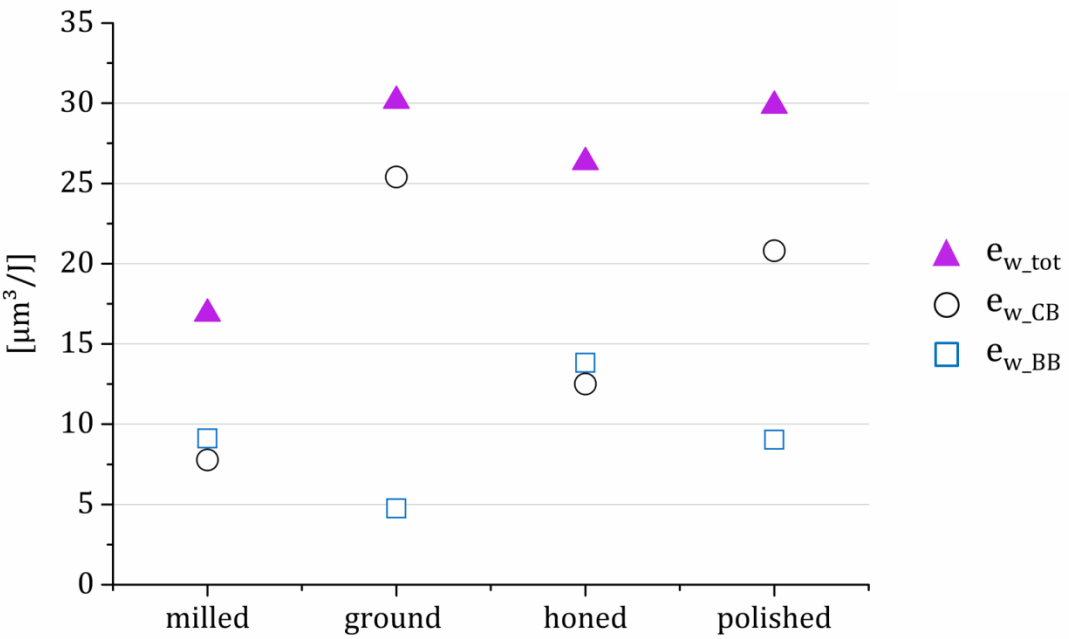

Figure 90: Energy-based wear rates e_w for the cast iron/bearing steel tribocouples display the dissipated energies related to the total wear volumes (w_tot) as well as to the wear volumes of counter (w_CB) and base bodies (w_BB)

13 References

[1] H. Berns, W. Theisen, Eisenwerkstoffe: Stahl und Gusseisen, 4. bearbeitete Aufl., Springer, Berlin, 2008.

[2] K. Holmberg, P. Andersson, A. Erdemir, Global energy consumption due to friction in passenger cars, Tribology International 47 (2012) 221–234.

[3] I. Tzanakis, M. Hadfield, B. Thomas, S.M. Noya, I. Henshaw, S. Austen, Future perspectives on sustainable tribology, Renewable and Sustainable Energy Reviews 16 (2012) 4126–4140.

[4] K. Gupta, R.F. Laubscher, J.P. Davim, N.K. Jain, Recent developments in sustainable manufacturing of gears: A review, Journal of Cleaner Production 112 (2016) 3320–3330.

[5] M. Dienwiebel, M. Scherge, Nanotribology in Automotive Industry, in: E. Gnecco, E. Meyer (Eds.), Fundamentals of friction and wear, Springer, Berlin, New York, 2007, pp. 549–560.

[6] P. Berlet, M. Dienwiebel, M. Scherge, The effect of sample finishing on the tribology of metal/metal lubricated contacts, Wear 268 (2010) 1518–1523.

[7] Y. Berthier, Third-Body Reality - Consequences and Use of the Third-Body Concept to Solve Friction and Wear Problems, in: G.W. Stachowiak (Ed.), Wear - Materials, Mechanisms and Practice, John Wiley & Sons Ltd, Chichester, England, 2005, pp. 291–316.

[8] R. Pourzal, A. Fischer, Reciprocating Sliding Wear of Surface Modified Austenitic High Nitrogen Stainless Steel and CoCrMo-Alloy, in: A. Fischer, K. Bobzin (Eds.), Friction, Wear and Wear Protection, Wiley-VCH Verlag GmbH & Co. KGaA, Weinheim, Germany, 2009, pp. 479–486.

[9] A. Hoppermann, M. Kordt, Tribological optimisation with laser-structured contact surfaces, Olhydraulik und Pneumatik 46 (2002) 560–564.

[10] R. Büscher, B. Gleising, W. Dudzinski, A. Fischer, The effects of subsurface deformation on the sliding wear behaviour of a microtextured high-nitrogen steel surface, Wear 257 (2004) 284–291.

[11] L. Wang, G. Zhang, R. Wood, S.C. Wang, Q. Xue, Fabrication of CrAlN nanocomposite films with high hardness and excellent anti-wear performance for gear application, Surface and Coatings Technology 204 (2010) 3517–3524.

[12] G. Marchiori, N. Lopomo, M. Boi, M. Berni, M. Bianchi, A. Gambardella, A. Visani, A. Russo, M. Marcacci, Optimizing thickness of ceramic coatings on plastic components for orthopedic applications: A finite element analysis, Materials Science and Engineering: C 58 (2016) 381–388.

[13] Y. Xiao, W. Shi, Z. Han, J. Luo, L. Xu, Residual stress and its effect on failure in a DLC coating on a steel substrate with rough surfaces, Diamond and Related Materials 66 (2016) 23–35.

[14] K. Bewilogua, G. Bräuer, A. Dietz, J. Gäbler, G. Goch, B. Karpuschewski, B. Szyszka, Surface technology for automotive engineering, CIRP Annals - Manufacturing Technology 58 (2009) 608–627.

[15] E. Roos, K. Maile, Werkstoffkunde für Ingenieure: Grundlagen, Anwendung, Prüfung, fourth., bearbeitete Aufl., Springer, Heidelberg, 2011.

[16] S. Jacobson, S. Hogmark, Surface modifications in tribological contacts, Wear 266 (2009) 370–378.

[17] D.A. Rigney, W.A. Glaeser, The significance of near surface microstructure in the wear process, Wear 46 (1978) 241–250.

[18] D. Shakhvorostov, B. Gleising, R. Büscher, W. Dudzinski, A. Fischer, M. Scherge, Microstructure of tribologically induced nanolayers produced at ultra-low wear rates, Wear 263 (2007) 1259–1265.

[19] E. Rabinowicz, The least wear, Wear 100 (1984) 533–541.

[20] B. Kim, J.C. Jiang, P.B. Aswath, Mechanism of wear at extreme load and boundary conditions with ashless anti-wear additives: Analysis of wear surfaces and wear debris, Wear 270 (2011) 181–194.

[21] P. Zeng, A. Rana, R. Thompson, W.M. Rainforth, Subsurface characterisation of wear on mechanically polished and electro-polished biomedical grade CoCrMo, Wear 332-333 (2015) 650–661.

[22] P.E. Sinnett-Jones, J.A. Wharton, R. Wood, Micro-abrasion–corrosion of a CoCrMo alloy in simulated artificial hip joint environments, Wear 259 (2005) 898–909.

[23] K.-H. Zum Gahr, Reibung und Verschleiss bei metallischen und nichtmetallischen Werkstoffen, DGM-Informationsgesellschaft m. b. H., Oberursel, Germany, 1990.

[24] M. Scherge, D. Shakhvorostov, K. Pöhlmann, Fundamental wear mechanism of metals, Wear 255 (2003) 395–400.

[25] M.J. Ghazali, W.M. Rainforth, H. Jones, Dry sliding wear behaviour of some wrought, rapidly solidified powder metallurgy aluminium alloys, Wear 259 (2005) 490–500.

[26] K. Jin, Z. Qiao, S. Zhu, J. Cheng, B. Yin, J. Yang, Friction and wear properties and mechanism of bronze–Cr–Ag composites under dry-sliding conditions, Tribology International 96 (2016) 132–140.

[27] A.R. Rosenfield, A shear instability model of sliding wear, Wear 116 (1987) 319–328.

[28] M. Scherge, A. Gervé, Mikrotribometrie im Maschinenbau, Mat.-wiss. u. Werkstofftech. 34 (2003) 934–937.

[29] S.V. Prasad, J.R. Michael, B.S. Majumdar, C.C. Battaile, N.R. Moody, M.J. Cordill, J.M. Jungk, D.J. Bammann, Modeling of Friction-Induced Deformation and Microstructures, Sandia Report (2006) 1–96.

[30] P. Stoyanov, P.A. Romero, T.T. Järvi, L. Pastewka, M. Scherge, P. Stemmer, A. Fischer, M. Dienwiebel, M. Moseler, Experimental and Numerical Atomistic Investigation of the Third Body Formation Process in Dry Tungsten/Tungsten-Carbide Tribo Couples, Tribol Lett 50 (2013) 67–80.

[31] A. Brink, Einlaufverhalten von geschmierten Stahl-Stahl-Paarungen unter Berücksichtigung der Mikrostruktur. Doctoral thesis at the Karlsruhe Institute of Technology, Karlsruhe, Germany, 2015.

[32] H.v. Weingraber, M. Abou-Aly, Handbuch Technische Oberflachen: Typologie, Messung und Gebrauchsverhalten, Vieweg, Braunschweig, 1989.

[33] H. Czichos, K.-H. Habig, Tribologie-Handbuch: Tribometrie, Tribomaterialien, Tribotechnik, third., überarbeitete und erw. Aufl., Vieweg+Teubner Verlag / GWV Fachverlage, Wiesbaden, Wiesbaden, 2010.

[34] I.S. Jawahir, E. Brinksmeier, R. M'Saoubi, D.K. Aspinwall, J.C. Outeiro, D. Meyer, D. Umbrello, A.D. Jayal, Surface integrity in material removal processes: Recent advances, CIRP Annals - Manufacturing Technology 60 (2011) 603–626.

[35] B. Karpuschewski, M. Toefke, M. Beutner, W. Spintig, Surface integrity aspects of milled large hardened gears, Procedia CIRP 13 (2014) 37–42.

[36] D.A. Lucca, E. Brinksmeier, G. Goch, Progress in Assessing Surface and Subsurface Integrity, CIRP Annals - Manufacturing Technology 47 (1998) 669–693.

[37] L. Sabri, S. Mezghani, M. El Mansori, A study on the influence of bond material on honing engine cylinder bores with coated diamond stones, Surface and Coatings Technology 205 (2010) 1515–1519.

[38] N. Tao, M. Sui, J. Lu, K. Lua, Surface nanocrystallization of iron induced by ultrasonic shot peening, Nanostructured Materials 11 (1999) 433–440.

[39] S. Goeke, D. Biermann, D. Stickel, P. Stemmer, A. Fischer, K. Geenen, S. Huth, W. Theisen, Enhancing the surface integrity of tribologically stressed contacting surfaces by an adjusted surface topography, Procedia CIRP 13 (2014) 214–218.

[40] M. Stewart, A New Approach to the Use of Bearing Area Curve, Society of Manufacturing Engineers (1990).

[41] E. Rabinowicz, Friction and wear of materials, secondnd ed., Wiley, New York, 1995.

[42] M. Hahn, Mikrostrukturelle Veränderungen in der Zylinderlaufbahn von PKW Dieselmotoren aus Grauguss und mittels thermischer Spritzverfahren hergestellter Stahlschichten. Doctoral thesis at the University of Duisburg-Essen, Duisburg Germany, 2012. VDI Verlag, Düsseldorf, 2013.

[43] J.F. Archard, W. Hirst, The Wear of Metals under Unlubricated Conditions, Proceedings of the Royal Society A: Mathematical, Physical and Engineering Sciences 236 (1956) 397–410.

[44] H. Czichos, Tribology: A systems approach to the science and technology of friction, lubrication, and wear, Elsevier Scientific Pub. Co; Distributors for the U.S. and Canada, Elsevier North Holland, Amsterdam, New York, New York, 1978.

[45] G. Schmaltz, Technische Oberflächenkunde: Feingestalt und Eigenschaften von Grenzflächen technischer Körper, insbesondere der Maschinenteile, J. Springer, Berlin, 1936.

[46] M. Hahn, R. Theissmann, B. Gleising, W. Dudzinski, A. Fischer, Microstructural alterations within thermal spray coatings during highly loaded diesel engine tests, Wear 267 (2009) 916–924.

[47] M. Dienwiebel, K. Pöhlmann, Nanoscale Evolution of Sliding Metal Surfaces During Running-in, Tribol Lett 27 (2007) 255–260.

[48] D. Shakhvorostov, K. Pöhlmann, M. Scherge, Structure and mechanical properties of tribologically induced nanolayers, Wear 260 (2006) 433–437.

[49] M. Godet, The third-body approach: A mechanical view of wear, Wear 100 (1984) 437–452.

[50] M. Godet, Third-bodies in tribology, Wear 136 (1990) 29–45.

[51] R. Pourzal, Possible pathways of particle formation in CoCrMo sliding wear. Doctoral thesis at the University of Duisburg-Essen, Duisburg, Germany, 2011. VDI Verlag, Düsseldorf, 2012.

[52] R. Büscher, A. Fischer, The pathways of dynamic recrystallization in all-metal hip joints, Wear 259 (2005) 887–897.

[53] M. Hahn, C. Bauer, R. Theissmann, B. Gleising, W. Dudzinski, A. Fischer, The impact of microstructural alterations at spray coated cylinder running surfaces of diesel engines – Findings from motor and laboratory benchmark tests, Wear 271 (2011) 2599–2609.

[54] A. Fischer, S. Weiss, M.A. Wimmer, The tribological difference between biomedical steels and CoCrMo-alloys, J Mech Behav Biomed Mater 9 (2012) 50–62.

[55] B. Dodd, Y. Bai, Introduction, in: B. Dodd, Y. Bai (Eds.), Adiabatic Shear Localization: Frontiers and Advances, second ed., Elsevier Science, Burlington, 2012, pp. 1–20.

[56] W.S. Farren, G.I. Taylor, The Heat Developed during Plastic Extension of Metals, Proceedings of the Royal Society A: Mathematical, Physical and Engineering Sciences 107 (1925) 422–451.

[57] S.D. Antolovich, R.W. Armstrong, Plastic strain localization in metals: origins and consequences, Progress in Materials Science 59 (2014) 1–160.

[58] R. Pippan, F. Wetscher, M. Hafok, A. Vorhauer, I. Sabirov, The Limits of Refinement by Severe Plastic Deformation, Adv. Eng. Mater. 8 (2006) 1046–1056.

[59] R. Valiev, R. Islamgaliev, I. Alexandrov, Bulk nanostructured materials from severe plastic deformation, Progress in Materials Science 45 (2000) 103–189.

[60] M. Busquet, S. Descartes, Y. Berthier, Formation conditions of mechanically modified superficial structures for two steels, Tribology International 42 (2009) 1730–1743.

[61] S.V. Dobatkin, J. Zrnik, I. Mamuzic, Nanostructures by severe plastic deformationof steels: Advantages and problems, Metalurgija 45 (2006) 313–321.

[62] C.C. Koch, Top-Down Synthesis of Nanostructured Materials: Mechanical and Thermal Processing Methods, Reviews on Advanced Materials Science 5 (2003) 91–99.

[63] E.O. Hall, The Deformation and Ageing of Mild Steel: III Discussion of Results, Proc. Phys. Soc. B 64 (1951) 747–753.

[64] N. Petch, The Cleavage Strength of Polycrystals, J. Iron Steel Inst. London (1953) 25–28.

[65] M. Zhao, J.C. Li, Q. Jiang, Hall–Petch relationship in nanometer size range, Journal of Alloys and Compounds 361 (2003) 160–164.

[66] C.E. Carlton, P.J. Ferreira, What is behind the inverse Hall-Petch effect in nanocrystalline materials?, Acta Materialia 55 (2007) 3749–3756.

[67] G. Saada, Hall-Petch revisited, Materials Science and Engineering A 400-401 (2005) 146–149.

[68] H. Conrad, J. Narayan, On the grain size softening in nanocrystalline materials, Scripta Materialia 42 (2000) 1025–1030.

[69] R.Z. Valiev, I.V. Alexandrov, Y.T. Zhu, T.C. Lowe, Paradox of strength and ductility in metals processed by severe plastic deformation, Journal of Materials Research 17 (2002) 5–8.

[70] R.Z. Valiev, Paradoxes of severe plastic deformation, Adv. Eng. Mater. 5 (2003) 296–300.

[71] Y. Wang, M. Chen, F. Zhou, E. Ma, High tensile ductility in a nanostructured metal, Nature 419 (2002) 912–915.

[72] B.J. Griffiths, Mechanisms of White Layer Generation With Reference to Machining and Deformation Processes, J. Tribol. 109 (1987) 525.

[73] O. Zwirlein, H. Schlicht, Werkstoffanstrengung bei Wälzbeanspruchung - Einfluß von Reibung und Eigenspannungen, Mat.-wiss. u. Werkstofftech. 11 (1980) 1–14.

[74] W. Liu, The failure analysis of the repeat geartooth breakage in a 40MW steam turbine load gearbox and the butterfly in the carburized case, Engineering Failure Analysis 46 (2014) 9–17.

[75] H.K. Bhadeshia, W. Solano-Alvarez, Critical Assessment 13: Elimination of white etching matter in bearing steels, Materials Science and Technology 31 (2015) 1011–1015.

[76] W. Österle, H. Rooch, A.R. Pyzalla, L. Wang, Investigation of white etching layers on rails by optical microscopy, electron microscopy, X-ray and synchroton X-ray diffraction, Materials Science and Engineering A 303 (2001) 150–157.

[77] A. Ramesh, S.N. Melkote, L.F. Allard, L. Riester, T.R. Watkins, Analysis of white layers formed in hard turning of AISI 52100 steel, Materials Science and Engineering A 390 (2005) 88–97.

[78] J.N. Barry, G.D. Byrne, TEM study on the surface white layer in two turned hardened steels, Materials Science and Engineering A 325 (2002) 356–364.

[79] S. Han, S.N. Melkote, M.S. Haluska, T.R. Watkins, White layer formation due to phase transformation in orthogonal machining of AISI 1045 annealed steel, Materials Science and Engineering A 488 (2008) 195–204.

[80] J.F. Archard, Contact and Rubbing of Flat Surfaces, J. Appl. Phys. 24 (1953) 981.

[81] A. Kapoor, J.A. Williams, Shakedown limits in sliding contacts on a surface-hardened half-space, Wear 172 (1994) 197–206.

[82] A.A. Torrance, The influence of surface deformation on mechanical wear, Wear 200 (1996) 45–54.

[83] A. Kappor, K.L. Johnson, J.A. Williams, A model for the mild ratchetting wear of metals, Wear 200 (1996) 38–44.

[84] A. Fischer, Subsurface microstructural alterations during sliding wear of biomedical metals. Modelling and experimental results, Computational Materials Science 46 (2009) 586–590.

[85] G. Kang, Ratchetting: Recent progresses in phenomenon observation, constitutive modeling and application, International Journal of Fatigue 30 (2008) 1448–1472.

[86] Quinn, T. F. J., Role of oxidation in the mild wear of steel, British Journal of Applied Physics Vol. 13 (1962) 33–37.

[87] J.L. Sullivan, Quinn, T. F. L., D.M. Rowson, Developments in the oxidational theory of mild wear, Tribology International (1980) 153–158.

[88] A.W. Batchelor, G.W. Stachowiak, A. Cameron, The Relationship between Oxide Films and the Wear of Steels, Wear (1986) 203–223.

[89] H. Hong, R.F. Hochman, Quinn, T. F. J., A New Approach to The Oxidational Theory of Mild Wear, Tribology Transactions 31 (1988) 71–75.

[90] K.C. Ludema, Mechanism-based modeling of friction and wear, Wear 200 (1996) 1–7.

[91] S.M. Hsu, M.C. Shen, A.W. Ruff, Wear prediction for metals, Tribology International 30 (1997) 377–383.

[92] M.F. Ashby, S.C. Lim, Wear-mechanism maps, Scripta Metallurgica et Materialia 24 (1990) 805–810.

[93] K. Kato, Classification of Wear Mechanisms/Models, in: G.W. Stachowiak (Ed.), Wear - Materials, Mechanisms and Practice, John Wiley & Sons Ltd, Chichester, England, 2005, pp. 9–20.

[94] G. Fleischer, Energetische Methode der Bestimmung des Verschleißes, Schmierungstechnik 4 (1973) 269–274.

[95] B.E. Klamecki, Energy dissipation in sliding, Wear 77 (1982) 115–128.

[96] P. Heilmann, D.A. Rigney, An energy-based model of friction and its application to coated systems, Wear 72 (1981) 195–217.

[97] H. Uetz, J. Föhl, Wear as an energy transformation process, Wear 49 (1978) 253–264.

[98] S. Fouvry, T. Liskiewicz, P. Kapsa, S. Hannel, E. Sauger, An energy description of wear mechanisms and its applications to oscillating sliding contacts, Wear 255 (2003) 287–298.

[99] O. Smerdova, D. Mazuyer, J. Cayer-Barrioz, Links between energy dissipation and wear mechanisms in solid epoxy/epoxy sliding contact, Tribology International 77 (2014) 148–159.

[100] S. Fouvry, P. Kapsa, An energy description of hard coating wear mechanisms, Surface and Coatings Technology 138 (2001) 141–148.

[101] K. de Moerlooze, F. Al-Bender, H. van Brussel, A novel energy-based generic wear model at the asperity level, Wear 270 (2011) 760–770.

[102] M.Z. Huq, J.-P. Celis, Expressing wear rate in sliding contacts based on dissipated energy, Wear 252 (2002) 375–383.

[103] Z. Rymuza, Energy concept of the coefficient of friction, Wear 199 (1996) 187–196.

[104] St. Hanke, I. Samerski, J. Schöfer, A. Fischer, The role of wear particles under multidirectional sliding wear, Wear 267 (2009) 1319–1324.

[105] D. Shakhvorostov, K. Pöhlmann, M. Scherge, An energetic approach to friction, wear and temperature, Wear 257 (2004) 124–130.

[106] J. Ruge, H. Wohlfahrt, Technologie der Werkstoffe: Herstellung, Verarbeitung, Einsatz ; mit 68 Tabellen, eighth., überarb. und erw. Aufl., Vieweg, Wiesbaden, 2007.

[107] D. Stickel, A. Fischer, R. Bosman, Specific dissipated friction power distributions of machined carburized martensitic steel surfaces during running-in, Wear 330-331 (2015) 32–41.

[108] D. Stickel, S. Goeke, K. Geenen, S. Huth, W. Theisen, D. Biermann, A. Fischer, Reciprocating sliding wear of case-hardened spheroidal cast iron against 100Cr6 under boundary lubrication, Proceedings of the Institution of Mechanical Engineers, Part J: Journal of Engineering Tribology 229 (2015) 1214–1226.

[109] D. Stickel, The Influence of Surface Finish on the Localized Dissipation of Frictional Power at Ultra-MildWear. Doctoral thesis at the University of Duisburg-Essen, Duisburg, Germany, 2015.

[110] R. Büscher, Gefügeumwandlungen und Partikelbildung in künstlichen Metall-Metall-Hüftgelenken. Doctoral thesis at the University of Duisburg-Essen, Duisburg, Germany, 2005. VDI Verlag, Düsseldorf, 2005.

[111] C.A. Schneider, W.S. Rasband, K.W. Eliceiri, NIH Image to ImageJ: 25 years of image analysis, Nat Meth 9 (2012) 671–675.

[112] S. Goeke, D. Biermann, D. Stickel, P. Stemmer, A. Fischer, K. Geenen, S. Huth, W. Theisen, Leistungssteigerung von Funktionsflächen durch eine gezielte Konditionierung der Oberflächenrandzone, in: 3. Győrer Tribologie Tagung, 2014, pp. 147–159.

[113] M. Heitkemper, A. Fischer, C. Bohne, A. Pyzalla, Wear mechanisms of laser-hardened martensitic high-nitrogen-steels under sliding wear, Wear 250 (2001) 477–484.

[114] M. Heitkemper, Verschleiss und Ermüdungsverhalten von kurzzeitlaserwärmebehandelten, hochstickstofflegierten Kaltarbeitsstählen. Doctoral thesis at the University of Duisburg-Essen, Duisburg, Germany, 2003. VDI Verlag, Düsseldorf, 2004.

[115] D. Turley, The nature of the white-etching surface layers produced during reaming ultra-high strength steel, Materials Science and Engineering 19 (1975) 79–86.

[116] H. Zhang, S. Ohsaki, S. Mitao, M. Ohnuma, K. Hono, Microstructural investigation of white etching layer on pearlite steel rail, Materials Science and Engineering A 421 (2006) 191–199.

[117] K.-H. Zum Gahr, Microstructure and wear of materials, Elsevier, Amsterdam, New York, 1987.

[118] I. Samerski, Verschleiß von kraftstoffgeschmierten Stahl-Stahl-Paarungen unter multidirektionaler reversierender Gleitbewegung. Doctoral thesis at the

University of Duisburg-Essen, Duisburg, Germany, 2009. VDI Verlag, Düsseldorf, 2009.

[119] D.A. Rigney, Large strains associated with sliding contact of metals, Materials Research Innovations 1 (1998) 231–234.

[120] D.A. Rigney, The Role of Characterization in Understanding Debris Generation, in: Wear Particles: From the Cradle to the Grave, Proceedings of the 18th Leeds-Lyon Symposium on Tribology, Elsevier, 1992, pp. 405–412.

[121] P.L. Ko, M. Robertson, E.E. Magel, Wear Particle Formation in Lubricated Sliding between a Hardened Sphere and a Flat Surface, in: Wear Particles: From the Cradle to the Grave, Proceedings of the 18th Leeds-Lyon Symposium on Tribology, Elsevier, 1992, pp. 81–90.

[122] J.K. Lancaster, Y.A. Mashal, A.G. Atkins, Particle Detachment Processes in the Dry and Lubricated Wear of Ceramics, in: Wear Particles: From the Cradle to the Grave, Proceedings of the 18th Leeds-Lyon Symposium on Tribology, Elsevier, 1992, pp. 237–246.

[123] G.W. Stachowiak, G.B. Stachowiak, D. de Pellegrin, P. Podsiadlo, Characterization and Classification of Abrasive Particles and Surfaces, in: G.W. Stachowiak (Ed.), Wear - Materials, Mechanisms and Practice, John Wiley & Sons Ltd, Chichester, England, 2005, pp. 339–368.

[124] D. Rigney, Transfer, mixing and associated chemical and mechanical processes during the sliding of ductile materials, Wear 245 (2000) 1–9.

[125] P. Stoyanov, P. Stemmer, T.T. Järvi, R. Merz, P.A. Romero, M. Scherge, M. Kopnarski, M. Moseler, A. Fischer, M. Dienwiebel, Friction and wear mechanisms of tungsten-carbon systems: a comparison of dry and lubricated conditions, ACS applied materials & interfaces 5 (2013) 6123–6135.

[126] J.M. Challen, P. Oxley, An explanation of the different regimes of friction and wear using asperity deformation models, Wear 53 (1979) 229–243.

[127] Z. Dimkovski, C. Anderberg, B.-G. Rosén, R. Ohlsson, T.R. Thomas, Quantification of the cold worked material inside the deep honing grooves on cylinder liner surfaces and its effect on wear, Wear 267 (2009) 2235–2242.

[128] M. Dienwiebel, N. Pradeep, G.S. Verhoeven, H.W. Zandbergen, J.W. Frenken, Model experiments of superlubricity of graphite, Surface Science 576 (2005) 197–211.

[129] J. Sugishita, S. Fujiyoshi, The effect of cast iron graphite on friction and wear performance III: The lubricating effect of graphite under rolling-sliding contacts, Wear 77 (1982) 181–193.

[130] L. Sabri, M. El Mansori, Process variability in honing of cylinder liner with vitrified bonded diamond tools, Surface and Coatings Technology 204 (2009) 1046–1050.

[131] H.T. Angus, The significance of hardness, Wear 54 (1979) 33–78.

[132] P.J. Burnett, D.S. Rickerby, The relationship between hardness and scratch adhession, Thin Solid Films 154 (1987) 403–416.

[133] D.H. Buckley, The Influence of the Atomic Nature of Crystalline Materials on Friction, A S L E Transactions 11 (1968) 89–100.

[134] S. Tarasov, V. Rubtsov, A. Kolubaev, Subsurface shear instability and nanostructuring of metals in sliding, Wear 268 (2010) 59–66.

[135] S. Fouvry, P. Kapsa, L. Vincent, An elastic–plastic shakedown analysis of fretting wear, Wear 247 (2001) 41–54.

[136] A. Luft, Microstructural Proscesses of Plastic Instabilities in Strengthend Metals, Progress in Materials Science Vol. 35 (1991) 97–204.

[137] W.M. Rainforth, R. Stevens, J. Nutting, Deformation structures induced by sliding contact, Philosophical Magazine A 66 (1992) 621–641.

[138] J.-H. Wu, S. Karthikeyan, M.L. Falk, D.A. Rigney, Tribological characteristics of diamond-like carbon (DLC) based nanocomposite coatings, Wear 259 (2005) 744–751.

[139] M. Scherge, D. Linsler, T. Schlarb, The running-in corridor of lubricated metal–metal contacts, Wear 342-343 (2015) 60–64.

[140] A. Fischer, Well-founded selection of materials for improved wear resistance, Wear 194 (1996) 238–245.

[141] P. Stoyanov, P.A. Romero, R. Merz, M. Kopnarski, M. Stricker, P. Stemmer, M. Dienwiebel, M. Moseler, Nanoscale sliding friction phenomena at the interface of diamond-like carbon and tungsten, Acta Materialia 67 (2014) 395–408.

[142] R. de Kloe, Do You Want to Be Average(d)?, 2015, Information on http://edaxblog.com/2015/09/22/do-you-want-to-be-averaged/

[143] EDAX, Operation Manual OIM 6.0.

14 Appendix

Particle Preparation

Particle isolation procedure

1) Centrifuge lubricant samples and carefully remove supernatants (centrifugation time depends on the viscosity of the medium). Do not touch the pellet at the bottom of the tubes.
2) Resuspend and wash particles with cyclohexane, use shaker (Vortex-Genie-2, Scientific Industries, Bohemia, NY, USA) and ultrasonic cleaner
3) Centrifuge for 15 min at 20,000 x g
4) Carefully discard supernatants. Do not touch the pellet at the bottom of the tubes! Resuspend and wash particles with acetone, use shaker and ultrasonic cleaner
5) Centrifuge for 15 min at 20,000 x g
6) Carefully discard supernatants. Do not touch the pellet at the bottom of the tubes! Resuspend and wash particles with isopropanol, use shaker and ultrasonic cleaner
7) Centrifuge for 15 min at 20,000 x g
8) Carefully discard supernatants. Do not touch the pellet at the bottom of the tubes! If necessary repeat steps 2-8
9) Store particles in isopropanol or ethanol at 4°C

Cyclohexane and acetone are used in order to dissolve the lubricant. These solvents (particularly cyclohexane) should not be stored in the tubes for too long since they can damage the tubes! They would also damage the carbon film on the Cu-grids. Therefore it is necessary to suspend the particles in a less aggressive solvent, such as isopropanol or ethanol, before applying them on Cu-grids.

Particle embedding

1st day:

1) Centrifuge for 15 min at 20,000 x g
2) Prepare acetone/epoxy mixture
   Mix epoxy and hardener at a ratio of 100:50
   (Epoxy 3000 Quick, Cloeren Technology GmbH, Wegberg, Deutschland)
   Add 100% acetone at a ratio of 1:1
3) Carefully discard supernatants. Do not touch the pellet at the bottom of the tubes!
   Add 0.5 ml of the acetone/epoxy mixture
4) Place tubes in a rotator (Thermomixer compact, Eppendorf, Hamburg, Germany) for 24 h

2nd day:

1) Centrifuge for 15 min at 20,000 x g
2) Place tubes, with open lids, under vacuum for 1 h in order to remove the acetone
3) Place tubes, with open lids, at 80 °C for 24 h for polymerization

3rd day:

Remove tubes to obtain solid pieces of resin with particles embedded at the bottom

➔ Section with diamond blade to a thickness of approx. 90 nm